8-28-2012

# Unipolar barrier strained layer superlattice infrared photodiodes : physics and barrier engineering

Nutan Gautam

NUTAN GAUTAM
*Candidate*

ELECTRICAL AND COMPUTER ENGINEERING
*Department*

This dissertation is approved, and it is acceptable in quality and form for publication:

*Approved by the Dissertation Committee:*

PROF. SANJAY KRISHNA , Chairperson

PROF. LUKE F. LESTER

PROF. KEVIN J. MALLOY

DR. DAVID Z. -Y. TING

# Unipolar Barrier Strained Layer Superlattice Infrared Photodiodes: Physics and Barrier Engineering

by

**NUTAN GAUTAM**

**B.SC., DAYALBAGH EDUCATIONAL INSTITUTE, AGRA, 2003**
**M.SC., DAYALBAGH EDUCATIONAL INSTITUTE, AGRA, 2005**
**M. TECH, INDIAN INSTITUTE OF TECHNOLOGY, KANPUR, 2007**

**COMMITTEE CHAIR: PROF. SANJAY KRISHNA**

DISSERTATION

Submitted in Partial Fulfillment of the
Requirements for the Degree of

**DOCTOR OF PHILOSOPHY**
**ENGINEERING**

The University of New Mexico
Albuquerque, New Mexico

July 2012

*Dedicated to My Mother,*

*Smt. Urmila Gautam*

# Acknowledgments

I would like to thank my advisor, Prof. Sanjay Krishna for guiding me and supporting me throughout my term as a graduate student. Working with him was fun as he is open to new ideas and gave freedom to explore the field which indeed made the research interesting. He always has time for his students and he is a patient listener of all the failures which come on the way of graduate research. He has been a motivating advisor and has always come up with a positive message from tough situations. The only situation which makes him unhappy is the news of broken MBE! I would like to thank my committee members, Prof. Luke F. Lester, Prof. Kevin J. Malloy, and Dr. D. Z. –Y. Ting for their time and constructive suggestions during the course of my PhD.

I am thankful to all my present and past group members for helping me at various stages. I want to thank Dr. Yagya Sharma for his help in my initial days at CHTM. I would like to thank Ajit and Stephen for teaching me characterization and processing. Many thanks to Dr. Elena Plis, for teaching me MBE! Special thanks to Prof. Ganesh Balakrishnan for insightful growth discussions and Dr. Thomas Rotter for his help and growth tips. Thanks to Dr. Alex Albrecht for maintaining the PL setup. I would like to thank Stephen, Brianna, Maya, Ha Sul and Dr. Zhao-Bing Tian for help with device processing. I want to thank Brianna for her help with absorption and PL measurements. I would like to thank Ted for proof reading my thesis. Thanks to Brianna, Maya and Marziyeh for yelling at Stephen and pulling his legs. Thanks to Stephen for being my best gossiping buddy, we discussed stories about each and everyone! Thanks to John Montoya for some exciting discussions on random topics and Maya for her dinners and cakes! A very special thanks to Prof. Ralph Dawson for his encouragement, guidance and trust in my abilities.

I want to thank Rick Bradley and Dan Bryant for making sure that all the facilities run smoothly at CHTM. I would also like to thank all the cleanroom staff, for making sure that all the equipment are available as much as possible. The office staff at CHTM has been wonderful and thanks to them for taking care of the all the paper work. Thanks to Joe Sadler for always being there for computer glitches. Special thanks to Ms. Elmyra Grelle from ECE for helping me and answering all my queries.

It is impossible for me to thank my mother and father who always trusted in me and supported me in all my decisions. My mother made me the person I am today, and being a mother I know it's not easy. My sister Neha and brother Rinku have been two support pillars and have always stood by my side.

During my PhD, the person whom I looked upto is Ajit and probably that is why he says that my thesis is the superlattice version of his thesis. I ran all my ideas and results through him and anxiously waited for his criticism as well as appreciation, everything got better after that. He made my stay here wonderful, first as a best friend then as a boyfriend and finally as my husband! It has been amazing to discuss research during breakfast or dinner. He is the best husband material for a researcher! I want to thank Aai for her love and support, without her it would not have been easy to finish my thesis. Finally, love to my daughter Anvesha who always fills me with enthusiasm and delight, the past one year went by so fast juggling between graduate research and challenges of being a new mom.

# Unipolar Barrier Strained Layer Superlattice Infrared Photodiodes: Physics and Barrier Engineering

by

**Nutan Gautam**

Master of Technology, Indian Institute of Technology,

Kanpur, India, 2007

PhD, Engineering, University of New Mexico, 2012.

## Abstract

Type-II InAs/GaSb Strained Layer Superlattice (T2SL) is an emerging technology for infrared detection. They are being seen as a threat to 50 years old incumbent technology based on Mercury-Cadmium-Telluride (MCT) system. T2SL have been theoretically predicted to outperform MCTs. This dissertation has been aimed at improving the physical understanding and detector performance of T2SL detectors.

This work has been focused on the bandstructure simulation, molecular beam epitaxy (MBE) growth optimization, physical understating, and heterojunction barrier engineering of T2SL, in midwave infrared (MWIR, 3-5μm) and longwave infrared (LWIR, 8-12μm) regimes. The bandstructure of InAs/GaSb/AlSb superlattices has been simulated in this work using empirical pseudopotential method. The simulation results

have been used extensively in the later part of this work for designing heterojunction T2SL photodetectors. The interfaces between the individual layers (InAs and GaSb) in T2SL have been optimized for improving the detector performance. Performance of different interface structures were evaluated using variable temperature photoluminescence response, and with the use of detector performance parameters such as responsivity, detectivity and dark current. It was concluded that supporting "InSb" type bonds at both the interfaces resulted in the best performance. This was achieved by using $Sb_2$ soak time on "InAs on GaSb" interface and growing thin InSb layer on "GaSb on InAs" interface. This also helps in strain balancing the system. This interface scheme has been subsequently used in the high performance LWIR pBiBn devices as well as the HOT MWIR cascade devices, giving lattice matched T2SL in these structures. Physical properties of T2SL system are not very well understood, for example the nature of minibands. Polarization sensitive photocurrent spectroscopy measurements were carried out on MWIR and LWIR T2SL material, and experimental results were correlated with the theoretical simulations to unambiguously establish the ordering of valence minibands in T2SL system. It was found that the ordering of minibands with the increase in energy in the valence band is HH1, LH1, LH2 and HH2.

The performance of InAs/GaSb T2SL photodiodes was improved by barrier engineered devices. Device architecture, called pBiBn, was proposed in this work, and was realized for MWIR and LWIR detectors. It uses unipolar electron and hole current blocking layers to reduce the various components of the dark currents. LWIR devices optimized for this device architecture demonstrated the performance close to the state of the art in T2SL technology with the dark current density of $1.42 \times 10^{-5} A/cm^2$, with cutoff wavelength on

10μm at 76K. MWIR pBiBn device also demonstrated high operating temperature (HOT). The capability of multicolor detection using InAs/GaSb/AlSb system was demonstrated in this work by realizing two-color and three color detectors, using three contact architecture, for SWIR/MWIR/LWIR detection.

An interband cascade detector based on InAs/GaSb T2SL system was implemented in this work for HOT application. It consisted of absorber, tunneling and transport regions and all the regions were based on InAS/GaSb/AlSb system. The MWIR ($\lambda_c$=5μm, T=77K) cascade detector demonstrated operation up to 420K, which is the highest reported operating temperature in MWIR regime, while the LWIR ($\lambda_c$=9.6μm, T=80K) device operated till 200K with an optimal bias range of a few mV. This work has demonstrated the flexibility of InAs/GaSb/AlSb superlattice system by heterojunction device designs and their successful implementation.

# Contents

# List of Figures

# List of Tables

# 1 Introduction

The photon emission spectrum of objects with temperatures above absolute zero is determined by Planck's law [1],

$$L_e = \frac{2hc^2}{\lambda^5}\frac{1}{e^{\frac{hc}{\lambda k_B T}}-1}\left(\frac{W}{cm^2 sr\ \mu m}\right) \quad (1.1)$$

Where $L_e$ is the spectral radiance, λ is the wavelength of light, $h$ is Planck's constant, $c$ is the speed of light in vacuum, and $k_B$ is Boltzmann constant. This has been plotted in Fig. 1.1, after scaling it to a more appropriate form of photon radiance ($L_q$) (photons/cm$^2$.s.sr.μm) for photon detectors. The emission spectrum of objects at room temperature (295K) peaks at a wavelength of 9.8μm, which falls in the infrared range, according to Wien's displacement law.

$$\lambda(\mu m) = \frac{2897.768}{\mathrm{T(K)}} \quad (1.2)$$

The infrared spectrum is important because objects with temperatures in the range of 100K to 1000K have the highest radiance in this regime, as can be seen from Fig. 1.1, which is for perfect blackbody objects and can be scaled for real objects depending on their emissivity (ε). This covers wavelengths all the way from 0.7 μm to 1000 μm. Hence, the detection of infrared is important for observing wavelengths which are beyond the sensitivity of the human eye. This leads to the application of infrared detection in defense and security, surveillance, medical imaging, industrial hot-spot, and astronomy. It has been divided into different bands of interest, such as near infrared (NIR) from 0.7

μm to 1 μm, shortwave infrared (SWIR) from 1 μm to 3 μm, midwave infrared (MWIR) from 3 μm to 5 μm, longwave infrared (LWIR) from 8 μm to 14 μm, very longwave infrared (VLWIR) from 14 μm to 30 μm and terahertz (THz) or far infrared (FIR) from 30 μm all the way up to 1000 μm. MWIR and LWIR bands are important as emission from objects at room temperature (RT) or higher than RT by 670°C peaks in these bands. This leads to their application in night vision, monitoring heat distribution in airplane fuel compartment, etc.

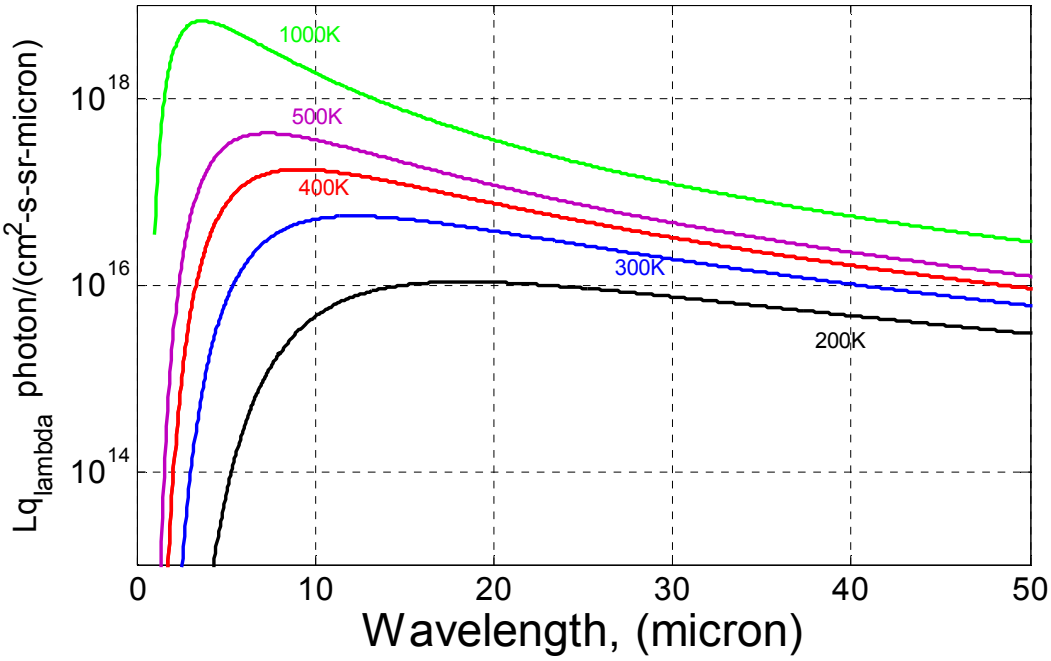


Fig. 1.1 Spectral photon radiance as a function of wavelength for different blackbody temperatures.

## 1.1 Infrared Detectors

Infrared detectors can be divided into two broad categories [2, 3], thermal detectors and photon detectors. In thermal detectors, such as Si microbolometers, pyrometers, thermocouples, Golay cells, and superconductors, incident optical radiation increases the

temperature of the detector which leads to a change in physical parameters, such as resistance or voltage. Some of the characteristic features of thermal detectors are broad spectrum, room temperature operation, low cost, and slow response. However, superconductor based thermal detectors are expensive as they need cryogenic cooling[1]. Photon detectors detect light by changing their electrical properties, such as conductance or voltage drop for every photon absorbed. Photon detectors for infrared are typically realized using III-V and II-VI semiconductors, and can further be divided into intersubband and interband detectors. Examples of intersubband detectors are quantum well infrared photodetectors (QWIP)[4] and quantum dot infrared photodetectors (QDIP)[5, 6], where intersubband transition energies in the conduction band can be tailored to detect infrared radiation. Examples of interband detectors are HgCdTe (MCT), InSb, and InAs/GaSb/AlSb type-II strained layer superlattice (T2SL) systems. This thesis has been focused on interband infrared detectors based on InAs/GaSb/AlSb T2SL system.

The various types of detectors discussed above cater to different application requirements [3]. Intersubband QWIP detectors, based on GaAs and InP systems, are commercially available for high-volume, low cost applications. However, QWIPs lack normal incidence operation, need cryogenic cooling and suffer from low quantum efficiency (QE) [7]. Research on QDIP detectors has been focused on improving performance over that of QWIPs as QDIPs can absorb normal incidence light and their fabrication process is similar to that of QWIPs [6]. InSb detectors are commercially used for the detection of MWIR radiation, and need cryogenic cooling. Also, they are not suited for multicolor detection. MCT[8] based detectors are seen as major players in low-volume, high-cost applications and are used in LWIR detection. They are low-noise detectors and have high

quantum efficiency (QE). However, they suffer from non-uniformity of substrates and high cost. Research on InAs/GaSb/AlSb T2SL has been focused on demonstrating performance equivalent to that of MCT detectors. A detailed comparison of these two technologies has been given in next section.

## 1.2 T2SL Detectors

Type II superlattice based on the InAs/GaSb semiconductor system was first proposed by Nobel Laureate Leo Esaki more than four decades ago[9, 10]. The use of this system for infrared detection, along with a detailed theoretical model, was later proposed by Smith and Mailhiot in 1987[11]. It was followed by experimental and theoretical research in the field. A detailed historical account of the development of T2SL technology has been provided by Ting *et al*.[12]. Theoretically, the T2SL system was proposed to outperform the MCT detectors. While the performance of MCT detectors is limited by Auger lifetime, theoretical calculations speculate a much longer Auger lifetime in InAs/GaSb T2SL[13]. This is due to the strain in the system, which leads to the degeneracy lifting in the valence band, separating heavy hole and light hole energies at Γ point. Experimentally measured Auger lifetimes in T2SL were found to be two orders of magnitude longer than that of MCT detectors with the same cutoff wavelength[14]. Also, the T2SL system has a higher carrier effective mass than MCT material, which leads to a reduction in tunneling currents[12]. Since T2SLs are based on III-V semiconductors, the processing and handling is much easier than that of MCT detectors. T2SL detectors have demonstrated absorption QE comparable to that of MCT detectors [15-17].

The InAs/GaSb superlattices are made of alternating layers of InAs and GaSb, each a few monolayers in thickness. The band alignment between InAs and GaSb is such that the

conduction band of InAs is 150meV below the valence band of GaSb. This type of band lineup is called a type-II broken gap and hence the name T2SL. The band lineup amongst the 6.1Å family[18] (GaSb/InAs/AlSb) has been shown in Fig. 1.2. There is a type-II staggered alignment between InAs and AlSb, while GaSb and AlSb demonstrate type-I nested alignment. In the InAs/GaSb T2SL system, electrons and holes are confined inside the InAs and GaSb layers, respectively. Since the thicknesses of individual layers are small, the electron and hole wavefunctions of adjacent wells overlap significantly, which leads to the formation of minibands. A schematic of this is shown in Fig. 1.3. The effective bandgap, which is the energy difference between the first conduction miniband and the first hole miniband can be tailored from SWIR to VLWIR bands. Another important characteristic of superlattices is the bandgap and bandoffset tunability obtained by changing the thickness of the constituent layers and materials. This enables the design of heterojunction photodiodes based on the InAs/GaSb/AlSb system. The first superlattice focal plane array (FPA) in a 320x256 format was reported in the mid-wave infrared region (MWIR, $\lambda_c$=5μm) in 2005 [19]. Since then significant progress has been made in the realization of high performance detectors using heterojunction barrier engineered devices [20-23]. This has recently resulted in the fabrication of a large format (1-megapixel) FPA [24, 25].

## 1.3 Motivation and Approach

Though there has been a significant progress in the development of FPAs based on the T2SL system, understanding of the material system is not well established. The quantum confined minibands and their types are not well understood. There have been theoretical ventures to establish the nature of minibands, but they contradict each other. The carrier

transport is another aspect which needs further research and understanding. It is unclear how electrons and holes take part in the transport and what determines their mobility spectrum. This is a subject of study by a number of groups. The T2SL systems exhibit shorter carrier lifetimes than MCT detectors, which are believed to be dominated by Shockley-Read-Hall (SRH)[26-29] processes. The exact nature and origin of SRH centers is not well known, and can be related to the defects or interfaces between the alternating layers. The epitaxial growth of T2SL detectors is carried out using molecular beam epitaxy (MBE). Interfaces between the constituent layers can be controlled in many different ways and have been shown to play an important role in device performance[30-34]. Interface quality can also vary from one growth chamber to another as shutter transients can be different. Good control over the interfaces and identification of an optimal shuttering sequence is important for the growth of better detector material. This work focuses on improving the performance and understanding of the T2SL detector system by improvement in material growth, device designs and theoretical modeling.

The freedom of changing the bandgap and bandoffset provides an opportunity to realize barrier engineered devices which can lower dark currents significantly compared to homojunction photodiodes. Barrier engineering can be used to design detectors with *smart* barriers, for example, incorporating a barrier which blocks dark carriers but carries out avalanche multiplication of photogenerated carriers. In this work we have designed barrier engineered heterojunction photodetectors that have led to an improvement in the performance of T2SL infrared detectors by orders of magnitude over the last decade, as shown in Fig. 1.4 which records the performance of LWIR devices fabricated at UNM

over the years[23, 35, 36]. Dark current density, which is an important parameter used to evaluate detector performance, has been plotted against years.

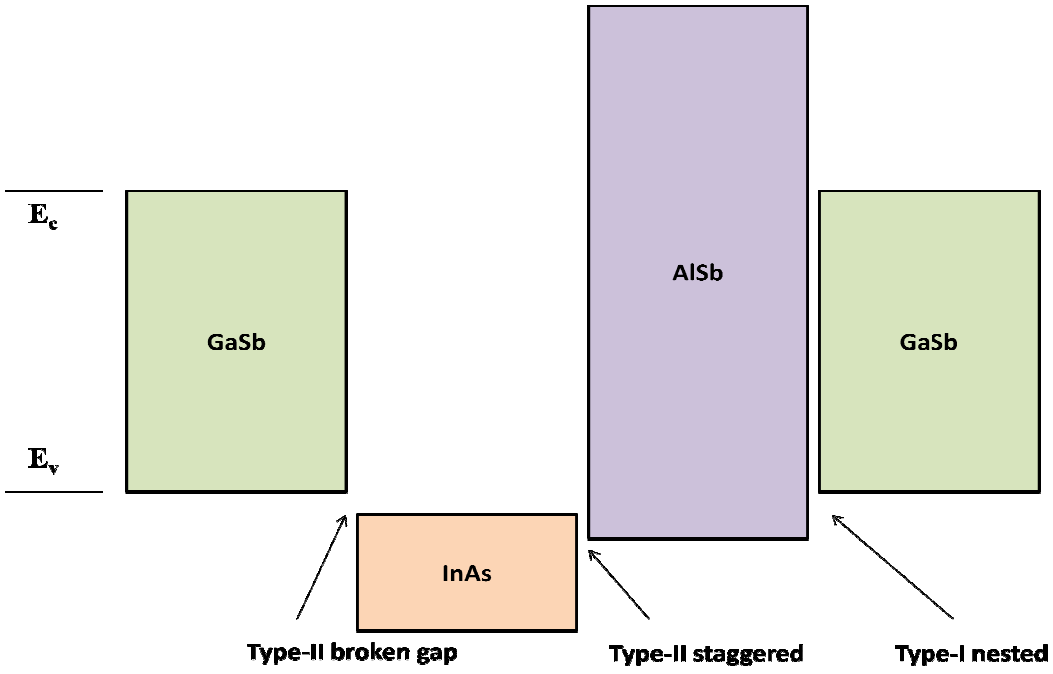


Fig. 1.2 Band lineup between InAs, GaSb, and AlSb showing type-II broken gap alignment, type-II staggered alignment, and type-I nested alignment for InAs/GaSb, InAs/AlSb, and GaSb/AlSb, respectively.

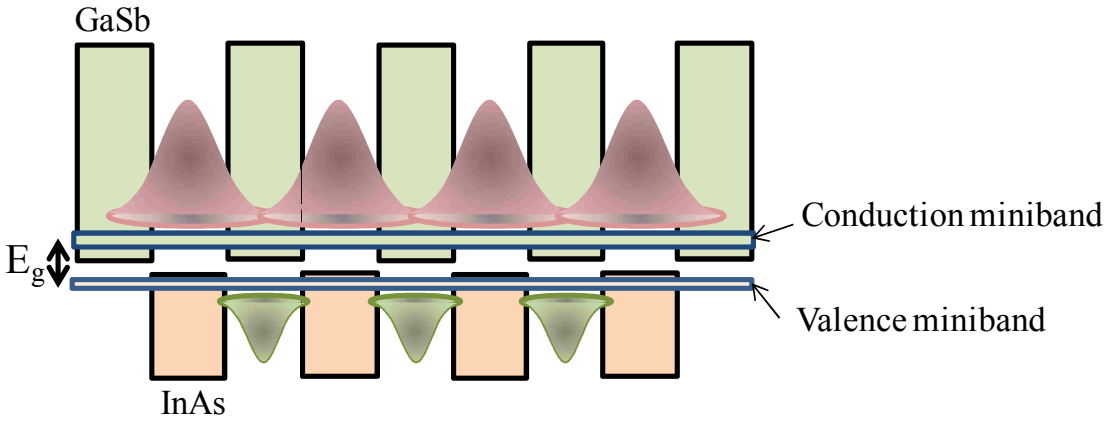


Fig. 1.3. Type-II band alignment between InAs/GaSb thin alternating layers results in T2SL and the formation of minibands due to the overlap of wavefunctions with electrons primarily confined in InAs layers and holes confined in the GaSb layers.

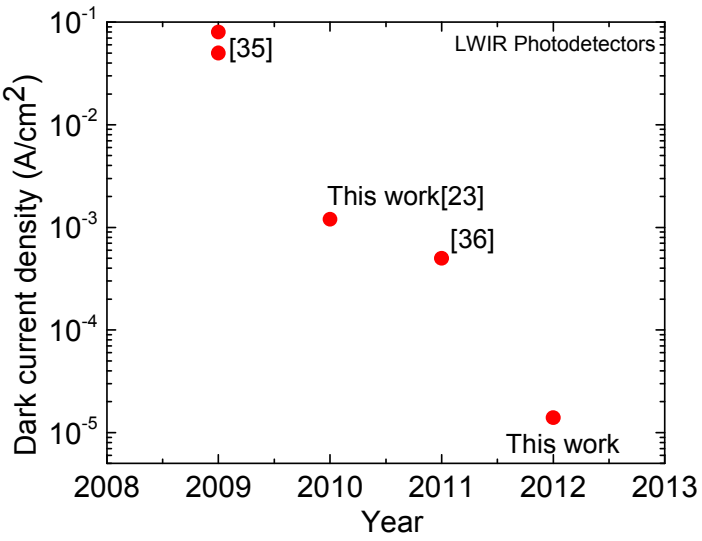


Fig. 1.4 Improvement in dark current density for past four years has been shown for T2SL LWIR devices fabricated at UNM.

## 1.4 Contributions of this Dissertation

This work has been aimed at improving the T2SL technology for the realization of high performance detectors. This has been carried out by studying the material properties and engineering the bandgaps/bandoffsets of T2SL detectors. In the material study, we carried out polarization dependent photocurrent spectroscopy to understand the nature of quantum confined minibands in the valence band and correlated the experimental results with theoretical simulations. This study established the nature and ordering of valence minibands with increase in energy. As mentioned earlier, interfaces play an important role in deciding the quality of the T2SL material. A systematic study was carried out to study the effect of different interfaces on the T2SL material using variable temperature photoluminescence (PL), high resolution x-ray diffraction (XRD) and the effect was subsequently studied on the detector performance.

As a part of this thesis, the bandstructure of T2SL was simulated using empirical pseudopotential method (EPM)[37]. These simulations were used extensively to design band-engineered photodetectors. In order to improve the performance of T2SL infrared detectors, a novel heterojunction architecture, pBiBn, which consists of electron and hole blocking layers to reduce dark currents, was proposed. pBiBn detectors for MWIR and LWIR detection were demonstrated. In the first generation of pBiBn LWIR detector, we found that the dark current improved by more than two orders of magnitude over a conventional PIN design[23]. In the second generation of LWIR pBiBn detector, barrier layers, absorber doping, and contact layers were optimized, which resulted in performance close to the state of the art in T2SL technology. This concept was further extended to realize multicolor detectors. A concept of barrier-APD was put forward in this work, where a barrier layer (made of T2SL), blocks dark current while multiplying the photocurrent. Band-engineering was further used to design high operating temperature interband cascade detectors based on T2SL for MWIR and LWIR applications. One stage of cascade detector consists of three main regions; the absorber region, relaxation region, and interband tunneling region. Different regions were designed using EPM simulations and a one dimensional Schrödinger solver. The detector architecture consists of seven stages, which leads to an inherent photoconductive gain in the system. The MWIR cascade detector demonstrated high operating temperature, with spectral response measured up to 420K.

## 1.5 Outline of the Dissertation

This dissertation is organized in two sections. The first section is ‘Materials Research’ of T2SL infrared detectors, which consists of chapter 2 through 4. In chapter 2, different

steps in the detector fabrication such as epitaxial growth, material processing, and material and device characterization techniques are discussed. Issues related to the epitaxial growth and detector processing are also highlighted. In chapter 3, a T2SL electronic bandstructure modeling approach is discussed. Bandstructure and wavefunctions of different T2SL systems are presented in this chapter. In chapter 4, details of the polarization dependent photocurrent spectroscopy along with theoretical simulations are presented. It also talks about the effect of interfaces on the T2SL material quality as well as on the performance of the detectors.

The second section is “Barrier Engineering”, which includes chapters 5, and 6. In chapter 5, the heterojunction barrier engineered architecture, pBiBn, is discussed for MWIR and LWIR applications. It also explains the use of barrier layers for realizing multi-color detectors. In Chapter 6, interband cascade photovoltaic detectors based T2SL are discussed. The design aspects, simulations and growth complexities are highlighted. It shows the results for MWIR and LWIR cascade detectors. Finally, chapter 7 is devoted to discussions about conclusions from this work and identifying the key areas for future work such as Barrier-APDs.

Two appendices have been provided at the end of the thesis. Appendix A provides a detailed growth recipe for heterojunction pBiBn T2SL detector, while Appendix B details all the bulk form factors used for the simulation of the T2SL bandstructure using the empirical pseudopotential method.

# 2 Methods

Key ingredients required to make a high performance detector are modeling, epitaxial growth, fabrication and then characterization. This chapter gives a brief description of the methods used in the course of this work. It covers all the important aspects of epitaxial growth using MBE, including techniques such as high resolution x-ray diffraction and photoluminescence for characterization of material. It also covers the fabrication steps for photodetectors based on T2SL, and detector characterization using black body and variable temperature dark and photocurrent measurements.

## 2.1 Theoretical Modeling

Theoretical modeling of any material system is important for a better understanding of its physical properties and for device oriented research. It is an important tool for high performance device designs. Theoretical modeling of InAs/GaSb/AlSb T2SL was carried out as a part of this work and empirical pseudopotential method (EPM)[37] was used for this purpose. The details of the theoretical modeling, procedures and results have been discussed in detail in chapter 3. The advantage of EPM is that it gives band offsets as well as bandgaps of different T2SLs. Once the absorber T2SL is decided, contact layers and barrier layers can be suitably designed using information from EPM codes. With the help of this information, high performance heterojunction photodetectors were designed, which is discussed in chapter 5 and 6. The next step is the epitaxial growth of T2SL, described blow.

## 2.2 Epitaxial Growth

Epitaxial growth of T2SL system is very sensitive with respect to growth parameters such as growth temperature, shutter sequence, flux ratios and doping. In this work, most of the material growth has been carried out in a VG Semicon (V80H) molecular beam epitaxial system. Growth of T2SL detectors was optimized with respect to growth temperature, and flux ratios. While no detector structure was grown on CHTM's Veeco Gen10 MBE chamber for this work, a systematic calibration study was carried out on it and optimal growth conditions were established for T2SL detector growth. The schematics of MBE machine is shown in Fig. 2.1[38]. The source panel in the MBE system contains three dopant cells; Si and GaTe for n-type and Be for p-type doping. It also has Ga, Al, and In group III sources and group V sources such as Arsenic with valved cracker and Antimony unvalved cracker source. The system is always maintained under ultrahigh vacuum (UHV) in order to reduce the defect density and background doping concentration in the growth epilayers.

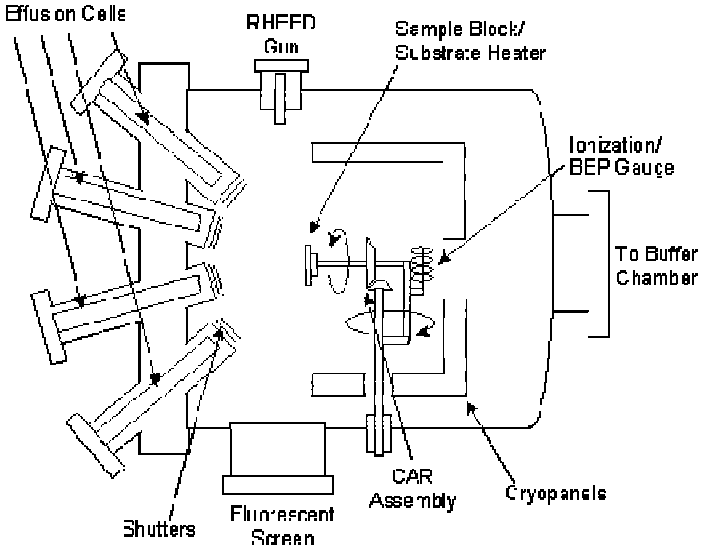


Fig. 2.1. Schematic of the molecular beam epitaxy (MBE) reactor

MBE growth of InAs/GaSb T2SL is carried out on GaSb substrates. Presently, 3" substrates are available from several vendors, who have also been working on developing better quality 4" substrates [39]. However, for this work, only 2" substrates were used. The lattice constant of GaSb, InAs, and AlSb are 6.09593Å, 6.0583Å and 6.1355Å, respectively. InAs is tensile strained while AlSb is compressively strained on GaSb, with -0.62% and 0.65% strain, respectively. Unless the strain in each period of InAs/GaSb or InAs/AlSb T2SL is compensated, it is not possible to grow thick detector structures, due to formation of threading dislocations to relax strain. For this purpose, each period of InAs/GaSb T2SL is strain compensated with a very thin layer of InSb, which has a lattice constant of 6.83012Å and a compressive strain of 6.2%. The details of strain compensation in T2SL detectors are discussed in chapter 4. In a typical growth sequence, the fluxes of different sources are measured to decide the valve setting of As and power setting of Sb base (as mentioned earlier, Sb source was unvalved), to achieve desired growth rates and flux ratios. After that, the substrate is loaded inside the chamber and heated under group V (Sb) flux up to 535$^{o}$C for oxide desorption. The temperature is measured with a calibrated pyrometer. Oxide desorption is marked by obtaining a bright streaky reflection high energy electron diffraction (RHEED) [40] pattern. After the oxide desorption, a GaSb buffer layer of 300-500 nm thickness is grown to smoothen the surface, before continuing on to the growth of the rest of the structure. Typical growth rates for In and Ga are 0.35ML/s and 0.4ML/s, while T2SL growth temperature is typically 390-410 $^{o}$C. A detailed growth recipe for growth of a LWIR pBiBn detector is given in Appendix A.

### 2.2.1 Growth Calibrations

A growth campaign starts with various calibrations, in which growth rates and doping densities are calibrated. For growth rate calibrations, RHEED intensity oscillations are used. For this, a small sample (typically 3-4 mm side squares) is mounted on a molybdenum plate. The RHEED pattern is obtained after oxide desorption. The sample surface is smoothened by growth of a thick buffer layer; this step helps in getting good RHEED oscillations. The intensity oscillations are observed after both group III and V shutters are open. During two consecutive readings, the surface is recovered under group V flux. This procedure is repeated several times (4-5 times) at each of 4-5 different source temperatures. A line fit through the Arrhenius plot of the log of growth rate against 1/T, where T is source temperature, gives the equation for growth rate at different source temperatures under those conditions. A typical Arrhenius plot of growth rate vs. 1/T, obtained from the left hand side (LHS) chamber of the V-80H MBE is shown in Fig. 2.2. For T2SL growths, the growth rates are confirmed with XRD as well by growing superlattices of two different compositions and solving the linear equation involving growth times, growth rates, and period thickness of superlattices (obtained from XRD data).

For doping calibrations, thick GaAs layers (typically 3 μm) are grown on semi-insulating GaAs substrate by changing the dopant cell temperature to get different doping concentrations. GaSb substrates cannot be used because of their conducting nature. Hall measurement in Van der Pauw configurations are carried out to measure the doping density. A linear fit of the data gives doping density for different dopant temperatures for a given growth rate, and can be scaled to a desired growth rate.

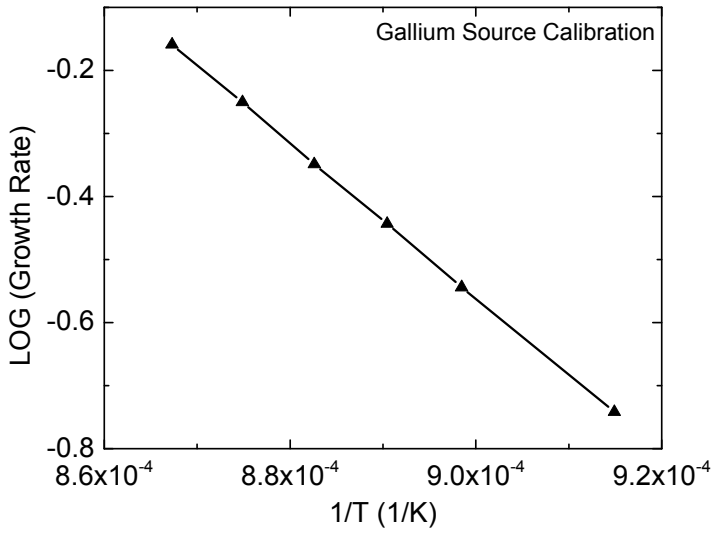


Fig. 2.2. Arrhenius plot of log of Gallium cell growth rate against inverse of cell temperature obtained from LHS of V80H chamber.

### 2.2.2 Growth Parameter Optimization

MBE growth of T2SL detectors is optimized by growing a number of samples under different growth conditions and comparing their performances. The details of the growth optimization procedure carried out in the Gen10 MBE system is provided below. For this purpose, a MWIR detector structure was grown at different temperatures and flux ratios for XRD, PL, and detector performance evaluation. The MWIR detector consisted of 8 monolayers (ML) InAs/8 ML GaSb T2SL, where a 1ML thickness of a compound semiconductor is for half its lattice constant on the substrate under consideration. It is advantageous to use MWIR T2SL for growth optimization as it is easier to get PL signal from it. The schematic of the detector structure is shown in Fig. 2.3(a). InSb layers and Sb-soak times were used for strain compensation. While Sb-soak time was fixed to 0.6s, InSb layer thickness was changed so as to strain balance the T2SL. Fig. 2.3(b) shows the shutter sequence of group V and group III species for one period of 8ML InAs/8ML

GaSb T2SL, assuming growth rates of 0.4ML/s. It is to be noted that the thickness of InSb layer needs to be adjusted to achieve lattice matched T2SL structure. The P and N contact layers were doped with Be and GaTe, respectively.

For growth temperature study, detectors were grown at 380ºC, 400ºC, and 420ºC. For this study, V/III beam equivalent pressure (BEP) ratios of 5 and 7 were used for GaSb and InAs, respectively. Fig. 2.4(a) compares room temperature PL (RTPL) obtained from these three samples and Fig. 2.4(b) compares full width half maximum (FWHM) and strain of first order satellite peaks measured from XRD. The strength of RTPL increases with the increase in growth temperature, however the change in strength from 400ºC to 420ºC is not significant. XRD data confirms that the structural quality was better for a 400ºC growth temperature. Since optimal detector performance is the ultimate goal of this study, single pixel detector structures were fabricated from these samples. The detector fabrication details have been provided later in this chapter. The normalized spectral response, which realtes photocurrent generation information to wavelength, is shown in Fig. 2.5(a), which shows a cutoff wavelength of 5μm for all three samples. Fig. 2.5(b) compares responsivity and specific detectivity ($D^*$) of three samples at 77K. The terms responsivity and detectivity are described later in this chapter, so for now we can define responsivity and detectivity as a measure of quantum efficiency (QE) and signal to noise ratio (SNR), respectively. We find that the responsivity increases with increase in growth temperature, which is due to the improvement in the crystalline quality of the material. Growth temperature of 380ºC demonstrated the lowest $D^*$, while 400ºC showed a slightly better $D^*$ than 420ºC. Though the responsivity is higher for 420ºC than 400ºC

by a factor of 1.2, better noise performance and better crystalline quality establish 400ºC as the optimal growth temperature.

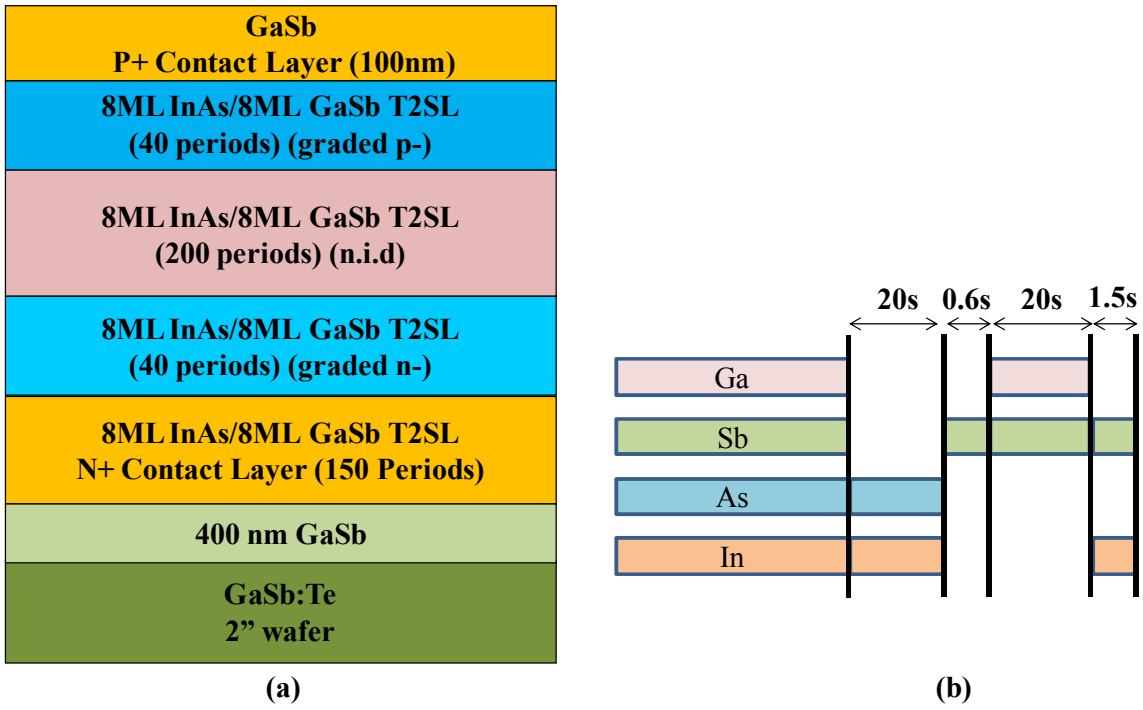


Fig. 2.3. (a) Structure schematic of MWIR detector showing absorber and contact layers, (b) shutter sequence for one period of 8ML InAs/8ML GaSb T2SL, depicting the strain compensating layers as well.

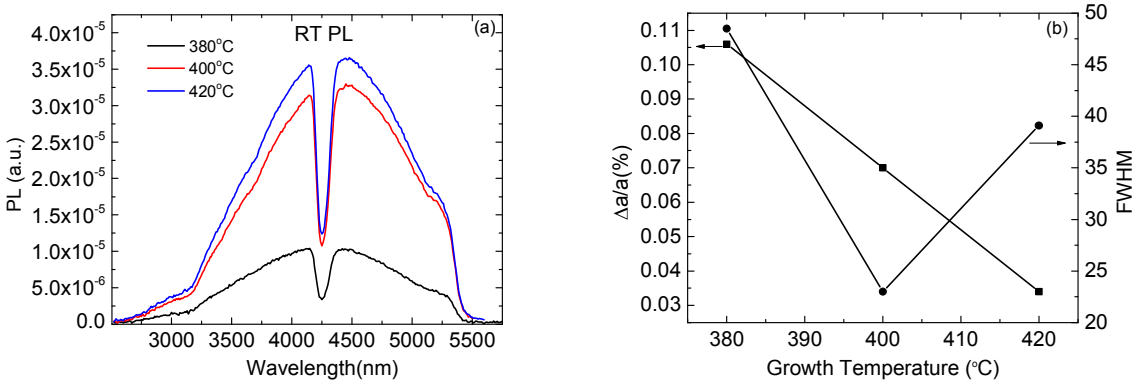


Fig. 2.4. Comparison of RTPL data and (b) XRD data showing strain and full width half maximum (FWHM) of MWIR detector grown at different temperatures (380, 400 and 420$^{o}$C)

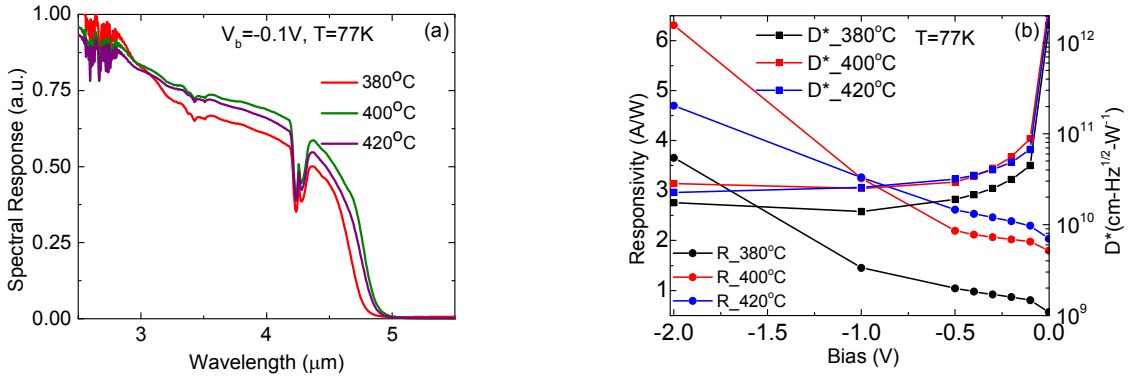


Fig. 2.5. Comparison of (a) spectral response and (b) responsivity and specific detectivity of MWIR detectors grown at different temperatures at 77K.

For the next optimization step, which involved group V/III flux ratios, all growths were carried out at 400ºC. In this study, first Sb/Ga BEP flux ratio was initially kept fixed at 5, while As/In ratio was varied as 5, 6, 7 and 9. As before, XRD and RTPL measurements were carried out and then detector performances were compared. The results showed that As/In=5 demonstrated the best detector performance with the highest responsivity and detectivity, though the RTPL was maximum for As/In=6, which is shown in Fig. 2.6(a). This shows that the material level characterization such as XRD and PL are necessary but not sufficient to estimate the detector performance, as electrical transport also plays an important role. To study the effect of Sb/Ga flux ratio, the As/In flux ratio was set to 5 and the growth temperature at 400ºC. Sb/Ga flux ratio was then changed to 4 and 3. The detector performance at 77K, with responsivity and *D** data, has been shown in Fig. 2.6(b). It is clear that the responsivity reduces drastically with respect to decreased Sb/Ga flux ratios. From this study, we concluded that, for the Gen10 MBE at UNM, optimal growth temperature is 400ºC, As/In (BEP) ratio=5, and Sb/Ga(BEP) ratio=5. These

conditions may not apply to other MBE reactors as they depend on the position of sources on the source panel and the location of the beam flux gauge with respect to the substrate. For example, on the LHS chamber of the V80H MBE, the optimal BEP ratios for As/In and Sb/Ga are 9.2 and 3.8, respectively. Please note that this flux optimization on the LHS chamber was done with an unvalved Sb cracker source.

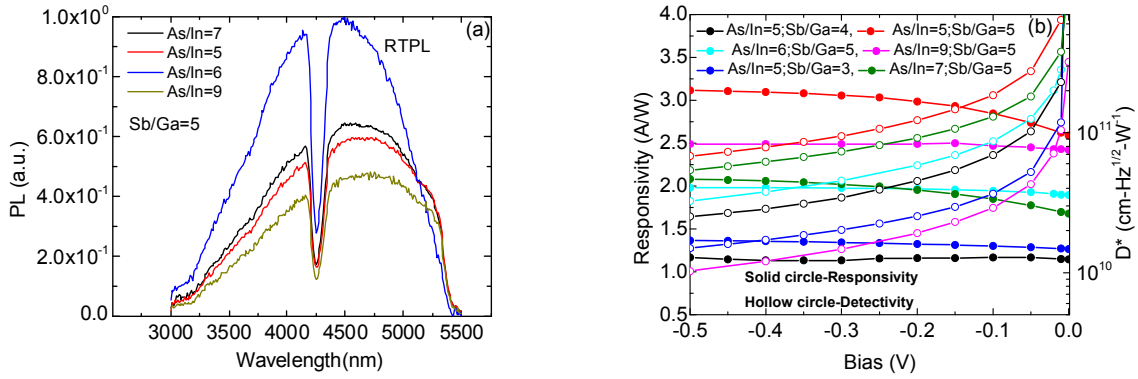


Fig. 2.6. (a)Comparison of RTPL data for samples grown with Sb/Ga ratio of 5 and different As/In ratios, (b) Comparison of 77K responsivity and specific detectivity as a function of bias at 77K, where hollow circles represent D* and solid circles represent responsivity.

## 2.3 Device Fabrication

## 2.3 Fabrication

Once grown, the material is processed into an array of single pixel detectors. This process involves the following steps, which are performed in the cleanroom. Contact lithography is used to define the patterns in photoresist for every step. A detailed single pixel device fabrication process has been given in [41].

1. Mesa etching: This is the first step, which involves inductively coupled plasma (ICP) etching for vertical sidewalls. The mesa etching for most of this work was done using

$BCl_3$ gas in the ICP chamber. The sidewalls may be further smoothened by wet chemical etching using phosphoric acid based solutions to reduce the surface roughness.

2. Contact metallization: For T2SL detectors, both P and N ohmic contacts are made with Ti/Pt/Au (500/500/3000Å). It is important to do a premetallization acid dip in (1:10) ($HCl:H_2O$) to remove native oxide. Afterwards, the sample should be cleaned and put in the metal evaporation chamber immediately.

3. Passivation: Passivation is indispensable for T2SL photodiodes. Surface leakage current is a technological challenge in T2SL detector system. The sidewalls of the mesa can be protected with a number of passivation schemes as provided in [42]. In this work SU8[43], which is an epoxy based photoresist, and silicon-dioxide ($SiO_2$) were used.

## 2.4 Characterization

Several characterization techniques have been used in the course of this work. These can be broadly classified as material characterization and device characterization. A brief description of all the techniques has been given below.

### 2.4.1 Material Characterization

Material characterization includes important techniques to obtain quick feedback about the material quality before fabrication. Some of the tools used in this work are high resolution x-ray diffraction, photoluminescence, and hall measurement setup.

**Photoluminescence**

Photoluminescence (PL)[44] is an extremely important technique for T2SL material characterization. The setup at CHTM has variable temperature PL characterization ability, but the optics, spectrometer, and detector can only be used for MWIR PL

measurements. Measurements can be undertaken from 10K to room temperature PL. For T2SL samples, a high power Argon ($Ar^{++}$) ion laser with power range from (1-2Watts) is used. Liquid nitrogen ($LN_2$) cooled indium antimonide (InSb) detector was used to detect MW PL signal. An example RTPL signal from a MWIR sample, measured using this setup, has been shown in Fig. 2.3(a). Use of PL data for comparison of detector performance has been described in chapter 4.

**X-Ray Diffraction**

XRD is the most important tool for characterization of T2SL materials and gives a large amount of information related to the crystalline quality. The physics behind the XRD setup can be found elsewhere[45]. This dissertation covers the steps required to use the setup for extracting information about the material. A typical, XRD spectrum of a T2SL LWIR sample has been shown in Fig. 2.7, after a symmetric (004) omega-2theta scan. The effective lattice constant of the T2SL is different from that of the substrate and is determined by the thickness and composition of each layer in one period of T2SL. The difference between the $0^{th}$ order T2SL peak ($P_{0th}$) and the GaSb substrate peak ($P_{GaSb}$) positions normalized by the substrate peak position gives the percentage of strain in T2SL.

$$\frac{\Delta a}{a} = \frac{(a_{T2SL} - a_{GaSb})}{a_{GaSb}} = \frac{(P_{0th} - P_{GaSb})}{P_{GaSb}} \tag{2.1}$$

Where, for $m$ ML InAs/$n$ ML GaSb T2SL, $a_{T2SL} = \frac{m \times a_{InAs} + n \times a_{GaSb}}{2(m+n)}$, $a_{InAs}$ and $a_{GaSb}$ are normal to the growth plane lattice constants of InAs and GaSb, respectively, on GaSb. The separation between the +1 and -1 order superlattice peaks, which can be changed

from degrees into arc-seconds, can be put into the peaksplit program[46] and the period of the T2SL can be obtained. The FWHM of the $0^{th}$ order and $1^{st}$ order peaks is a commonly used parameter to establish the crystalline quality. It is usually reported in arc-seconds in the literature. The narrower the peaks, the better the crystalline quality for the given thickness of the T2SL.

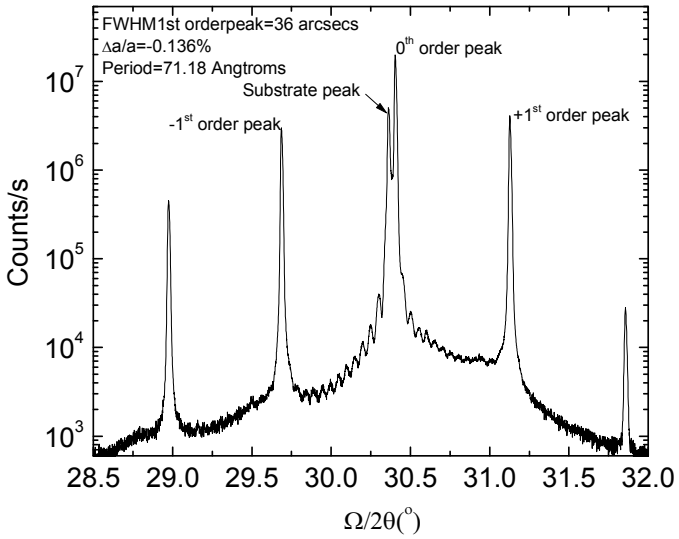


Fig. 2.7. XRD spectrum of a LWIR T2SL detector, showing calculated lattice mismatch, FWHM of first order satellite peak, and period thickness.

**Hall Measurement**

Hall measurement is primarily used to determine the doping density of the material in order to calibrate the dopant source. For reliable measurements, especially at low doping densities, thick (>3 μm) doped layers are desired. Sample preparation involves cleaving the sample in small squares and reflowing Indium bumps on all four corners. Indium is usually annealed to form ohmic contacts at 300ºC for 3-5 minutes. Gold wires are then attached to Indium bumps which are used to pass the current through the device in a Van

der Pauw configuration. The measurement gives an estimate of sheet doping density, type of dopant and mobility of the sample. This measurement can also be used to monitor the background doping in the sample, which gives an idea of the cleanliness of the MBE growth chamber. For this purpose, a standard high electron mobility transistor (HEMT) structure can be grown for improved sensitivity or a very thick GaAs epilayer can be grown for background doping.

### 2.4.2 Device Characterization

After the device is processed, the detector characteristics are measured. In this section, various detector characteristics and figures of merit, such as spectral response, dark current, responsivity, and detectivity are discussed.

**Spectral Response**

Spectral response or photocurrent spectrum of a fabricated detector is measured using a Nicolet 670 Fourier transform infrared spectrometer (FTIR) which is equipped with a broadband infrared glowbar source. The instrument is software controlled and values of different parameters such as resolution and velocity of the scanning mirror of the FTIR can be selected by the user. The spectrum can be corrected for the background in the software and should be corrected with respect to the detector response as well. Spectral response gives the cutoff wavelength of a detector as well as the relative QE at different wavelengths.

**Dark current**

The current that flows through the detectors in the absence of any photon flux is called the dark current. It is usually measured in a variable temperature cryostat with a cold

shield (made of Aluminum) in front of the device and cold finger cooling the device from back side. This arrangement, however, has some error depending on the cold shield temperatures which cannot be at absolute zero. Dark current is a very important figure of merit, since it determines the maximum operating temperature for the detector for a given signal-to-noise ratio (SNR). In T2SL detectors, major sources of dark current are minority carrier diffusion current, SRH current (G-R current), tunneling (trap assisted and band to band) current, and surface leakage current. The performance improvement in a T2SL detector is carried out by reducing the dark current without affecting the photocurrent. Use of unipolar barriers to reduce dark current has been demonstrated in chapter 5.

Dark current data also provides crucial information about the dominant dark current mechanism in the device. Once temperature dependent dark current data is obtained, the log of dark current can be plotted against the inverse of temperature at a particular voltage bias value. Different components of dark current $(J_d)$, described in detail in chapter 5, vary exponentially as a function of temperature.

$$J_d \propto J_0 e^{-\frac{E_a}{kT}} \tag{2.2}$$

Where $J_0$, is either temperature independent or has weaker dependence on temperature as compared to the exponential dependence of the second term of equation (2.2). When $\log(J_d)$ is plotted against $(1/T)$, one gets a straight line, slope of which determines the activation energy. Diffusion dominated dark current has activation energy comparable to the bandgap, while SRH dominated dark current usually has activation energy equal to half of the bandgap, arising from midgap trap states.

**Responsivity**

Responsivity is defined as the amount of photocurrent flowing through the external circuit per watt of optical power incident on the detector. It is typically measured with a calibrated blackbody source radiating photons in the detector response range, which can be calculated by using Planck's law (equation 1.1). Using basic radiometric calculations[1], the number of photons falling on the detector per second can be calculated for the given parameters such as blackbody temperature, aperture size, distance from the detector, detector optical area and the wavelength range of interest. Using these factors, the following formula for responsivity can be derived:

$$R = \frac{I_o}{\int_{\lambda_1}^{\lambda_2} \frac{R(\lambda)}{R(\lambda_c)} L_e(\lambda,T) \frac{A_s A_p A_d}{r_1^2 r_2^2} t_1 t_2 F_F d\lambda} \tag{2.3}$$

where $\frac{R(\lambda)}{R(\lambda_c)}$ is the normalized spectrum of the detector, $L_e(\lambda,T)$ is the radiance, $\frac{A_s A_p A_d}{r_1^2 r_2^2}$ is the solid angle subtended from blackbody onto the detector, in extended source extended detector configuration ($A_s$, $A_p$ and $A_d$ are the area of blackbody aperture, blackbody slit and detector respectively, while $r_1$ and $r_2$ are the distances from the blackbody aperture to the slit and blackbody slit to the detector, respectively). $I_0$ is the measured photocurrent from a detector. Photocurrent is taken out from the detector using BNC connectors, and is amplified in a low noise preamplifier and measured using a spectrum analyzer. The chopper frequency is used as a trigger for the SRS760 fast Fourier transform (FFT) spectrum analyzer. $t_1$ *and* $t_2$ are transmission of windows and any other optics used, and $F_F$ is the form factor which can be calibrated with a detector

with known responsivity (such as InGaAs detector at 77K). This includes chopper loss and any other optical scattering losses.

For photodiode absorption QE can be extracted from responsivity (*R*), using the following equation.

$$\mathrm{QE}(\%) = R(\mathrm{A/W}) \times \frac{1.24}{\lambda(\mu\mathrm{m})} \times 100 \tag{2.4}$$

In the case of a photoconductor, which has an inherent photoconductive gain inside the device, the above formula needs to be modified, with the left hand side becoming conversion efficiency, which is a product of QE and photoconductive gain.

**Detectivity**

Specific detectivity ($D^*$) is a widely used figure of merit for describing the signal-to-noise ratio of a detector, normalized with respect to the detector area ($A_d$) and measurement bandwidth ($\Delta f$). It is defined as,

$$D^*(\lambda) = \frac{R(\lambda)\sqrt{A_d \Delta f}}{i_n} \tag{2.5}$$

where, $i_n$ is the root mean square (rms) noise current. For $\lambda = \lambda_{peak}$, $D^*(\lambda)$ is referred to as peak-specific detectivity, which is often quoted as the figure of merit for a single-pixel detector.

The primary components of noise current in T2SL photodiode are shot noise due to dark current and photocurrent, and thermal noise. The expression for the rms noise current is:

$$i_n = \sqrt{i^2_{Background} + i^2_{Signal} + i^2_{Dark} + i^2_{th}} \tag{2.6}$$

where

$$i_{Background} = \sqrt{2qI_{Background}\Delta f}\ (A_{rms})$$
$$i_{Signal} = \sqrt{2qI_{Signal}\Delta f}\ (A_{rms})$$
$$i_{Dark} = \sqrt{2qI_{Dark}\Delta f}\ (A_{rms})$$
$$i_{th} = \sqrt{\frac{4kT}{R}}(A_{rms})$$

where $q$ is the electronic charge, $I_{Dark}$ and $I_{Signal}$ are the dark current and photocurrents, respectively, $k$ is the Boltzmann constant, $T$ is the absolute temperature, and $R_d$ is the differential resistance of the device. The last term $i_{th}$ is the thermal noise current, also called Johnson noise, and is usually negligible compared to the shot noise.

Noise for detectivity calculations is usually measured with a FFT spectrum analyzer. The device is exposed to 300K background (2π field of view (FOV)). The spectrum of the noise is analyzed. The noise in g-r limit is measured by rms averaging of noise over a certain bandwidth. At low frequency range the noise is dominated by 1/f noise, which is highly dependent on the detector architecture and can be dominated by surface leakage current [47]. For higher frequencies, typically 2-5 kHz, the white noise from generation recombination dominates. After the detector cutoff, which is determined by the carrier lifetime in the material, only Johnson noise ( $i_{th}$) is present. For detectivity measurements, noise is usually measured at 2000Hz, with a long integration time. Care must be taken to operate the preamplifier at highest possible gain, without overloading, in order to maximize the sensitivity (reduce the noise floor) of the measurement.

In the T2SL community, detectivity is reported under different conditions and there are only a few reports of detectivity obtained through actual noise measurements[48].

Detectivity calculated from shot noise due to dark current and thermal noise is the most commonly used method[21, 23, 35, 36, 49, 50]. A number of groups also report detectivity under the Johnson noise limit [51, 52]. Another method is to estimate the total noise by calculating noise due to photocurrent (generation due to background flux), dark current, and thermal noise[22].

# 3 Bandstructure and Device Simulations

This chapter will give a detailed account of simulation methods used in this work. The first section of this chapter talks about the bandstructure simulations of InAs/GaSb T2SL, while the second section focuses on device simulations which have been carried out using Sentaurus TCAD[53].

## 3.1 Motivation

As discussed in chapter 1, the performance of T2SL detectors can be improved by designing heterojunction detector structures. For this, one needs to have a simulation platform which would give bandgaps and bandoffsets of different T2SLs. Though there are a few ready to use softwares, such as nextnano[54], the modification of software to incorporate different superlattice systems such as InAs/AlSb and AlSb/GaSb becomes difficult. Also, one has to use software as a black box and it gives little insight into the understanding of simulation procedure. For this reason, bandstructure modeling of InAs/GaSb/AlSb superlattices was carried out using empirical pseudopotential (EPM). Effectiveness of unipolar barrier incorporation can be judged by looking at the electric field profile across the heterstructure photodiodes. In this work, electric field and bandgap simulations have been carried out using Sentaurs TCAD software, described later in the chapter. The limitations and advantages of the software have also been discussed in this chapter.

## 3.2 Bandstructure Simulations

In the literature, bandstructure simulation of T2SL has been carried out using a number of methods such as k.p method [11, 55, 56], atomistic pseudopotential method[57], empirical pseudopotential mehod[37], and tight-binding method[58]. Without going into the comparison of one theoretical approach with another, we will directly talk about the method used in this work.

We used empirical pseudopotential method as described in [37, 59]. This approach was preferred over other methods due to the ease of implementation, computationally less demanding and lesser number of input parameters needed. Once bulk components are simulated, no special treatment or information is required to simulate a superlattice. In this section we will go over the bulk material simulation and then demonstrate the simulation approach for T2SL. This approach also incorporates coherent strain in the superlattice layers. The understanding of EPM for this work was also supplemented by [60, 61].

**Pseudopotential for Bulk Semiconductors**

In this section, simulation steps for bandstructure of zincblende semiconductors have been discussed. InAs has been used as an example but the approach is very generic. The steps are given below.

1. Start with the time-independent Schrodinger equation, $H\psi_{n,\mathbf{k}} = E_{n,\mathbf{k}}\psi_{n,\mathbf{k}}$
2. Wavefunctions can be expressed in terms of the complete orthonormal set of plane waves, such that $\psi_{n,\mathbf{k}}(\mathbf{r}) = \sum_{\mathrm{G}} a_{n,\mathbf{k}(\mathbf{G})} u_{\mathbf{G},\mathbf{k}}$ , $u_{\mathbf{G},\mathbf{k}} = \frac{1}{\sqrt{\Omega}} e^{i(\mathbf{G}+\mathbf{k})\cdot\mathbf{r}}$ . Here $\Omega$ is

normalization volume and $a_{n,\mathbf{k}(\mathbf{G})}$ are coefficients of expansion, $u_{\mathbf{G},\mathbf{k}}$ represent plane wave, **r** and **k** are the position vector and wave vector, respectively, for electrons.

3. Since, electrons move in a periodic potential inside the lattice, Bloch's theorem has to be satisfied for the wavefunction and the expansion in (2) holds only when **G** represent reciprocal lattice vectors[61].
4. Substitute wavefunction expansion in Schrodinger equation, multiply by complex-conjugate of plane wave $u^*_{\mathbf{G},\mathbf{k}}$, and integrate over all space, which results in the following equation:

   $\sum_{\mathbf{G}} a_{n,\mathbf{k}}(\mathbf{G}) \int u^*_{\mathbf{G}',\mathbf{k}} H u_{\mathbf{G},\mathbf{k}}\, \mathrm{d}\tau = \sum_{\mathbf{G}} a_{n,\mathbf{k}}(\mathbf{G})\, E_{n,\mathbf{k}} \int u^*_{\mathbf{G}',\mathbf{k}} u_{\mathbf{G},\mathbf{k}}\, \mathrm{d}\tau$

   $\Longrightarrow \sum_{\mathbf{G}} a_{n,\mathbf{k}}(\mathbf{G}) H_{\mathbf{G}',\mathbf{G}} = \sum_{\mathbf{G}} a_{n,\mathbf{k}}(\mathbf{G})\, E_{n,\mathbf{k}} \delta_{\mathbf{G}',\mathbf{G}}$, where orthonormality of plane waves has been used.

5. The Hamiltonian for an electron with rest mass $m_0$ is given by $= -\frac{\hbar^2}{2m_0}\nabla^2 + \mathrm{V_C}$, where $\mathrm{V_C}$ is crystal potential. Using this in (4), one gets

   $H_{\mathbf{G}',\mathbf{G}} = -\frac{\hbar^2}{2m_0}|\mathbf{G}+\mathbf{k}|^2 \delta_{\mathbf{G}',\mathbf{G}} + V$, where $V = \frac{1}{\Omega}\int e^{-i(\mathbf{G}'+\mathbf{k})\cdot\mathbf{r}} V_C e^{i(\mathbf{G}+\mathbf{k})\cdot\mathbf{r}} \mathrm{d}\tau$

6. Following the approach in [61] and using the definition of lattice translation vector **T**, potential $V$ can be expressed as

   $V = e^{-i(\mathbf{G}-\mathbf{G}')\cdot\mathbf{T}} \frac{1}{\Omega_{\mathrm{C}}} \int V_a^{cat}(\mathbf{r})\, e^{-i(\mathbf{G}'-\mathbf{G})\cdot\mathbf{r}} \mathrm{d}\tau + e^{i(\mathbf{G}-\mathbf{G}')\cdot\mathbf{T}} \frac{1}{\Omega_{\mathrm{C}}} \int V_a^{an}(\mathbf{r})\, e^{-i(\mathbf{G}'-\mathbf{G})\cdot\mathbf{r}} \mathrm{d}\tau$

   where $V_a^{cat}$ and $V_a^{an}$ are atomic potentials at the site of cations and anions, respectively. $\Omega_c$ is the volume occupied by a single Bravais lattice.

7. Form factor is then defined as $V_f(q) = \frac{1}{\Omega_{\mathrm{C}}} \int V_a(\mathbf{r})\, e^{-i\mathbf{q}\cdot\mathbf{r}} \mathrm{d}\tau$, where $\mathbf{q}=\mathbf{G}'-\mathbf{G}$. The expression for $V$ can be modified to the following equation

$$V = V_f^S(q)cos(\mathbf{G}-\mathbf{G'})\cdot\mathbf{T} + \boldsymbol{i}V_f^A(q)sin(\mathbf{G}-\mathbf{G'})\cdot\mathbf{T}$$

$V_f^S$ and $V_f^A(q)$ are called symmetric and antisymmetric form factors.

8. Equation in step (5) is modified to the following equation

$$H_{\mathbf{G'},\mathbf{G}} = -\frac{\hbar^2}{2m_0}|\mathbf{G}+\mathbf{k}|^2\delta_{\mathbf{G'},\mathbf{G}} + V_f^S(q)cos(\mathbf{G}-\mathbf{G'})\cdot\mathbf{T} + \boldsymbol{i}V_f^A(q)sin(\mathbf{G}-\mathbf{G'})\cdot\mathbf{T}$$

The above equation is then solved for eigenvalues and eigenfunctions for a given electron wavevector **k**. In this work, the eigenvalues and eigenfunctions were obtained by solving equation in MATLAB and using its inbuilt eigen-solver. The eigenvalues are the electron energy levels and eignefunctions give the coefficients of plane wave expansion, $a_{n,\mathbf{k}(\mathbf{G})}$, which can be used to get wavefunctions.

In this theory, form factors are the parameters which are tailored in order to get the bandstructure and physical properties close to the experimental values. The dimension of the eigenvalue matrix depends on the number of terms used in the plane wave expansion of wavefunction. If, say, 15 terms are used in the plane wave expansion, the dimension of matrix becomes 30, where a factor of 2 comes from inclusion of spin degeneracy. The incorporation of spin-orbit coupling[37] in the pseudopotential formalism leads to the pseudopotential spin-orbit matrix element given by the following equation.

$$V^{spin}(q) = \frac{i\hbar^2}{4m^2c^2}\Gamma\langle S|\boldsymbol{\sigma}|S\rangle\cdot(\mathbf{G}-\mathbf{G'})\otimes(\mathbf{G'}+\mathbf{k})V^f(q)$$

where $|S\rangle$ denotes spin orientation and $\boldsymbol{\sigma}$ is a vector of Pauli spin matrices, $V^f(q)$is form factor, $\hbar$ is Planck's Constant over 2π, *c* is speed of light and *m* is free electron mass. The multiplicative factor Γ has been discussed in [37].

**Strain Effects**

InAs is tensile strained on GaSb, and this strain modifies the bandstructure of InAs. The first effect is the hydrostatic shift in the bandgap which is given by the following equation.

$\Delta E = (-a_H) \cdot 2\frac{C_{11}-C_{12}}{C_{11}} \cdot \epsilon$, where $a_H$ is the hydrostatic deformation potential, $C_{11}$ and $C_{12}$ are the elastic moduli, and $\epsilon$ is the strain. This causes InAs bandgap to shrink by 28.8meV. Shear strain breaks the symmetry and lowers it by shortening the *z* direction lattice spacing with respect to *x* or *y* direction, and leads to the degeneracy lifting in the valence band. This effect is taken into account in the EPM formalism by distorting two-atom basis vector **T**, such that $\mathrm{T_z} = \frac{a}{8} \cdot (1 - L \cdot \epsilon)$. Here the empirical parameter $L$ is determined by fitting results for the splitting of the light and heavy hole bands.

Fig. 3.1 shows the bandstructure of bulk InAs. The form factors and other parameters used in the simulation of strained InAs, GaSb and strained AlSb bulk bandstructure have been provided in Appendix B.

**Extension to Superlattices**

In this section we will go over the implementation of pseudopotential technique for the simulation of type-II superlattice bandstructures. Here we present it in context of T2SL made of InAs and GaSb.

Consider a two-component T2SL with period thickness *P* and quantum well thickness (thickness of InAs layer which acts as well for electrons) as *w*. Here we assume that the substrate is GaSb and hence the form factors of InAs coherently strained on GaSb have been used. If we ignore any charge distributions that might occur at the interfaces, then T2SL effective potential can be written as

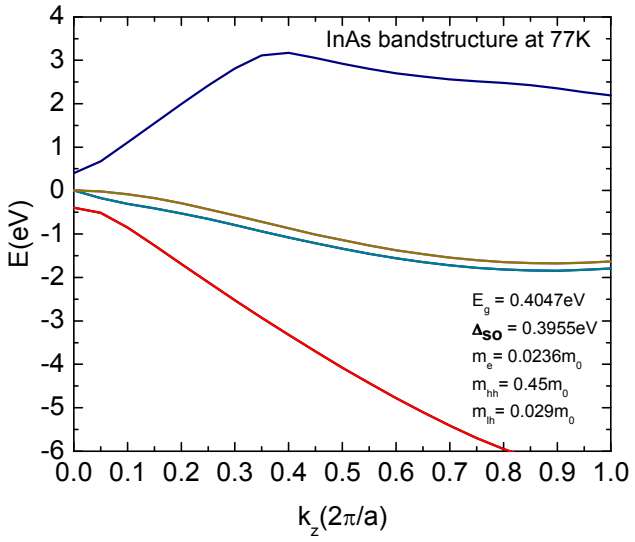


Fig. 3.1. Calculated bandstructure of InAs at 77K along $k_z$ direction. Zero on energy scale specifies valence band maximum.

$$V(r) = rect\left(\frac{z}{w}\right)\sum_G V_G^W e^{i\mathbf{G}.\mathbf{r}} + \left[1 - rect(\frac{z}{w})\right].\sum_G V_G^B e^{i\mathbf{G}.\mathbf{r}}$$

Here,$V_G^W$ and $V_G^B$ are the pseudopotential coefficients, also known as formfactors[62], for the well (InAs) and barrier (GaSb) materials, respectively , *z* denotes the direction normal to the plane of T2SL. The periodic rectangle function can be represented by a finite Fourier series, where center of well has been taken as *z*=0.

$$rect\left(\frac{z}{w}\right) = \sum_{-M}^{M} \frac{1}{n\pi} \sin\left(\frac{\pi w}{P} \cdot n\right) e^{i\left(\frac{2\pi n}{P}\right)\cdot z}$$

$M$ referes to the number of terms in the Fourier seies expansion and can be increased or decreased in order to increase or decrease the sharpness of the interfaces. Using Bloch's theorem for an electron in superlattice, the plane-wave expansion of the wave function can be written as

$$\Psi(\mathbf{r}) = e^{i\mathbf{k}.\mathbf{r}} \sum_G \sum_{n=-N_F}^{n=N_F} \sum_S a_{n,\mathbf{k}}^S(\mathbf{G})\, e^{i\mathbf{G}.\mathbf{r}} e^{i\left(\frac{2\pi}{P}\right)nz} |S\rangle$$

$N_F$ denotes the cutoff for the Fourier series expansion. The wavefunction is then substituted in the Schrödinger equation and one obtains a set of equations for eigenvalues $E(\mathbf{k})$, and the eigenvector components $a_{n,\mathbf{k}}^S$ as

$$\frac{\hbar}{2m}\left[\left|\mathbf{G}_{||} + \mathbf{k}_{||}\right|^2 + \left(\mathrm{G}_z + \frac{2\pi n}{P} + \mathrm{k}_z\right)^2\right] a_{n,\mathbf{k}}^S(\mathbf{G}) + \sum_{\mathrm{G},n} \langle \mathrm{G}ns|V|\acute{\mathrm{G}}\acute{n}\acute{s}\rangle a_{n,\mathbf{k}}^S(\mathbf{G}) = E(k) a_{n,\mathbf{k}}^S(\mathbf{G})$$

Where $\langle \mathrm{G}ns|V|\acute{\mathrm{G}}\acute{n}\acute{s}\rangle$ represents matrix elements of the T2SL potential. The dimension of eigenvalue problem is fixed by the cutoff as $30\cdot(2N_F+1)$, where the first factor is determined by the reciprocal lattice vector cutoff and spin of electron (15 reciprocal lattice vectors taken for plane wave expansion), while the second factors is driven by the spatial frequencies contributed by the superlattice periodicity. Fig. 3.2(a) and (b) show the bandstructure and wavefunction calculated for a 10ML InAs/10ML GaSb T2SL. In case of a superlattice, periodicity is defined by thickness of one period and correspondingly in k-space, one gets mini-Brillouin zone (mBZ) in $k_z$ direction. First mBZ is ($-\pi/P$, $\pi/P$), where $P$ is period thickness. For 10ML InAs/10ML GaSb T2SL, mBZ boundary (at $\pi/P$), in units of $2\pi/a$, is at 0.0506. It can be seen, in Fig. 3.2(a), as the

$k_z$ value around which energy values are mirror image of each other. This position has been marked in Fig. 3.2(a).

Once eigenenergies and wavefunctions are evaluated, the next task is to calculate radiative matrix elements for various transitions. These calculations have been used in theoretical study of polarization sensitive photocurrent spectrum of T2SL. Using Fermi's golden rule and k-selection rule, the momentum matrix element is given by the following equation.

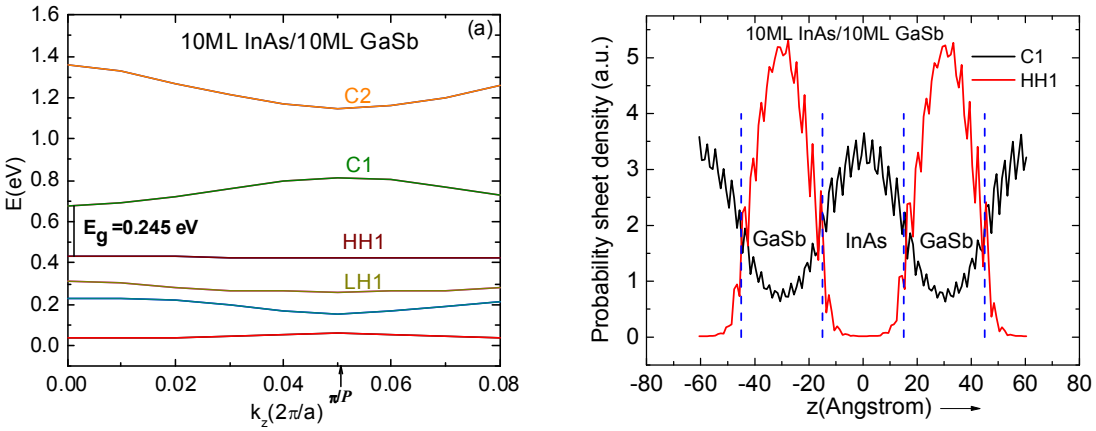


Fig. 3.2. (a) E-k dispersion curve along (001) direction, (b) calculated electron and heavy hole 1 wavefunctions.

$$p_{if} = \frac{1}{Vol}\int \Psi^{*}_{k,\acute{\imath}}(\hat{a}\cdot\vec{p})\Psi_{k,l}\, d^3\mathbf{r}$$

where $\Psi^{*}_{k,\acute{\imath}}$ is the complex conjugate of the final conduction miniband state and $\Psi_{k,l}$ is the wavefunction of the initial valence miniband state, $\hat{a}$ is the unit vector in the direction of electromagnetic field, $\vec{p}$ is the momentum operator, $Vol$ is the volume of the space and $\mathbf{k}$

denotes electron wave-vector as defined earlier. This expression can be shown to reduce to the following expressions for light polarized in *x*, *y* and *z* directions.

$$p_{if}\big|_x = \hbar \sum_{\mathbf{G},n} \sum_{s=\pm} \left(b^s_{\mathbf{G},n}\right)^* (\mathrm{G}_x)\left(a^s_{\mathbf{G},n}\right)$$

$$p_{if}\big|_y = \hbar \sum_{\mathbf{G},n} \sum_{s=\pm} \left(b^s_{\mathbf{G},n}\right)^* (\mathrm{G}_y)\left(a^s_{\mathbf{G},n}\right)$$

$$p_{if}\big|_z = \hbar \sum_{\mathbf{G},n} \sum_{s=\pm} \left(b^s_{\mathbf{G},n}\right)^* \left(\mathrm{G}_z + \frac{2\pi n}{P}\right)\left(a^s_{\mathbf{G},n}\right)$$

where $a^s_{\mathbf{G},n}$ and $b^s_{\mathbf{G},n}$ are components of valence sub-band and conduction sub-band eigenvectors, respectively, **G** is the reciprocal lattice vector and $\mathrm{G}_x$, $\mathrm{G}_y$ and $\mathrm{G}_z$ are its *x*, *y* and *z* components, respectively. Radiative matrix element in energy units is given by the expression $2\left|p_{if}\right|^2/m_0$. Theoretical calculations of radiative matrix element for different T2SL compositions have been presented in chapter 4.

## 3.3 Device Simulations

Device simulation for IR T2SL detector structures were carried out in a commercial Sentaurus TCAD[53] software. The simulations were only intended to generate the heterojunction band profile at a given applied bias and electric field profile across the detector structure. However, Sentaurus does not have GaSb and AlSb in its database. To circumvent this issue, each T2SL was defined as a new material system and included in the database. There are some limitations in making T2SL parameter file as the physical properties of T2SL are not known very well. For this purpose, refractive index was taken as the weighted average of InAs and GaSb refractive indices for InAs/GaSb T2SL, carrier effective masses were taken from [63], Shockley Read Hall (SRH) lifetimes were taken from [28] and carrier mobility was again defined as the weighted average of mobilities in

InAs and GaSb. Other shortcomings of TCAD program are the absence of dopants used in material growth, for example GaTe, and convergence issues. Also the intrinsic doping type in T2SL is not known very well [64-66], which poses some limitation in accurately simulating the bandgap profile at different temperatures. Nevertheless, Sentaurus TCAD can be used to simulate the bandgap profile of a heterostructure and it is indeed a very good tool for comparative study of different heterostructures. Fig. 3.3(a) gives the schematic of a heterostructure diode, the details of which have been given in chapter 5. Fig. 3.3(b) is the simulated electric field and bandgap profile of the heterostructure at equilibrium.

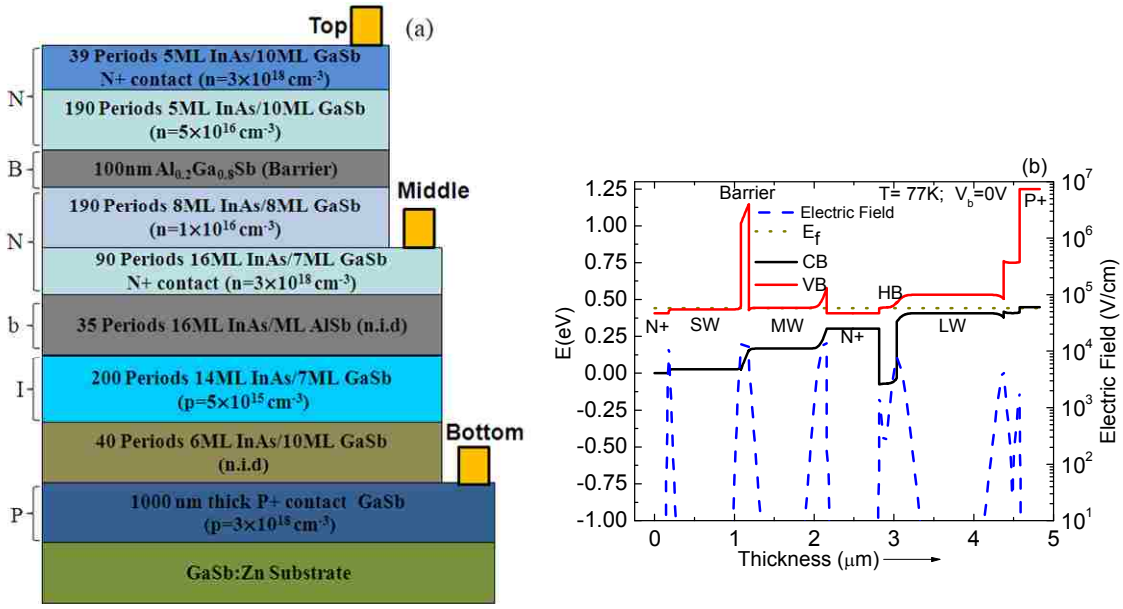


Fig. 3.3. (a) Heterostructure schematic and (b) simulated electric field and bandgap profile at equilibrium and 77K, for a three terminal three contact detector.

In conclusion, T2SL bandstructure can be simulated using EPM. The ease of implementation and computational time favor this technique. Once bulk materials have been simulated, the extension of technique to T2SL is straightforward. Results of bulk as

well as T2SL bandstructure have been presented. Use of Sentaurus TCAD to simulate T2SL band profile was discussed along with all the limitations of the modeling tool.

# 4 Type-II Superlattice: Material Study

In this chapter material aspects of InAs/GaSb T2SL have been discussed. Development of high performance detectors based on any material becomes easier with sound understanding of the system. The understanding can be developed at multiple fronts such as material growth, physical properties of the system as well as the device properties. In this chapter we focus on improving the performance of T2SL detectors by optimizing the material growth. For this purpose, a systematic study of different types of interfaces for MWIR T2SL detector was carried out. Structures were grown with combinations of uncontrolled interfaces and interfaces controlled with soak times, growth interruption and incorporation of InSb, were grown and room temperature photoluminescence (RTPL) was measured. Further, radiometric characterization of the three best interfaces detectors was performed. The design of experiments, growths and characterization of material and devices are discussed in the first section of this chapter.

Although detector applications of T2SL have led to a significant technological progress [67-69], the physics behind the material system is not yet very well understood. For example, the exact nature of the quantum confined interband transitions between the hole levels and the electron levels is unclear. Even though it is generally accepted that the band edge states are dominated by a transition from the lowest confined electron level in the conduction band (C1) to the highest lying heavy hole level in the valence band (HH1), the sequence of higher energy transitions has not been well established. Different theoretical methods have been applied to understand the bandstructure, electronic and

optical properties of superlattices [11, 37, 56, 70, 71]. There has been a number of contradicting theoretical ventures at identifying the ordering of minibands. It has been suggested in the literature that valence subbands are ordered as HH1, LH1, HH2 with increasing hole energy[72, 73], while elsewhere the theoretically suggested ordering is HH1, HH2, LH1[56, 74, 75]. In this work, we carried out polarization sensitive photocurrent spectroscopy in T2SL diodes, which has enabled us to identify electron confined levels and hole-confined levels in both MWIR and LWIR T2SLs. After correlating the experimental observations with the theoretical results, it has been concluded that the quantum confined transitions are ordered as C1-HH1, C1-LH1, C1-LH2 and C1-HH2, respectively. We go over all the experimental and theoretical details in the second part of the chapter.

## 4.1 Interface Study

Interfaces play an important role in dictating the performance of T2SL devices. Presently, T2SL based detectors are limited by Shockley-Read-Hall (SRH) recombination[76]. SRH generation-recombination dark currents are possibly caused by the presence of bandgap defect states and the interfacial states, owing to the interface roughness, which act as recombination sites for photogenerated carriers. The impact of interfaces on T2SL optical properties and bandstructure has been analyzed theoretically [30, 77] in the literature. The effect of interface roughness scattering on the electron mobility in InAs/GaSb T2SL has been explored by Szmulowicz *et al*[78]. Haugan *et al*[79] have discussed the effect of interface and strain on crystallographic quality through high resolution x-ray diffraction (XRD) and atomic force microscopy (AFM). The nature of interface bonds at InAs/GaSb hetero-interface has also been analyzed by Steinshnider *et al*[32] with the help of cross-

sectional scanning tunneling microscope (XSTM). This becomes particularly important because of non-common cation and anion interface between InAs and GaSb. The interface bonds between InAs and GaSb layers can be 'GaAs' or 'InSb' or mixed 'Ga-In-As-Sb' type bonds. One can control 'GaAs' or 'InSb' type bonds at the interfaces by the use of ultrathin GaAs/InSb layers or $As_2/Sb_2$ soak times. In this study, different interfaces have been obtained by a combination of uncontrolled interfaces, interfaces controlled with group V soak times, growth interruption and incorporation of InSb. A systematic study was carried out to select three best interface structures for MWIR T2SL growth on the basis of RTPL data, and the detector performances of these three structures have been compared to find out the best suited interface for MWIR T2SL detectors.

### 4.1.1 Experimental Details

The samples for interface study were grown under identical conditions on GaSb:Te substrates. For all the samples in this study, GaSb buffer layer of thickness 500nm preceded the growth of T2SL structure. For T2SL growth, group V fluxes were adjusted so as to achieve V/III beam equivalent pressure (BEP) ratio equal to 4 for GaSb and 6.5 for InAs. GaSb buffer layer was grown at $500^{o}$C on pyrometer, while T2SL growth was carried out $T_t$-$40^{o}$C, where $T_t$ is reconstruction transition temperature[80] between (1x3) and (2x5) RHEED patterns. The schematics of various interface structures are shown in Fig. 4.1(a), where thicknesses have been specified for 8ML InAs/ 8ML GaSb (8/8) T2SL. We call "InAs on GaSb" interface as tensile interface while "GaSb on InAs" interface as compressive interface. In the beginning we grew two MWIR structures made of 6ML InAs/10ML GaSb (6/10) and 8/8 T2SLs, with interface type (A) and (B). Please note that in all the structures, thickness of InSb layer and the soak times were adjusted so as to

achieve lattice matching. In structure (A), tensile interface is forced to become InSb type by the growth of a thin layer of InSb, which also serves the purpose of strain compensation, while the compressive interface is uncontrolled. In structure (B), tensile interface is uncontrolled and compressive interface is InSb type. The comparison of RTPL data for 6/10 and 8/8 T2SL has been shown in Fig. 4.1(b), for interface scheme (A) and (B).

The PL measurements were carried out using Argon ion laser and liquid nitrogen cooled InSb detector, as described in chapter 2. It indicates that, for both the samples, interface scheme (A) results in higher RTPL signal than (B). The intensity of PL depends on radiative as well as nonradiative lifetimes[81] and higher PL intensity is indicative of longer nonradiative carrier lifetime. Since nonradiative lifetime is determined by the traps and interfacial defects, this indicates that the interfacial quality of T2SL improves more by promoting InSb bonds on tensile interface than compressive interface.

### 4.1.2 Results and Discussion

Next series of growths were designed to control both the interfaces. For this purpose, 8/8 T2SL was selected and all the structures were grown consecutively to avoid growth variations. Structure (C) has been optimized with $Sb_2$ and $As_2$ soak times[82], where compressive and tensile interfaces are controlled by $Sb_2$(12seconds (s)) and $As_2$ (2s) soaks to promote InSb and GaAs type bonds, respectively. The soak times were taken from reference [82], where they were adjusted to achieve strain balancing. Structure (D)[32] has InSb type bonds at both the interfaces, where $Sb_2$ soak time (12s) has been used at compressive interface while growth interruption (2s) has been used at tensile interface. Finally, structure (E) has InSb like bonds at both the interfaces, similar to

structure (D), but with the use InSb layer (0.5ML) at tensile interface and $Sb_2$ soak time (1.3s) at compressive interface. In this campaign, 8/8 TSL was also grown with interface (A) and (B), for comparison with other schemes. Fig. 4.1(c) compares the RTPL data of 8/8 T2SL for different interface schemes. It is to be noted that the cut-off of PL signal at 5.5μm wavelength is due to the cut-off wavelength of the liquid nitrogen cooled InSb detector used for measuring PL signal. RTPL data shows that the intensity of structure (C) is less than that of structure (A), which suggests that supporting GaAs type bonds reduce PL intensity and hence the optical quality of the structure and possibly decrease nonradiative lifetime. Structure (D) has a higher RTPL intensity compared to structures (A), (B) and (C). This indicates that InSb type bonds at both the interfaces give better optical quality and carrier lifetimes. However, soak times and growth interruptions lead to a significant increase in the growth time. For example, at a typical growth rate of 0.4ML/s for InAs and GaSb, total growth time for one period of 8/8 T2SL is 54 seconds from which 12s is for $Sb_2$ soak while 2s is for growth interruption. For LWIR T2SL, soak times and growth interruption time would increase dramatically for strain compensation and this would lead to increased growth times. Increased growth interruption time might deteriorate the quality of T2SL by encouraging incorporation of impurities during growth. As can be seen from Fig. 4.1(c), structure (E) has PL intensity to structure (D), and at the same time it requires smaller growth time as compared to structure (D), as summarized in Table 4.1.

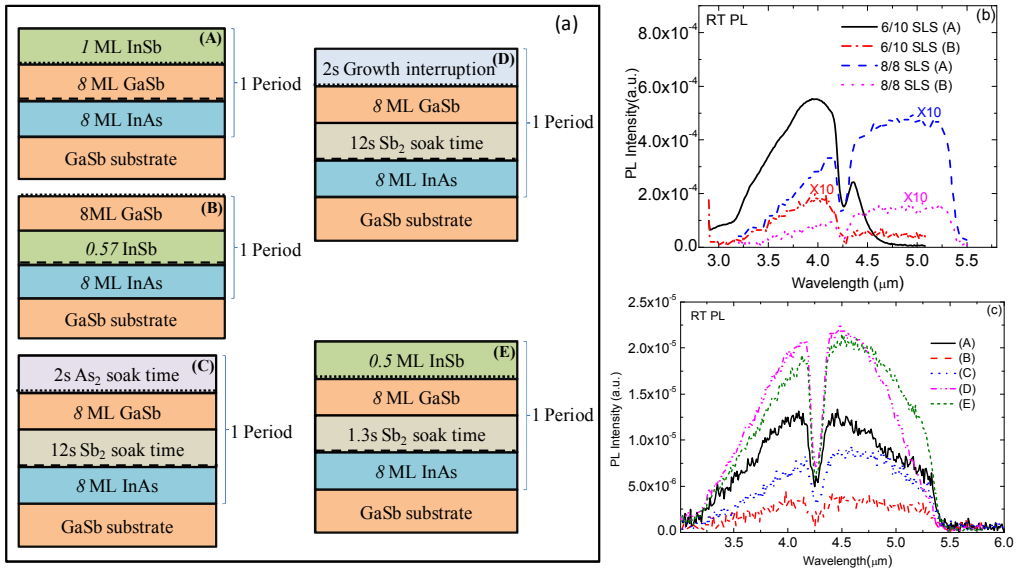


Fig. 4.1. (a) Different interface types studied for 8/8 MWIR detector performance comparison, where dotted and dashed lines represent tensile and compressive interfaces, respectively, (b) RTPL comparison of 6/10 T2SL and 8/8 T2SL with interfaces (A) and (B), (c) RTPL comparison of 8/8 T2SL structure grown back to back with all five interfaces.

| Structure | Tensile interface | Compressive interface | Growth time (One period) (s) | Integrated RTPL intensity (a.u.) (Normalized) |
|---|---|---|---|---|
| (A) | InSb growth | Uncontrolled | 42 s | 3.3 |
| (B) | Uncontrolled | InSb growth | 41s | 1 |
| (C) | $As_2$ soak time | $Sb_2$ soak time | 54s | 2.2 |
| (D) | Growth interruption | $Sb_2$ soak time | 54s | 5.1 |
| (E) | InSb growth | $Sb_2$ soak time | 42s | 5.2 |

Table 4.1. Summary of interface samples with their respective one period growth time, using growth rates of 0.4ML/s for both Ga and In, and normalized integrated RTPL intensity.

On the basis of material characterization, interface schemes (A), (D) and (E) have the highest intensity PL intensity at room temperature. In order to study the impact of interfaces on infrared detector performance, three homojunction PIN detectors with structure (A), (D) and (E) were grown. All three detectors consist of 150 periods thick 8/8 T2SL Te doped N contact layer ($n = 3\times10^{18}$ $cm^{-3}$), followed by 40 periods thick graded n-doping region. This is followed by a 200 periods thick non-intentionally doped (n.i.d) 8/8 T2SL absorber region, followed by p-type graded doping region, 40 periods, of 8/8 T2SL. The topmost layer is 50nm thick Be doped GaSb P contact layer ($p = 2.8\times10^{18}$ $cm^{-3}$). The detector material was first characterized using PL. Fig. 4.2 compares variable temperature integrated PL data. It reflects that at low temperatures, structure (D) has highest PL intensity while structure (A) has the lowest. However, at higher temperatures, PL intensity of structure (E) becomes comparable to that of structure (D). This possibly indicates that the non-radiative recombination time in these two structures becomes comparable at higher temperatures, while scheme (A) has the shortest recombination time.

The material was processed into single pixel 410x410 $\mu m^2$ mesa area arrays with circular apertures ranging from 25μm diameter to 300μm using inductively coupled plasma (ICP) dry etching followed by deposition of Ti/Pt/Au to make ohmic contacts. The normalized spectral response data for three detectors has been shown in Fig. 4.3(a) at 77K, at a reverse bias voltage of 50mV. The 50% cutoff wavelength ($\lambda_c$) for structures (A), (D) and (E) is 4.2μm, 3.8μm and 4.1μm, respectively. Structure (A) has InSb layer for strain compensation which results in higher cutoff wavelength, while structure (D) totally relies

on soak time and growth interruption to achieve strain compensation and hence has the smallest $\lambda_c$.

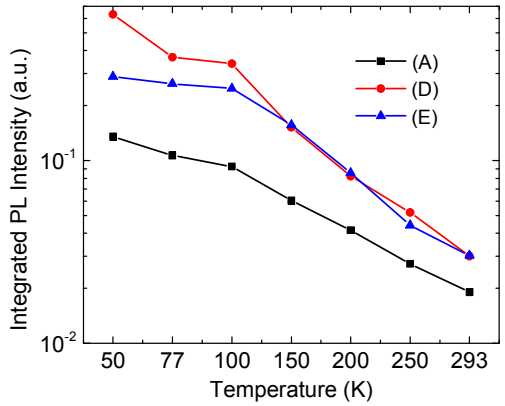


Fig. 4.2. Variable temperature integrated PL intensity comparison of structures (A), (D) and (E).

Fig. 4.3(b) shows dark current densities for structures (A), (D) and (E) at 77K as a function of applied bias. Structures (A), (D) and (E) have dark current densities of $2\times10^{-3}$ A/cm$^2$, $8.8\times10^{-4}$ A/cm$^2$ and $8\times10^{-4}$ A/cm$^2$, respectively, at 20mV of reverse bias. This suggested that the highest dark current density was observed for interface (A). Radiometric characterization of these detectors was carried out using a calibrated blackbody source at 900K, and a 2.5μm long pass filter (LPF). Measured peak quantum efficiency (QE) and detectivity, as a function of temperature, have been shown in Fig. 4.4. It is to be noted that the noise measurements for detectivity were carried out with 2π field of view (FOV) and 300K background. It can be seen that the responsivity is highest for structure (A), but very close to that of structure (E), and is the least for structure (D). Measured detectivity is maximum for structure (D) at 77K and 100K, however it becomes comparable to that of structure (E) at higher temperature (above 150K), while

structure (A) has the least detectivity at all the temperatures. The lowest detectivity in structure (A), in spite of high responsivity, is due to higher noise compared to structures (D) and (E). We attribute this to increased interface scattering with respect to other structures which leads to high nonradiative recombination rate or small nonradiative lifetime. This corroborates well with PL data, shown in Fig. 4.2, where structure (A) had the least integrated PL intensity of all the samples while the intensity of structure (E) was comparable to that of structure (D) at higher temperatures. Structure (E) has higher and comparable detectivity than structure (A) and (D), respectively. It also has higher responsivity than structure (D). Peak responsivity and detectivity of structure (E) at 77K, at reverse bias of 20mV, is 3A/W and $4.3\times10^{10}$ cm-$Hz^{1/2}W^{-1}$, respectively, for $2\pi$ field of view, 300K background. Peak responsivity and detectivity at 200K are 2.2A/W and $6.7\times10^{8}$ cm-$Hz^{1/2}W^{-1}$, respectively. Detector characterization shows that promoting InSb type bonds at both the interfaces of T2SL improves the optical quality of material and signal to noise ratio at high operating temperatures as compared to structures with one uncontrolled interface. Use of InSb layer at tensile interface and use of $Sb_2$ soak time at compressive interface is optimal in terms of material optical quality, device performance and growth time.

## 4.2 Polarization Selective Photocurrent Spectroscopy

This section gives experimental and theoretical details of the polarization dependent interband transitions in T2SL detectors. In this wok, experimental and theoretical results have been correlated to establish ordering of minibands in valence band of InAs/GaSb T2SL detectors.

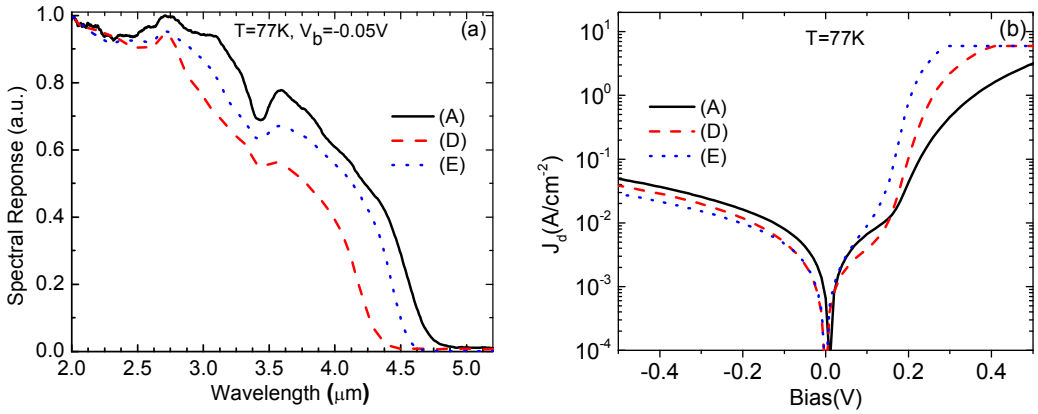


Fig. 4.3 Comparison of (a) normalized spectral response of three detector structures at -0.05V, (b) dark current densities of structures (A), (D) and (E) at 77K.

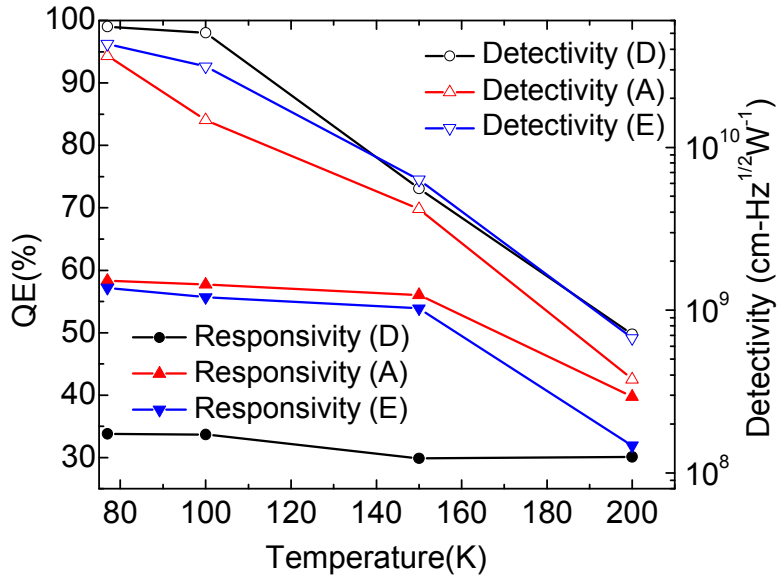


Fig. 4.4. Temperature dependent measured peak QE and detectivity comparison of three detectors at 2π FOV and 300K background.

### 4.2.1 Experimental Details

To carry out polarization dependent interband transition study, photocurrent measurements were preferred over absorption measurements because of poor signal to noise ratio in latter. The photocurrent measurements are performed on a processed single pixel detector. After MBE growth, material was processed into detector arrays, and then a

small piece, 5mm by 5mm, was cleaved which had multiple single pixel devices with optical apertures ranging from 25μm to 300μm diameter. The sample was then mounted on a polishing holder to polish one of the edges at 45º facet. Polishing was carried out manually, starting with 30μm polishing pad and ending with a 1μm pad. Once the edge was polished, the sample was mounted on at 45º holder which was then mounted on a chip carrier with a hole to couple light to the edge. The photograph of the sample mounted on the chip carrier as well as inside the LN2 cooled dewar has been shown in Fig. 4.5(a), while Fig. 4.5(b) shows the schematic of the prepared sample and different polarization of incident beam with respect to the sample. Polarization of light in the plane of the superlattice (*x*-*y* plane) is TE, while that along the growth direction (*z*-axis) is TM polarization.

The schematic of the measurement setup has been shown in Fig. 4.6. The device is mounted inside a cryostat, cooled with liquid nitrogen. The glowbar source of Fourier Transform Infrared (FTIR) Spectrometer is used as the excitation source for the measurements. The beam passes through a KRS5 polarizer for polarization selection. It is to be noted that the sample is mounted inside the cryostat such that the polished edge is normal to the incident light. A bias voltage is applied across the device using a current preamplifier. Once beam falls on the device, electron-hole pairs are generated leading to the photocurrent. The polarizer can be used to select either ***s*** or ***p*** polarized light, as shown in Fig. 4.5 (b), and hence photocurrent can be measured for these two polarizations. Once, photocurrent has been measured for ***s*** and ***p*** polarized beams, it is resolved into TE and TM component using the following math[83]. If $R_p$ and $R_s$ are the photocurrents for ***p*** and ***s*** polarized beams, respectively, then the photocurrent due to TE

polarization is same as $R_s$. The photocurrent for TM polarization can be obtained by using equation (4.1).

$$\frac{\mathrm{TE}}{\mathrm{TM}} = \frac{1}{\left[2\times\left(\frac{R_p}{R_s}\right)-1\right]} \tag{4.1}$$

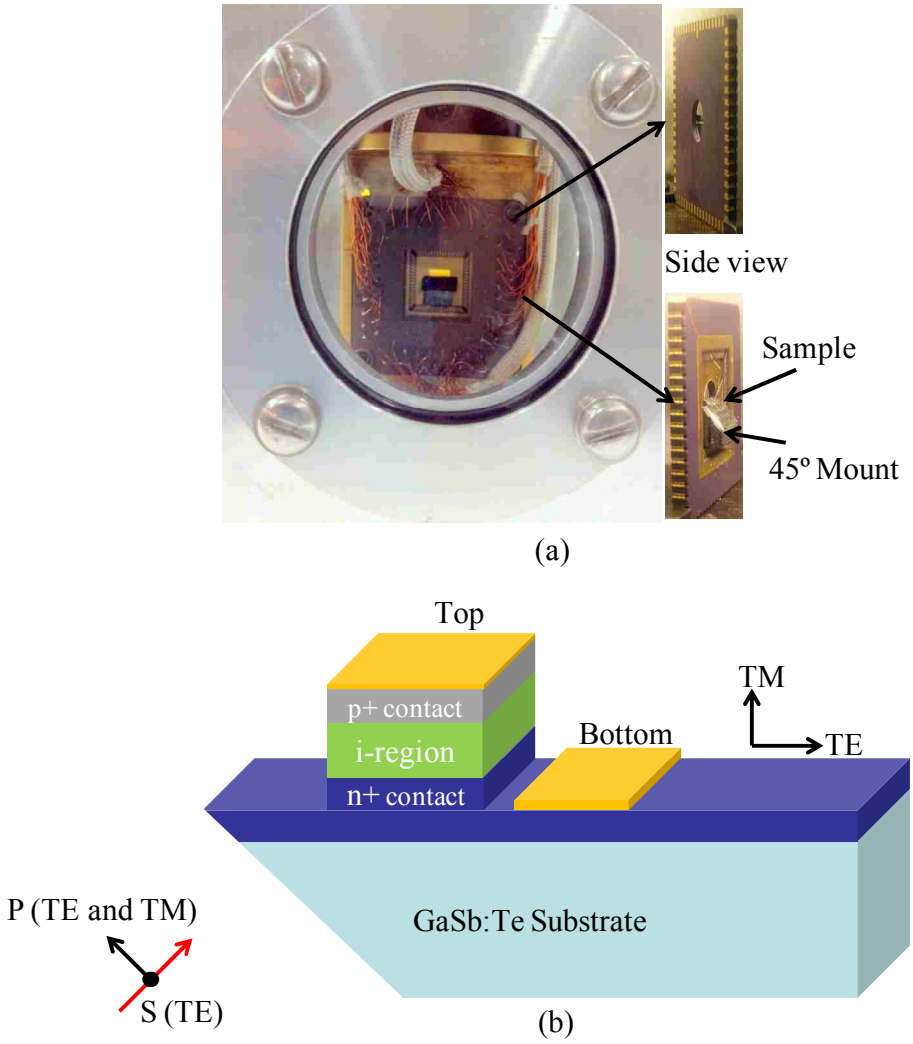


Fig. 4.5. (a) Picture of device mounted inside the cryostat for measurements at 77K and a zoomed in image of the device mounted in the chip carrier at 45° angle, (b) Schematic of the structure of device under test and the orientation of electric field with respect to the device. TE polarization is the polarization of light in plane of T2SL while TM is in the growth direction.

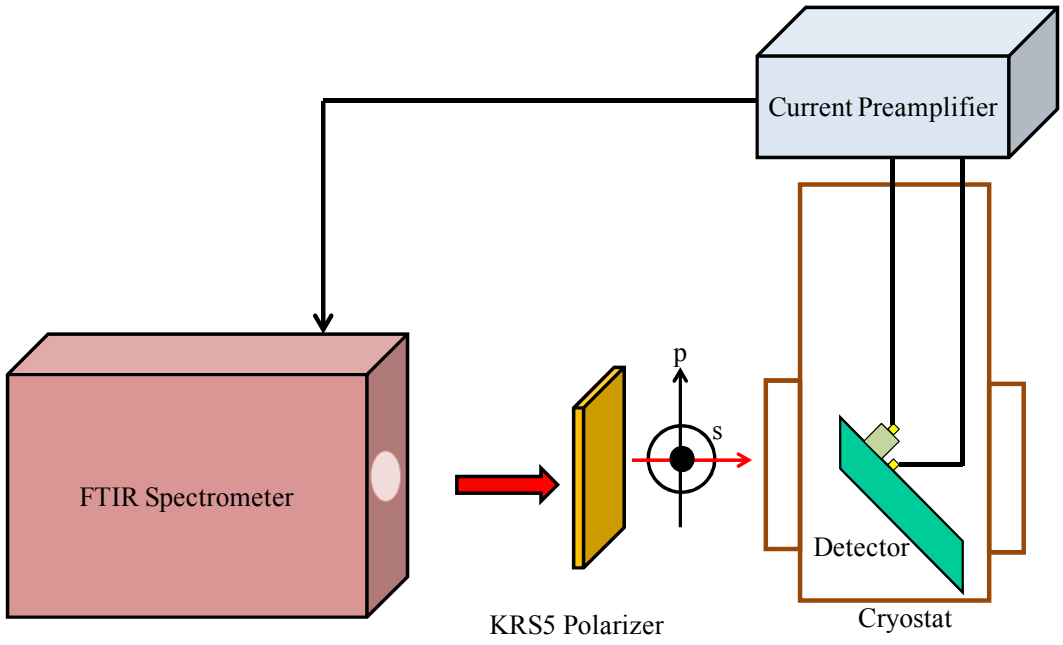


Fig. 4.6. Schematic illustration of experimental setup for polarization sensitive photocurrent measurements, showing the FTIR, polarizer, cryostat with T2SL detector mounted inside it and the current preamplifier.

Photocurrent measurements were carried out on homojunction MWIR, and LWIR T2SL detectors. The schematic of the MWIR detector structure, with thicknesses of various regions, is shown in Fig. 4.7 (a). In this structure, 10ML InAs/10ML GaSb T2SL has been used for N-contact layer, absorber region and P-contact layer. The structure also has graded n- and p- region between the bottom contact layer and absorber region and absorber and top contact layer, respectively. The unpolarized photocurrent measurements were carried out without the polarizer in the beam path, which shown in Fig. 4.7 (b). The unpolarized photocurrent spectrum shows a cutoff wavelength of 5.8μm, at 77K and a reverse bias of 50mV. The polarized photocurrent for TE and TM polarized light has been shown in Fig. 4.7(c). From the polarized photocurrent spectrum shown in Fig. 2(c), we make three key observations: (1) The TE photocurrent is higher than the TM photocurrent for all the wavelengths; (2) The TM absorption vanishes near the band-edge

before the TE absorption, and (3) There is a pronounced dip in the TM photocurrent at 3.7μm (0.335eV), away from the band-edge of the T2SL. Latter two features are indicated by circle and arrow, respectively, in Fig. 4.7(c) and a zoomed-in image of the band edge photocurrent is also shown in the inset.

The schematic of LWIR T2SL detector is shown in Fig. 4.7(d), which is made of 14 ML InAs/7ML GaSb T2SL. The relative positions of minibands can be significantly different between MWIR and LWIR T2SL. The LWIR absorber has a cutoff wavelength of 11.5μm, at 77K, at a reverse bias of 50mV. Interestingly, the polarization sensitive photocurrent spectrum also shows the same three features observed in the MWIR T2SL: a dominant TE polarized absorption, zero TM response at the bandedge and a dip in TM polarized light at 5μm, beyond which the signal increases monotonically for lower wavelengths.

In order to understand the nature of the participating transitions, a detailed theoretical modeling of the T2SL was undertaken to calculate bandstructure, wavefunction, momentum matrix element and oscillator strength, using empirical pseudopotential method[37]. The details of the EPM method to find E-k relationships and wavefunctions have been elaborated in chapter 3. Then using Fermi's golden rule and k-selection rule [84], the momentum matrix element $p_{if}$ was obtained using equation (4.2), which has also been described in chapter 3.

$$p_{if} = \frac{1}{Vol} \int \Psi^{*}_{\mathrm{k,\acute{l}}} (\hat{\mathrm{a}} \cdot \vec{\mathrm{p}}) \Psi_{\mathrm{k,l}} \, d^3 r \qquad (4.2)$$

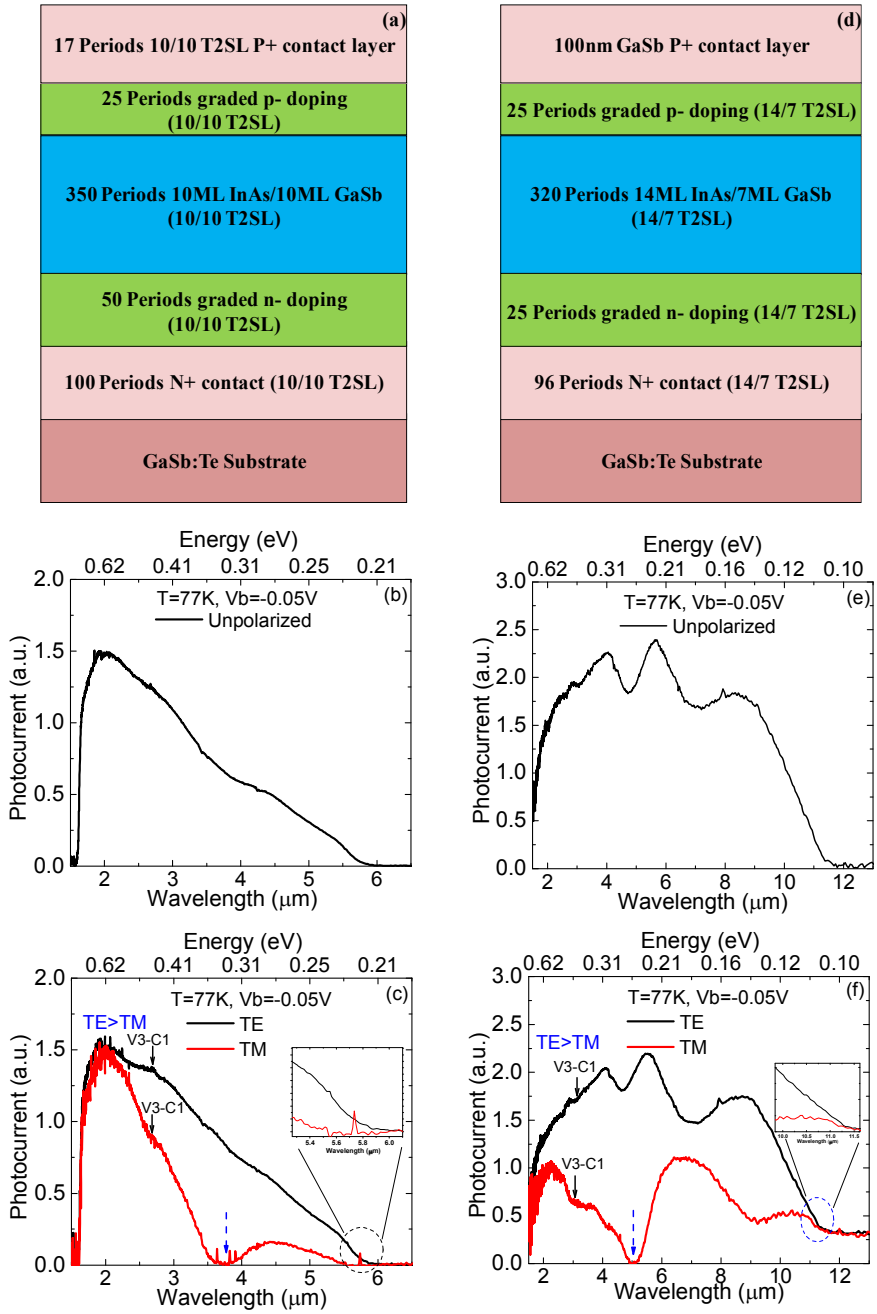


Fig. 4.7. Heterostructure schematic, unpolarized, transverse electric (TE), transverse magnetic (TM) photocurrent spectra for a mid wave infrared (MWIR) and long wave infrared (LWIR) in the first and second column, respectively.

where $\Psi^*_{k,\hat{l}}$ is the complex conjugate of the final conduction miniband state, $\Psi_{k,l}$ is the wavefunction of the initial valence miniband state, $\hat{a}$ is the unit vector in the direction of

electromagnetic field, $\vec{p}$ is the momentum operator, $Vol$ is the volume of the space and $\mathbf{k}$ denotes electron wave-vector. The oscillator strength in energy units is given by the expression $2\left|p_{if}\right|^2/m_0$, where $m_0$ is the mass of an electron. Fig. 4.8(a) and (b) show the calculated bandstructure and energy dispersion relationship for MWIR and LWIR T2SL, respectively, for wave-vector in the plane of T2SL ($k_{xy}$) as well as in the growth direction ($k_z$). Zero on the energy scale denotes conduction band energy of InAs at Γ point. As can be seen, bands are much more dispersive in the plane of the T2SL as compared to the growth direction, which is consistent with other simulation methods , such as, eight band k·p[74]. It is also to be noted that the width of the miniband is determined by the dispersion along $k_z$ direction.

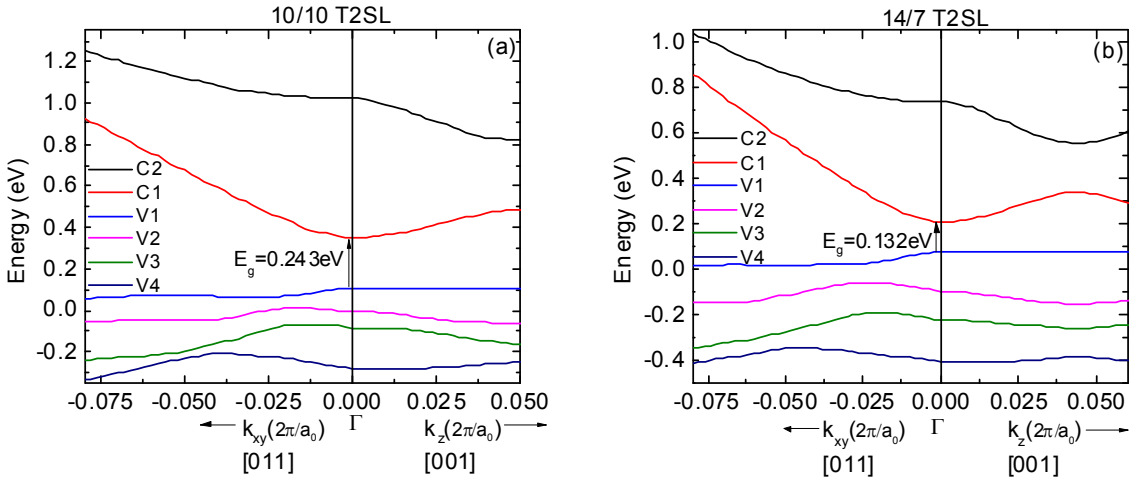


Fig. 4.8 Calculated bandstructure of T2SL showing dispersion of energy with respect to electron wavevector in plane ($k_{xy}$) and in the growth direction ($k_z$) for (a) MWIR T2SL and (b) LWIR T2SL. The conduction band states are labeled as C1 and C2, whereas the valence band states are labeled as V1-V4.

The oscillator strength, calculated for different transitions is shown in Fig. 4.9(a) and (b) for MWIR and LWIR T2SL, respectively. Please note that oscillator strength multiplied with density of states gives absorption coefficient[85]. We first discuss the simulation

results and compare them with the experimental observations for the MWIR T2SL. It is known that for heavy hole transitions, the TE polarization absorption is orders of magnitude stronger than the TM polarization absorption, while, for light hole transitions, the TM polarization absorption is much stronger than the TE polarization absorption[84, 86]. Fig. 4.9(a) indicates that the oscillator strength from V1 to C1 transition is higher for the TE polarization compared to the TM polarization, hence V1 is a heavy hole (HH1), while V2-C1 transition oscillator strength suggests that V2 is a light hole (LH1) band. Following this approach, Fig. 4.9(a) suggests that V3 is a light hole band (LH2), while V4 is a heavy hole band (HH2). Similarly, following the theoretical simulations for LWIR T2SL, shown in Fig. 4.9(b), we observe that V1 is HH1, V2 is LH1, V3 is LH2 and V4 is HH2 band.

The theoretical calculations were then compared with the experimental data. In order to verify the valence miniband assignments, we calculated the optical matrix element as a function of wavelength for both T2SLs, shown in Fig. 4.10. It is to be noted that the calculations shown in Fig. 4.10 have been carried out for electron wave-vector in $k_z$ direction. It can be seen that the calculated optical matrix element for HH1 to C1 transition, for both MW and LW T2SL, is much higher for the TE polarization than the TM polarization, and TM polarization absorption is insignificant at bandegde. This compares well with experimental data shown in Fig. 4.7(c) and (f). The transition from V2-C1 starts at an energy of 0.35eV and 0.27eV for MW and LW T2SL, respectively, from the theoretical results. These energies are close to the energies at which there is a

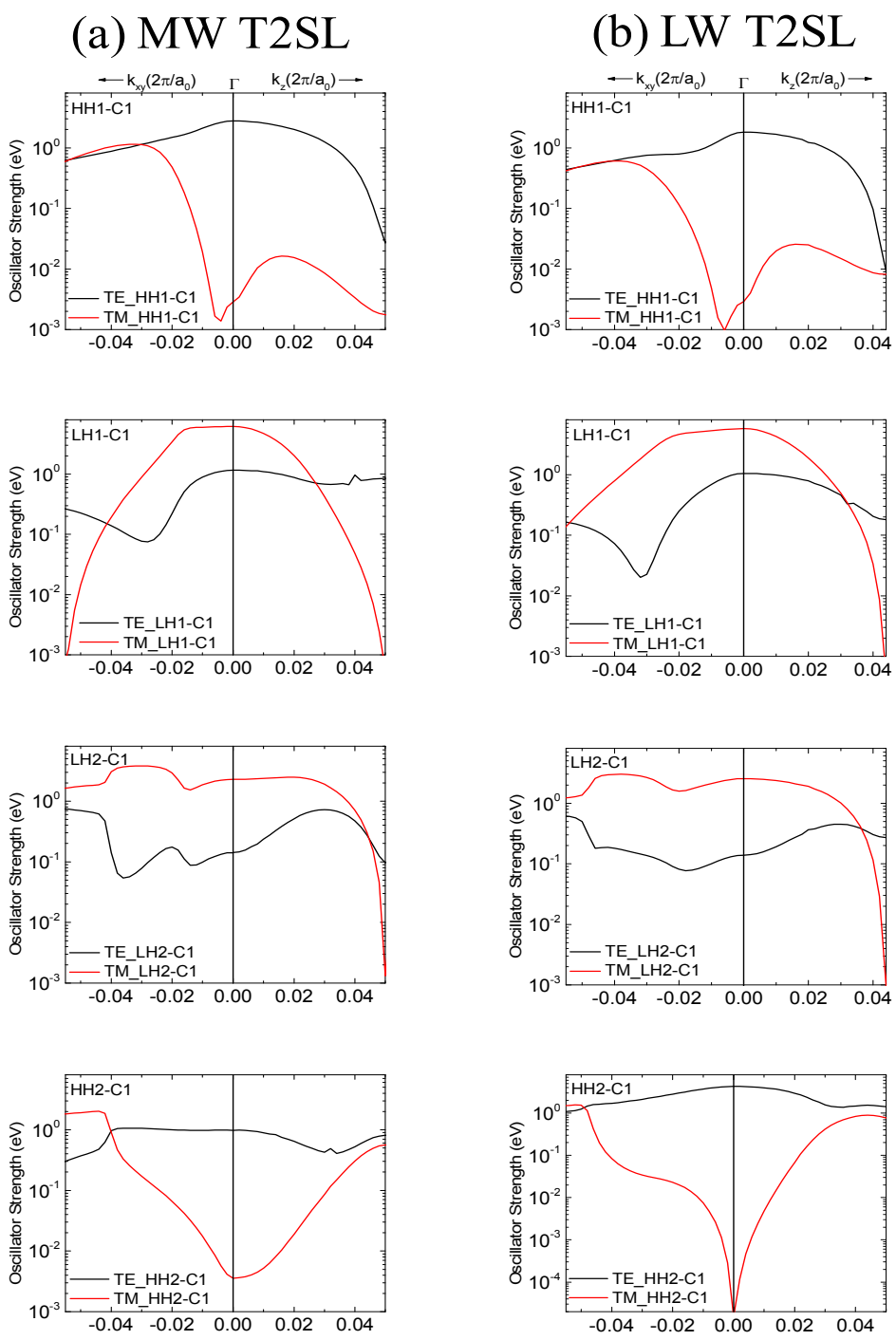


Fig. 4.9. Calculated oscillator strength for various valence minibands to conduction miniband (C1) transitions in the direction of growth ($k_z$) and in plane of T2SL ($k_{xy}$) for (a) MWIR and (b) LWIR T2SL.

dip in TM polarization photocurrent before it increases for higher energies, as shown, in Fig. 4.7(c) and (f). The increase in TM photocurrent with increase in energy after the prominent dip indicates that V2 band is a light-hole band, LH1, and the dip is indicative of the onset of LH1-C1 transition and can also provide an estimate for the width of the C1-HH1 transition. Theoretically, LH2-C1 transition starts at 0.46eV and 0.43eV, respectively, for MW and LW devices. These transitions are marked in Fig. 4.7(c) and (f), which also show that the TM photocurrent increases for energies higher than the absorption edge and hence suggesting their light-hole nature. The nature of third valence miniband is established as LH2, both theoretically and experimentally. Fig. 4.10 shows that the onset of HH2-C1 transition occurs at 0.62eV and 0.61eV for MW and LW devices, respectively, which is very close to the GaSb absorption edge and hence, in Fig. Fig. 4.7(c) and (f), the reduction in TM photocurrent at these energies is not obvious. The summary of miniband transition has been shown in Table 4.2 as well, for MW and LW T2SLs.

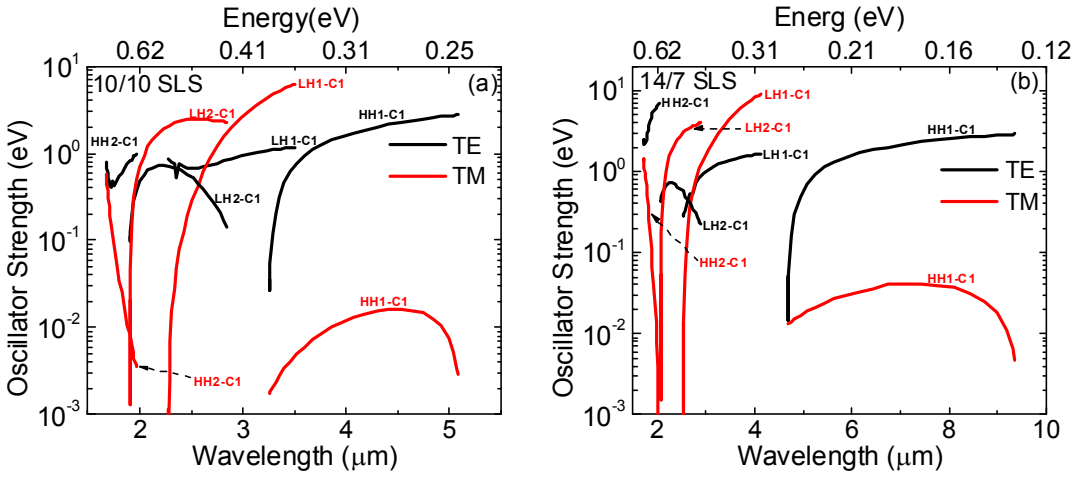


Fig. 4.10. Calculated oscillator strength as a function of wavelength (energy), showing absorption edges of different transitions for (a) MWIR and (b) LWIR T2SL. The dip in the TM photocurrent indicates the onset of C1-LH1 transition.

| Miniband Transitions | Transition Energies (eV) | | | |
|---|---|---|---|---|
| | Theoretically | | Experimentally | |
| | MW | LW | MW | LW |
| HH1-C1 | 0.24409 | 0.13248 | 0.21088 | 0.10877 |
| LH1-C1 | 0.35429 | 0.29736 | 0.33514 | 0.25306 |
| LH2-C1 | 0.43509 | 0.42907 | 0.45926 | 0.40129 |
| HH2-C1 | 0.62626 | 0.61084 | Hard to see as close to GaSb absorption edge (0.77eV) | Hard to see as close to GaSb absorption edge (0.77eV) |

Table 4.2. Theoretically and experimentally observed transition energies in MW(10/10) and LW(14/7) T2SL detectors.

In conclusion, it has been shown that the material quality of T2SL detectors can be improved significantly by using an optimal scheme for controlling the interfaces. It has been found that the use of Sb-soak time on compressive interface and an interfacial InSb layer on the tensile interface improves optical quality of the material and also leads to a significant improvement in detector performance.

Physical understanding of the T2SL system has been improved using polarization sensitive photocurrent spectroscopy. These measurements on InAs/GaSb T2SL superlattice detectors have led to the identification and ordering of quantum confined valence minibands for both MWIR and LWIR material systems. It has been established in this work, that ordering of the valence minibands is heavy-hole (HH1), light-hole (LH1), light-hole (LH2) and heavy-hole (HH2), with increasing energy, for both MWIR and LWIR T2SL. These findings are strongly supported by the theoretical simulations based on the empirical pseudopotential theory.

# 5 Barrier Engineered Photodiodes for Single and Multicolor Detection

Early work in LWIR T2SL detectors started with homojunction PIN devices. Such designs result in higher dark current levels and are not suitable for FPA fabrication. This has led to the realization of heterojunction T2SL photodiodes, which use unipolar barriers to reduce dark current [21-23, 87]. Such heterojunction designs are possible because of the bandgap and band-offset tunability offered by the 6.1Å family[18], where a desired T2SL can be formed by a combination of (InAs, GaSb, AlSb) compounds and by changing the thicknesses of constituting layers of T2SL. The advantage of unipolar barrier photodiodes is to improve performance by reducing one or several components of dark currents, while maintaining similar photocurrent as in PIN photodiodes. High performance barrier devices have resulted in large format LWIR T2SL FPA[24, 88].

Also, there has been a demand for high operating temperature (HOT) MWIR detectors. Operation at high temperature reduces cost of cryogenic cooling significantly, leading to a reduction in size and total cost of the detector system. Recently, FPAs based on T2SL have demonstrated operation up to 170K[89], challenging the established MWIR InSb technology. Another technology which has shown tremendous development with HOT FPAs is InAsSb, which recently demonstrated imaging up to 180K[90]. InAsSb technology is emerging as a contender for T2SL based HOT MWIR photodiodes. $InAs_{0.91}Sb_{0.09}$ lattice matched to GaSb is grown on GaSb substrate. The system cannot be used for the design of advanced detectors meant for multi-color detection. On the other hand, T2SL system gives the flexibility of changing the cutoff wavelength by change in

the composition of layers and strain compensation helps with the growth of thick detector structures.

Infrared detectors with multiband detection capabilities are important for highly demanding applications in target identification, recognition and tracking. Multicolor detectors can also be used to determine the absolute temperature of targets, which is very useful in medical diagnostics and astronomy. Dual band detectors have already been realized in commercially available technologies such as Mercury-Cadmium-Telluride (MCT)[91] system, and Quantum Well Infrared Photodetectors (QWIPs)[92]. Multicolor detectors usually have one or more spectrally selective bands in the short wave infrared (2-3μm), mid wave infrared (3-5μm) or long wave infrared (8-12μm) regions. For example, a dual color MWIR type-II InAs/GaSb T2SL FPA has been successfully demonstrated by Rehm *et al.*[93]. Bias tunable dual band MWIR/LWIR detector [94] have been reported earlier by our group, while n-i-p-p-i-n three contact dual-band MWIR/LWIR detectors[95] have been realized by Delaunay *et al.* at Northwestern University (NWU). Recently, a LWIR dual band T2SL FPA has been reported by NWU[96].

## 5.1 Barrier Device Realization on T2SL System

T2SL heterojunction barrier diodes have evolved from simple designs, where PIN homojunction is modified such that *p*-contact is replaced by GaSb contact layer which is also an electron barrier layer[97]. In this text we call barriers used for blocking electrons and holes as electron barrier (EB) and hole barrier (HB). One of the earlier heterojunction design was conceptualized by Johnson *et al.*[98], where EB and HB layers are made of *p*-type and *n*-type GaSb, respectively. Double heterojunction (DH) photodiode design

reported by Vurgaftman *et al.*[99] is based on W-structured T2SL(WSL)[20], where the wide bandgap contact layers act as barriers. Another DH design, reported by Delaunay *et al.*[100], was shown to reduce the surface leakage current. Other advanced heterojunction photodiode architectures that rely on unipolar barriers to reduce dark current are p-π-M-n [21], p-M-p[101], CBIRD[22], HSL[102], pBn[103], ALSL-B photodiode[87] and pBiBn[23].

The bandgap of InAs/Ga(In)Sb T2SL, for example, can be changed by just changing the thicknesses of constituting layers or by changing the composition of ternary compounds. The band-offset tunability is crucial for realization of barrier devices. Barrier layers are selected such that the HB layer offers unimpeded flow of electrons while blocking holes and the EB layer blocks off electrons while allowing unimpeded flow of holes. Hence, one requires EB and HB layers to have zero valence band-offset (VBO) and conduction band-offset (CBO) with respect to the absorber layer, respectively. One example, for the purpose of illustration, is to design EB layer with GaSb/AlSb superlattice, HB layer with InAs/AlSb T2SL for an absorber layer designed with InAs/GaSb T2SL. EB and HB layers can also be designed with similar T2SL system as the absorber region, by changing the composition of T2SL.

In this work, heterojunction unipolar barrier architecture, pBiBn, was developed for MWIR and LWIR detection. The design approach, growth aspects, and detector characterization have been discussed in this chapter. A dual band MWIR/LWIR, and a three band SWIR/MWIR/LWIR detectors, using unipolar barriers, are demonstrated as well. The design and growth complexities of multi-band detectors have also been discussed along with characterization results.

## 5.2 Designs

The major dark current components in T2SL detectors are diffusion current, Shockley-Read-Hall (SRH) current, tunneling current and surface leakage current. While a number of surface treatments have been tried by different groups, a review of which is given in reference [42], the research in reducing bulk dark currents has been focused on barrier engineering. With suitable barrier incorporation, all the components of bulk dark currents can be reduced significantly. This has led to the realization of heterojunction detectors such as nBn[49], W-structure[20], CBIRD[22], pBiBn[23] and M-structure[21].

In order to reduce the dark current in T2SL detectors, it is important to understand the origin of dark current mechanisms. The simulation of dark current T2SL detectors has been reported in the literature [63, 104-107], but it is not straightforward as a lot of the physical properties of T2SL are not known very well. The major dark current components have been given below.

**Diffusion current**

Diffusion dark current is present at any semiconductor junction, and it contributes to both forward and reverse bias. The expression for diffusion current is given by the following equation[63].

$$J_{diff} = n_i^2(T)\sqrt{qk_BT}\left(\frac{1}{N_A}\sqrt{\frac{\mu_e}{\tau_e}} + \frac{1}{N_D}\sqrt{\frac{\mu_h}{\tau_h}}\right)(\exp(qV/k_BT) - 1) \quad (5.1)$$

where $n_i(T)$ is the intrinsic carrier concentration, $q$ is the electronic charge, $T$ is temperature, $k_B$ is the Boltzmann's constant, $N_A$ and $N_D$ are acceptor and donor

densities, respectively. $\mu_e$, $\tau_e$, and $\mu_h$, $\tau_h$ are mobility and lifetime for electrons and holes, respectively, and $V$ is the applied bias.

**Generation-Recombination or SRH current**

Generation-recombination (GR) current originates from the defect and trap states which sit in the forbidden gap of the semiconductor. These states can act as a generation or recombination site. SRH current also contributes in both the bias regimes. The expression for it is given by the following equation [29, 108].

$$J_{SRH} = \frac{qn_iW}{\tau_{SRH}} \frac{2k_BT}{q(V_{bi}-V)} \sinh\left(\frac{qV}{2k_BT}\right) f(b) \tag{5.2}$$

$$f(b) = \int_0^\infty \frac{1}{u^2+2bu+1} du\,, \quad b = \exp\left(-\frac{qV}{2k_BT}\right) \cosh\left(\frac{E_t-E_i}{kT}\right) \tag{5.3}$$

where $W$ is depletion width, $\tau_{SRH}$ is the generation-recombination lifetime, $V_{bi}$ is the built-in voltage, $E_i$ is the intrinsic Fermi level and $E_t$ is the trap energy level.

**Trap-assisted tunneling (TAT)**

Trap assisted tunneling current is important at high electric fields, and commonly experienced in high reverse bias. This occurs in or near the depletion region when minority carrier gets into the trap state from valence band and then into the conduction band. The expression for trap-assisted tunneling is given by the following equation[107].

$$J_{\text{TAT}} = \frac{q^2 m_T V M^2 N_t}{8\pi h^3 (E_g-E_t)} \exp\left(-\frac{4\sqrt{2m_T(E_g-E_t)^3}}{3q\hbar F(V)}\right) \tag{5.4}$$

where $m_T$ is the reduced tunneling effective mass, $E_g$ is the bandgap, $N_t$ is the trap density, $M$ is the transition matrix element associated with the trap, $F$ is the electric field.

**Band-to-band tunneling (BTB)**

BTB current results from tunneling of carriers from valence band into the conduction band. Similar to TAT, BTB is dominant at high electric field, thus contributes in reverse bias. The expression for BTB current is given by the following equation [63, 106].

$$J_{\mathrm{BTB}} = \frac{q^3 F(V) V}{4\pi^2 \hbar^2} \sqrt{\frac{2m_T}{E_g}} \exp\left( - \frac{4\sqrt{2m_T E_g^3}}{3q\hbar F(V)} \right) \tag{5.5}$$

To significantly reduce the dark currents, we proposed a detector architecture called pBiBn[23], which demonstrated over two orders of magnitude improvement in dark current over a conventional PIN detector design, for LWIR detection. In this design, a PIN photodiode is modified such that, there are unipolar electron and hole blocking layers sandwiched between the P contact layer and the absorber, and the N contact layer and the absorber, respectively. The EB layer blocks the minority carrier diffusion (electrons) current from P contact layer into the absorber region. Similarly the HB layer blocks minority carrier diffusion (holes) current from the N contact layer into the absorber region. This design facilitates a significant reduction in the electric field drop across the narrow-gap absorber region, resulting in most of the electric field drop across the wider bandgap EB and HB layers. This reduction in electric field leads to a very small depletion region, in the absorber layer, and hence reduction in the SRH current. Furthermore, BTB and TAT currents are also reduced due to significant reduction in field drop across the absorber region. While in case of a PIN design, most of the filed drops

across the narrow-gap absorber region, resulting in higher dark currents due to SRH, TAT, BTB and diffusion processes. A cartoon of pBiBn heterojunction detector has been shown in Fig. 5.1, depicting “p” and “n” contact layers, “i” absorber region, and EB and HB barrier layers.

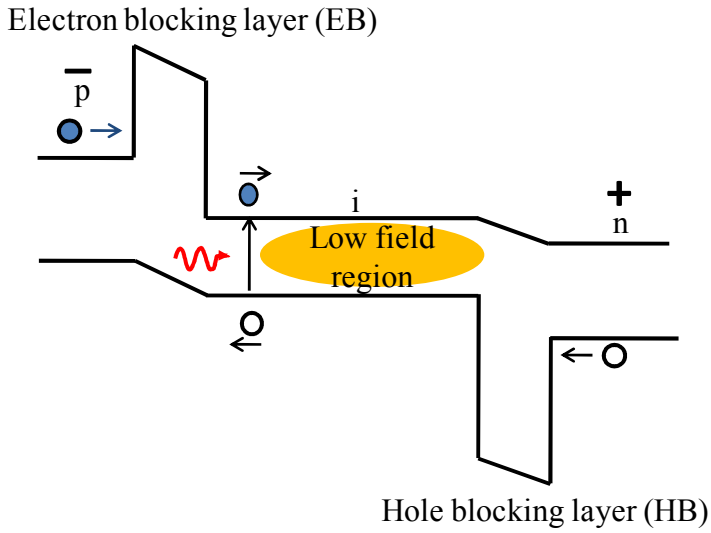


Fig. 5.1. A cartoon representation of pBiBn architecture showing “p” and “n” contact layers, “i” absorber region, and EB and HB electron and hole blocking layers, respectively. It shows operation of device in reverse bias range with EB and Hb layers blocking minority carrier diffusion form contact into the absorber and low field drop across the absorber region. However, there is an unimpeded flow of photogenerated carriers.

The design requirement of a pBiBn photodiode is to select barrier materials for a given absorber such that the HB layer has a zero conduction band offset and the EB layer has a zero valence band offset with respect to the absorber region. The barrier layers are also designed to be made of a wide bandgap T2SL for the purpose of reducing dark current, as mentioned above. To get the desired band alignment for barrier layers, contact layers and absorber region, different T2SLs were simulated using empirical pseudopotential method

[37], described in chapter 3. Once the design was completed, device simulations were carried out in the Sentaurus TCAD[53] simulation platform.

## 5.3 pBiBn LWIR Detectors

In this work, Design 1 of the pBiBn detector was developed, where all the layers were made of InAs/GaSb T2SL. However, this was the very first design and was succeeded by Design 2 which demonstrated performance comparable to the state of the art.

**Design 1**

The detector was grown on Te-doped (001) GaSb substrate. The heterostructure schematic of the detector design design and the X-ray diffraction (XRD) plot obtained using a Philips double crystal X-ray diffractometer has been shown in Fig. 5.2(a) and (b). The full width half maximum (FWHM) or first order satellite peak of the absorber T2SL is 29 arc seconds, which indicates good crystalline quality of the material. It has 637 nm thick N contact layer made of 16ML InAs/ 7ML GaSb doped with Te ($n=3\times10^{18}$ $cm^{-3}$) followed by non-intentionally doped (n.i.d) 450 nm thick hole blocking layer made of 13ML InAs/ 4ML GaSb T2SL. This is followed by a 2.2 μm thick n.i.d absorber region of 14ML InAs/ 7ML GaSb T2SL and an electron blocking layer of n.i.d 325 nm thick 8ML InAs/ 8ML GaSb T2SL. A 138 nm thick 13ML InAs/ 8ML GaSb T2SL P contact layer doped with Be ($p=2.8\times10^{18}$ $cm^{-3}$) completes the structure. The performance of pBiBn detector was compared with a homojunction PIN device. The PIN structure has 609 nm thick Te doped N contact layer ($n = 3\times10^{18}$ $cm^{-3}$) consisting of 14ML InAs/ 7ML GaSb T2SL followed by a 159 nm thick graded n-doping region. This is followed by 2.1 μm thick n.i.d absorber region of 14ML InAs/ 7ML GaSb T2SL, followed by p-type

graded doping region, 159 nm thick, of 14/7 T2SL. The topmost layer is 100nm thick Be doped GaSb P contact layer ($p = 2.8\times10^{18}$ $cm^{-3}$).

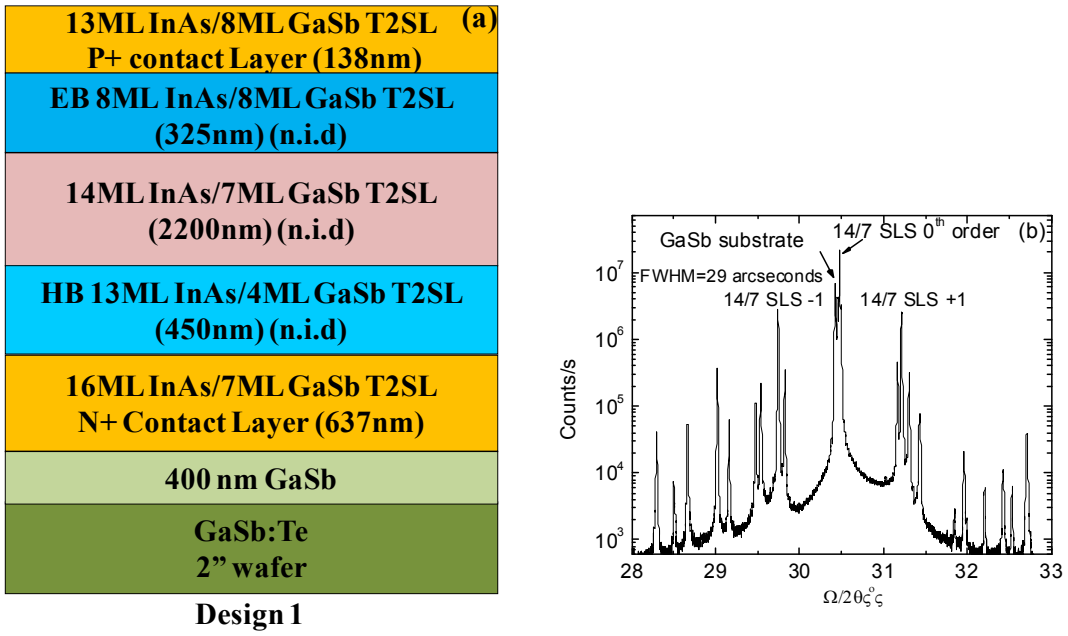


Fig. 5.2. (a) Heterostructure schematic, (b) XRD plot of pBiBn Design 1.

The electric field profile at -250mV of applied bias and band diagram at 77K for no applied bias are shown in Fig. 5.3, where 0eV on energy scale refers to the fermi energy ($E_f$). For the calculation of the electric field, the EB layer has been approximated to have $1\times10^{16}$ $cm^{-3}$ p-type doping while absorber region and HB layers with $8\times10^{15}$ $cm^{-3}$ and $1\times10^{16}$ $cm^{-3}$ n-type doping respectively. The performance improvement of pBiBn over PIN can be explained easily with the help of Fig. 5.3, which shows a significant drop in the electric field across the absorber region of pBiBn design as compared to the PIN design. This in turn leads to the reduction in SRH current, minority carrier diffusion current and tunneling currents.

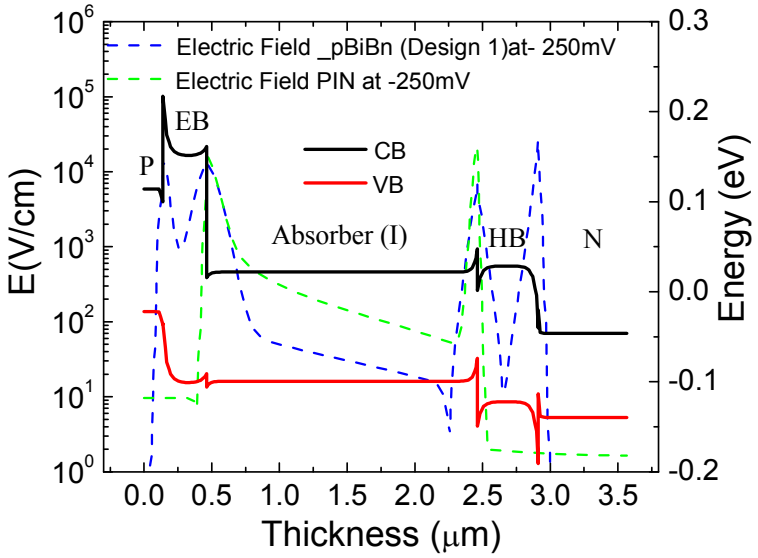


Fig. 5.3. Equivalent energy band diagram of Design 1 and calculated electric field comparison of pBiBn and PIN devices at -250mV

After the MBE growth, the material was processed into single pixel 410×410 μm$^2$ mesa area arrays with circular apertures ranging from 25μm to 300μm in diameter using inductively coupled plasma dry etching. An ohmic contact was made by depositing Ti/Pt/Au on the bottom and the top contact layers of the detectors. The devices were then passivated with SU-8 [43], an epoxy-based negative photoresist, to reduce surface leakage current. Spectral response measurements for these devices were performed at 77K at -0.2V of applied bias. Fig. 5.4(a) shows normalized spectral response of pBiBn and PIN designs with 10.8 μm and 11 μm 50% cutoff wavelengths respectively. The spectral response has been shown for wavelengths higher than or equal to 8.4 μm because all the radiometric measurements reported in this work have been undertaken using a longwave bandpass filter (8.4 – 11.5 μm).

Fig. 5.4(b) compares dark currents of pBiBn design with PIN design at 77K, 90K and 110K. At 77K, pBiBn design has reduced dark current by a factor of 140 over PIN ($V_b$ = -0.25V). However, it is to be noted that the reduction is much more significant at lower bias values with reduction of over three orders of magnitude at -50 mV of applied bias. Temperature dependent Arrhenius plot for PIN and pBiBn devices is shown in Fig. 5.4(c), where natural log of dark current density has been plotted against q/kT, q is electronic charge, k is Boltzmann's constant and T is the temperature. It reveals that dark current in PIN device is dominated by SRH currents above 77K till 175K, above 175K the diode becomes very leaky and resistance of the device becomes comparable to the contact resistance, hence very low value of activation energy is observed at higher temperatures. While for pBiBn device, dark current is SRH limited till 150K, as activation energy correspond to mid-gap states, and above this temperature device is limited by diffusion dark current, activation energy comparable to the bandgap.

The responsivity measurements were carried out at different temperatures using a calibrated black-body source at 900K.

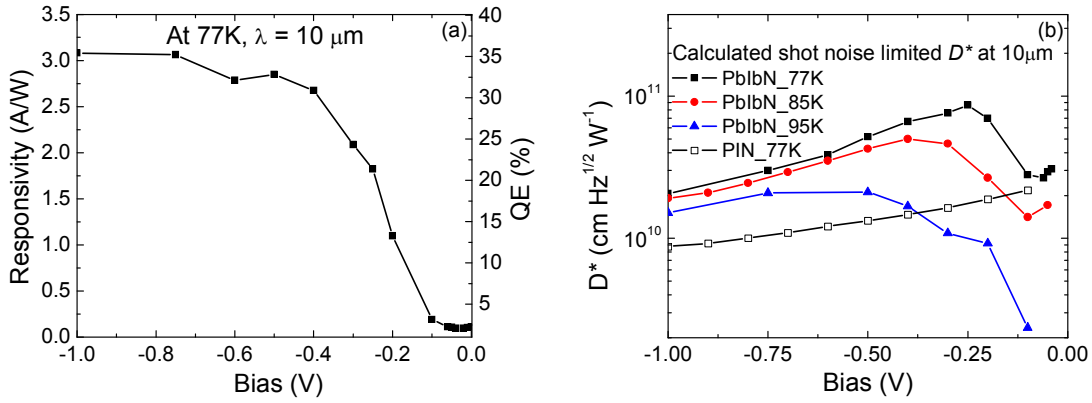


Fig. 5.5(a) the shows measured responsivity and the QE at λ=10 μm at 77K.

Photoconductive gain was assumed to be unity for calculating QE. It is to be noted that no anti-reflection coating (ARC) was used in these devices. The responsivity value at -0.5 V is 2.85 A/W with 35% QE, while at -0.25V bias, responsivity is 1.8 A/W with 23% QE.

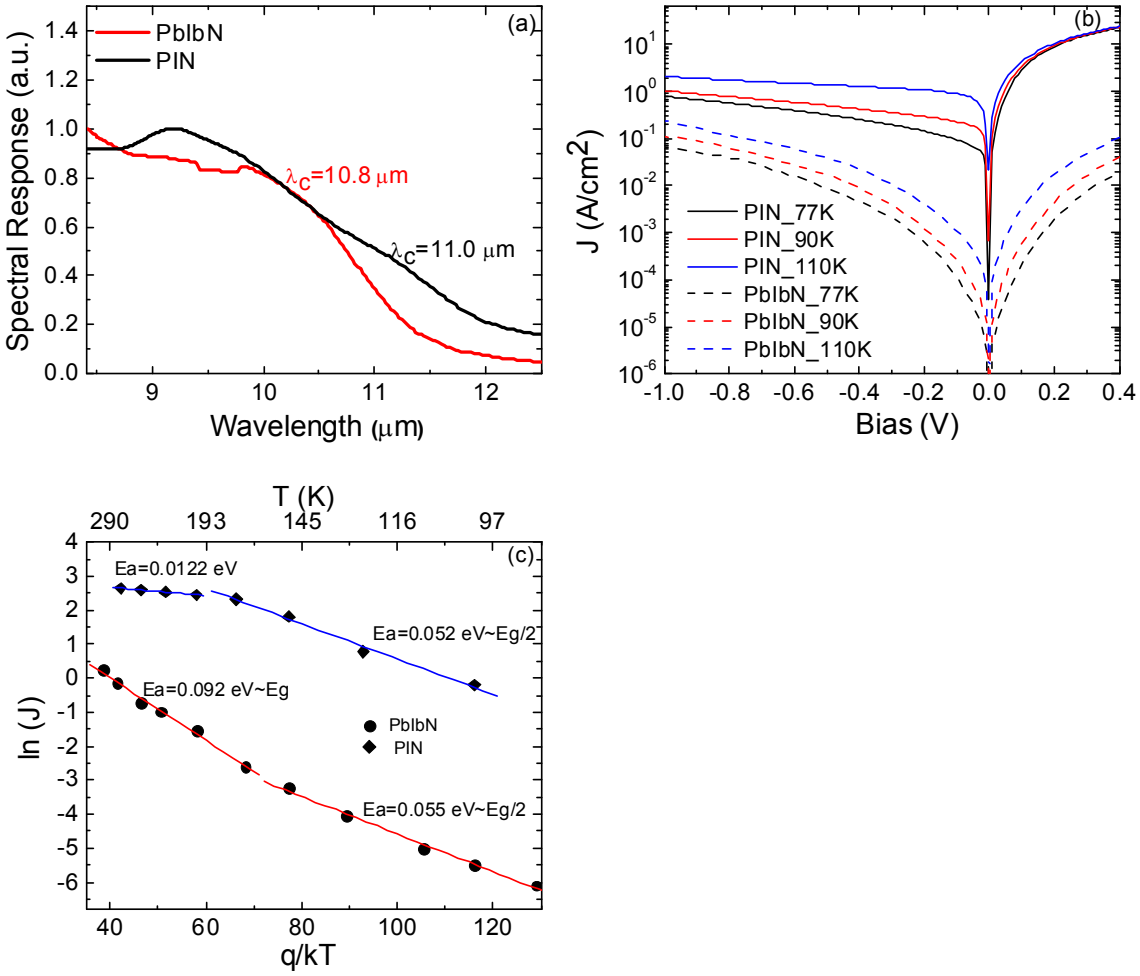


Fig. 5.4. Comparison of (a) spectral response showing 50% cutoff wavelengths, (b) dark current densities at different temperatures and (c) Arrhenius plot of log of dark current density vs. inverse of temperature, for PIN and pBiBn LWIR detectors.

The shot noise and thermal noise limited detectivity ($D^*$) was calculated at 10 μm using the equation (5.6).

$$D^* = R/\sqrt{2qJ_d + (4kT)/R_dA_d} \tag{5.6}$$

where $R$ is the responsivity, $q$ is the electronic charge, $T$ is the temperature of the device, $k$ is Boltzmann's constant, $J_d$ is the dark current density, $R_d$ is the dynamic resistance, and $A_d$ is the diode area.

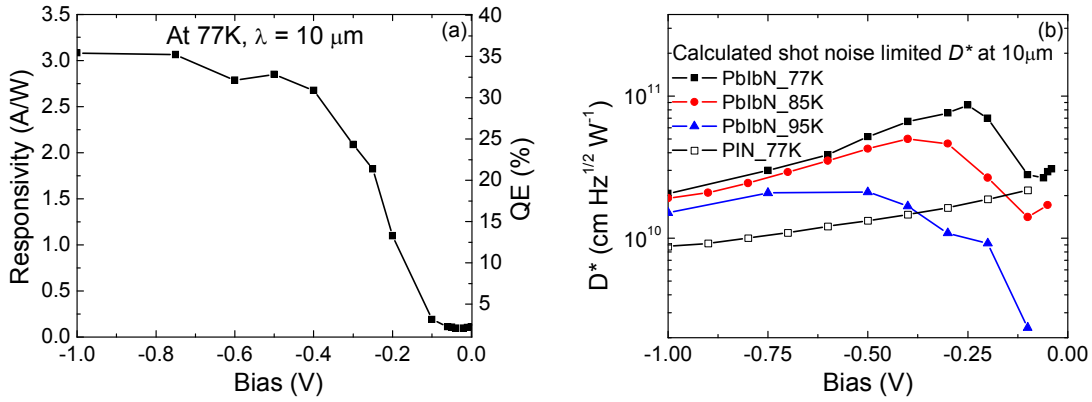


Fig. 5.5(b) shows calculated $D^*$ at various temperatures for pBiBn device and at 77K for PIN device for 10 μm wavelength. At 77K, a peak $D^*$ of $8.7\times10^{10}$ cm $Hz^{1/2}$ $W^{-1}$ is observed at -0.25 V, while at 85K and 95K, the peak $D^*$ is $5\times10^{10}$ cm $Hz^{1/2}$ $W^{-1}$ and $2.1\times10^{10}$ cm $Hz^{1/2}$ $W^{-1}$ at -0.4 V and -0.5V respectively for the pBiBn design. The PIN design has a peak detectivity of $2.2\times10^{10}$ cm $Hz^{1/2}$ $W^{-1}$ at -0.1V of applied bias, which indicates that the pBiBn design improves detectivity by a factor of four over PIN design. Background (300K) photocurrent calculations were carried out using responsivity data (at 10 μm) and blackbody irradiance on the detector under 2π field of view (FOV). Fig. 5.6 demonstrates comparison between photocurrent (PC) density and dark current (DC) densities for pBiBn design. Irradiance due to 300K background, $E_{bkg}$, on a detector for 2π FOV is $6.5\times10^{17}$ photons/s-$cm^2$ for $\lambda_c$ =11μm[1]. The photocurrent density due to 300K background generated in the detector is given by

$$j_{ph,bkg} = QE \times E_{bkg} \times q \tag{5.2}$$

It can be concluded from Fig. 5.6 that the background photocurrent is at least a factor of four higher than the dark current at 100K[17] at -0.25V. Hence, the device is BLIP at 100K.

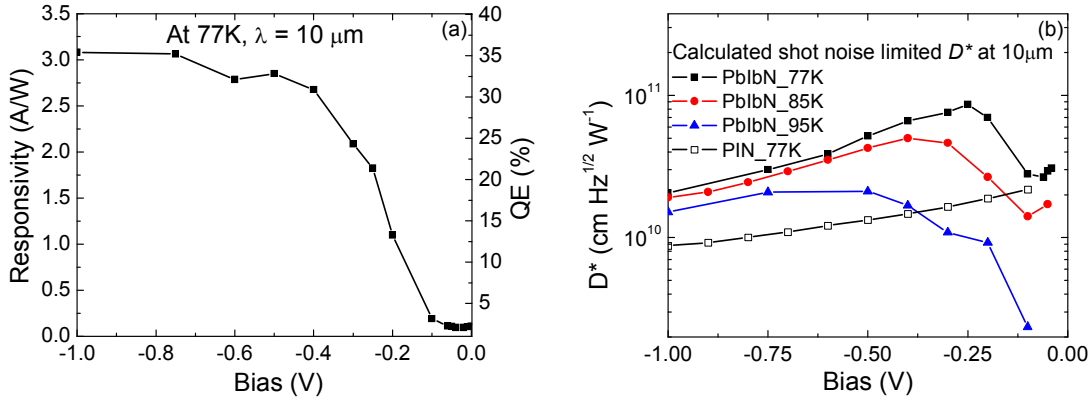


Fig. 5.5(a) Responsivity and QE as a function of applied bias for the pBiBn design at 10 μm, (b) calculated shot noise limited $D^*$ for pBiBn and PIN designs at 10 μm at different temperatures and bias values.

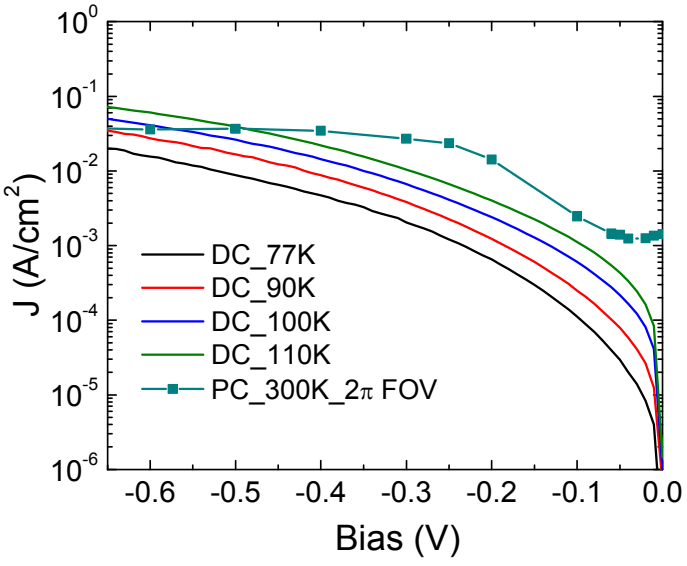


Fig. 5.6. Background photocurrent density and dark current densities at different temperatures for pBiBn Design 1.

**Design 2**

Though the Design 1 demonstrated a significant improvement over the PIN design, it was an unoptimized design and needed high bias (250mV) for operation. For photodetectors, a lower bias operation is preferred because all the components of dark current increase with the increase in bias. We worked on the optimization of barriers and doping in the absorber region to improve the performance further and reduce the bias of operation. In the next generation pBiBn, EB and HB layers were designed with higher bandgap superlattices. This could also facilitate the incorporation of wider bandgap contacts than in Design 1. We also doped the absorber LWIR T2SL with Be, as it has been shown that electrons, which are minority carriers in p-doped T2SL, have favorable transport than holes[109].

The schematic of the second generation pBiBn design has been shown in Fig. 5.7(a). The absorber is made of 14ML InAs/7ML GaSb LWIR T2SL, and is doped p-, such that the Be cell temperature was adjusted to incorporate a dopant density of $1x10^{16}$ $cm^{-3}$ at typical growth rates of InAs and GaSb. For doping the absorber, Be shutter was kept open for all the layers, while for the contact layers, N+ contact was made by doping only the InAs layer and P+ contact by doping the GaSb layers of T2SLs. The EB layer has been designed with a strained GaSb/AlSb superlattice, with a bandgap of 1.19eV. This barrier layer facilitates an increase in the bandgap of the P+ contact layer to 0.424eV, such that the CBO between EB layer and the contact layer is sufficient to block diffusion of minority carriers from the contact into the absorber region. Similar design consideration were used for HB and N+ contact layers which are made of 16ML InAs/4ML AlSb T2SL and 9ML InAs/4ML GaSb T2SL, respectively. The equilibrium heterojunction

bandstructure has been shown in Fig. 5.7(b) at 77K, where band alignments were obtained using EPM and then heterojunction band diagram with Sentaurus TCAD.

The material was fabricated into single pixel detectors and the side walls were encapsulated with silicon dioxide ($SiO_2$) to reduce surface leakage currents. The spectral response measurements have been shown in Fig. 5.8(a), from 77K till 200K at an operating bias of -100mV. A 0% cutoff wavelength of 10μm and 11.7μm has been observed at 77K and 200K, respectively. Fig. 5.8(b) shows dark current density as a function of bias for temperatures ranging from 60K to 176K. A dark current density of $1.42x10^{-5}A/cm^2$ has been measured at 76K and -60mV of applied bias. Fig. 5.9 shows the Arrhenius plot of dark current density against the inverse of temperature. It shows that in low temperature range, below 80K, the activation energy is close to 8meV while at higher temperatures, it is close to the bandgap of the absorber. This suggests that the dark current is limited by the diffusion process for the temperatures above 80K and by tunneling mechanism (or surface leakage) for lower temperatures. This indicates that the barrier layers are effective in reducing the electric field drop across the absorber region, and hence the performance of this device is not limited by the SRH process, which usually results in midgap activation energies. The dark current density is a factor of 1.4 higher than that reported in the literature[110], for state of the art T2SL LWIR detectors, which also has a higher cutoff wavelength.

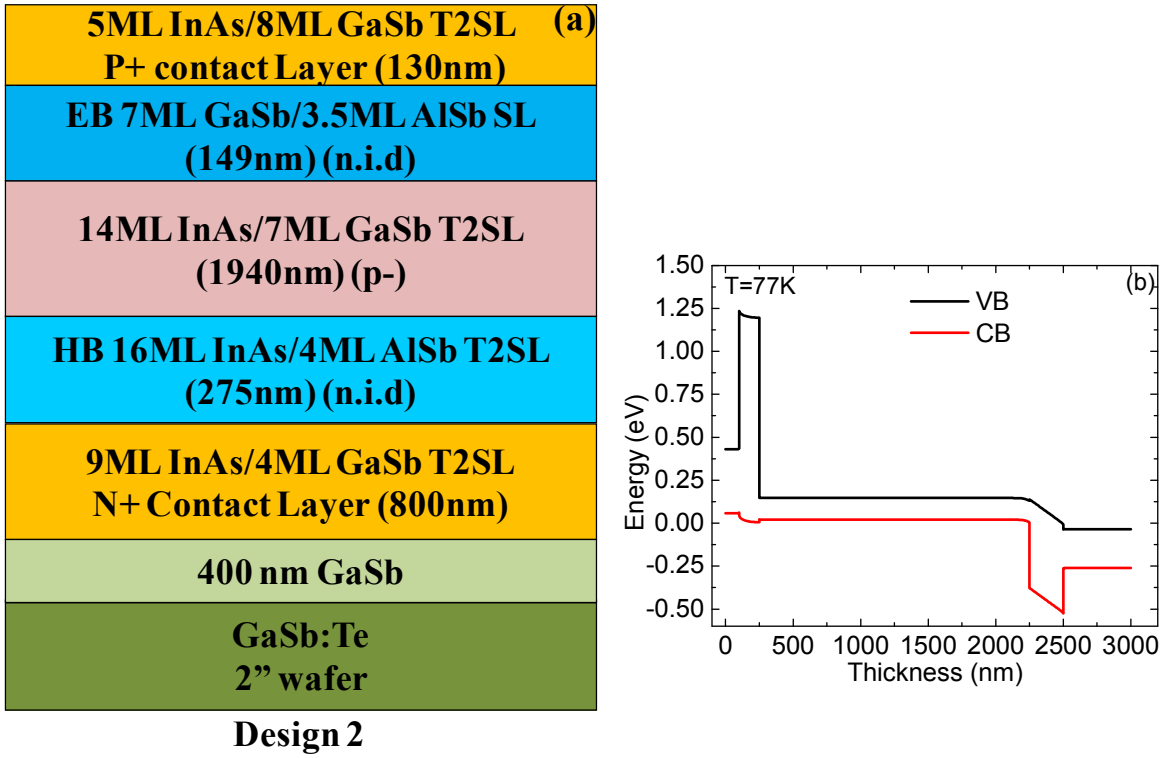


Fig. 5.7. (a) Strcuture schematic of pBiBn Design 2, (b) calculated equivalent energy band diagram of Design 2 at 77K.

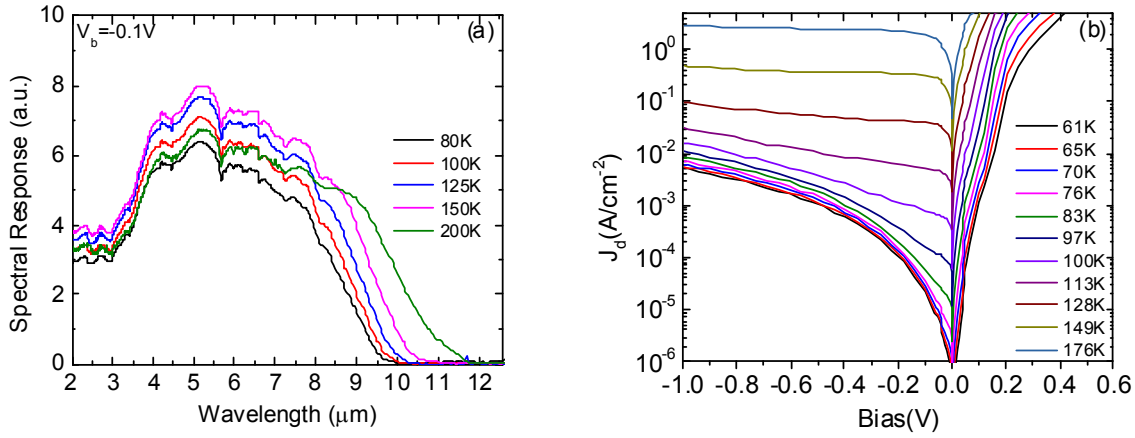


Fig. 5.8. (a) Measured spectral response and (b) dark current density as a function of temperature for pBiBn Design 2.

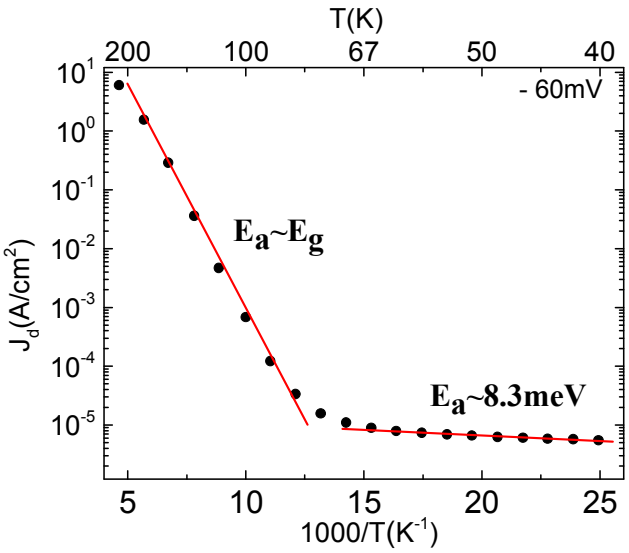


Fig. 5.9. Arrhenius plot of dark current density as a function of inverse of temperature, at 60mV of applied reverse bias.

The radiometric characterization was carried out with a calibrated black body source at 900K. The responsivity and detectivity as a function of temperature have been shown in Fig. 5.10. It shows measured detectivity, at 2π field of view with a 300K background, and the detectivity calculated using thermal noise and shot noise due to the dark current. The later is a figure of merit commonly reported in the literature. We measured a detectivity of $3.7x10^{10}$ cm-Hz$^{1/2}$-W$^{-1}$ and a corresponding responsivity of 1.66A/W at 8.7μm and 77K (-60mV), which translates into a QE of 23.5%. The calculated peak detectivity is $7.7x10^{11}$ cm-Hz$^{1/2}$-W$^{-1}$, at -40mV and 77K, and the corresponding QE is 21% at 8.7μm. At 150K, a responsivity of 2.88A/W with a corresponding QE of 40% was measured at -250mV. An increase in responsivity with temperature was observed for this device, which is due to an increase in absorption coefficient. Calculated peak detectivities at 100K, 125K and 150K are $1.5x10^{11}$ cm-Hz$^{1/2}$-W$^{-1}$, $2.6x10^{10}$ cm-Hz$^{1/2}$-W$^{-1}$, and $8.7x10^{9}$ cm-Hz$^{1/2}$-W$^{-1}$, respectively. The device demonstrated maximum detectivity at very small

bias values, which is beneficial as most of the dark current components increase with applied bias. Table 5.1 compares the performance of Design 1 and Design 2 at 77K. Design 2 demonstrated almost two orders of magnitude reduction in dark current as compared to Design 1, however, it is to be noted that Design 1 has a higher cutoff wavelength than Design 2.

| **Designs** | **0% cutoff wavelength** | **Dark current density (A/cm$^2$)** | **Responsivity (A/W)** | **Calculated *D**** **(cm-Hz$^{1/2}$-W$^{-1}$)** |
|---|---|---|---|---|
| Design 1 | 11.8μm | $1.2\times10^{-3}$ | 1.8 | $8.7\times10^{10}$ (λ=10μm) |
| Design 2 | 10.0μm | $1.4\times10^{-5}$ | 1.66 | $7.7\text{x}10^{11}$ (λ=8.7μm) |

Table 5.1. Comparison of performance of Design 1 and Design 2 at 77K.

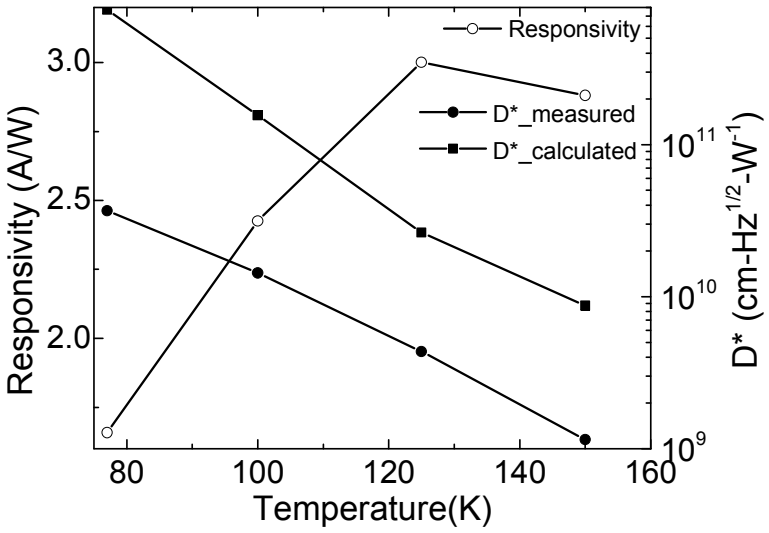


Fig. 5.10 Measured responsivity, measured detectivity with 2πFOV, (300K background) and calculated detectivity of pBiBn Desin 2 as a function of temperature.

## 5.4 pBiBn MWIR Detectors

The efforts in MWIR T2SL research have been focused towards the realization of HOT detectors. A HOT detector can drastically reduce the cost as well as the size of FPA. In

this work, a MWIR T2SL detector based on pBiBn architecture was designed, grown, fabricated and tested, as described below.

The heterojunction schematic of the detector is shown in Fig. 5.11(a). The contact layers and barrier layers with appropriate bandoffsets were first designed using EPM, as discussed previously. The structure was then grown on GaSb:Te substrate. The detector structure was grown on a 400nm thick GaSb buffer layer. The bottom contact layer is made of 6ML InAs/7ML GaSb T2SL, which is followed by the HB layer made of 11ML InAs/4ML AlSb T2SL. The absorber region is made of 1μm thick 9ML InAs/9ML GaSb MWIR T2SL, which is followed by an EB layer made of 8ML GaSb/5ML AlSb superlattice. The top contact layer is made of 5ML InAs/8ML AlSb T2SL.

The spectral response measurements were carried out at different temperatures from 77K to 295K, shown in Fig. 5.11(b). It shows a 0% cutoff wavelength of 5μm and 6.2μm at 80K and 295K, respectively, at an applied bias of -100mV. It can be seen that the photocurrent signal strength does not change from 80K to 200K and above 200K, we see decrease in signal. This suggests that the recombination of photogenerated carriers, which leads to a decrease in the photocurrent, does not have temperature dependence till 200K. At temperatures beyond 200K, carrier lifetimes possibly reduce with increasing temperature. There have been reports on the carrier lifetime measured in T2SL at 77K[28], however the temperature dependence of carrier lifetimes need further investigation.

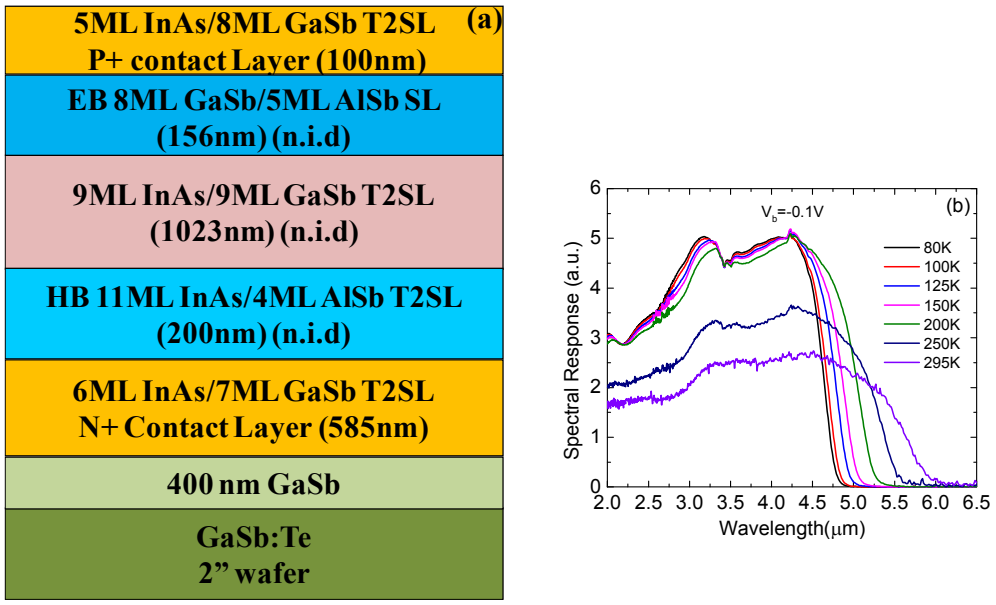


Fig. 5.11 (a) Structure schematic and (b) measured spectral response at different temperatures, of MWIR pBiBn detector.

The current-voltage relationship of the device has been shown in Fig. 5.12(a). A dark current density of $1.6\text{x}10^{-7}\text{A/cm}^2$ and $6.8\text{x}10^{-2}\text{A/cm}^2$ was measured at 80K and 200K, at an applied bias of -30mV and -80mV, respectively. The Arrhenius plot of dark current density with respect to the inverse of temperature has been shown in Fig. 5.12(b). It suggests that the limiting dark current mechanism at temperatures higher than 80K is the diffusion process since the activation energy is close to the bandgap of the absorber region. However, at lower temperatures, the activation energy is close to 45meV which reveals the dominant mechanism to be surface leakage or tunneling currents. This MWIR design, similar to the LWIR pBiBn Design 2, does not show SRH limited dark current behavior.

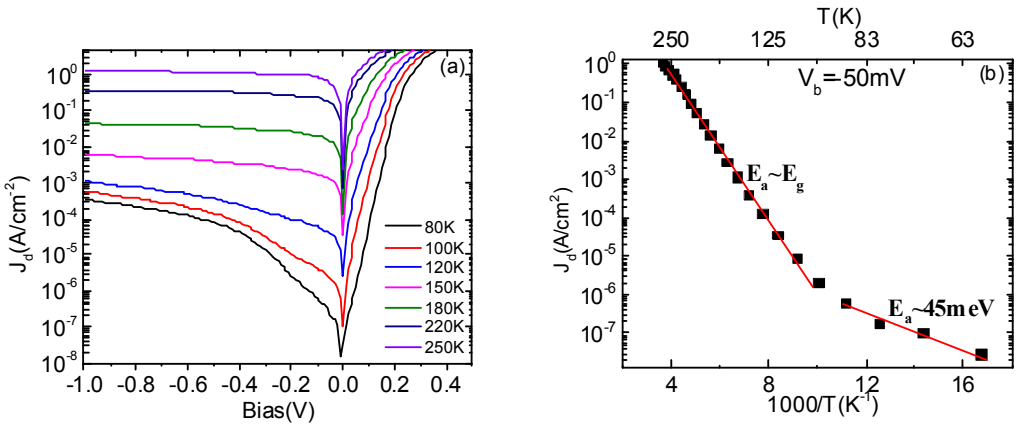


Fig. 5.12. (a) Dark current density and (b) Arrhenius plot of dark current density with respect to the inverse of temperature, for MWIR pBiBn detector.

Radiometric characterization was carried out using a calibrated black body source at 900K. Fig. 5.13(a) shows the radiometric characterization data of the device at 77K, $\lambda$=4.2μm, measured with a calibrated black body at 900K. The measured peak detectivity of 2.1x10$^{11}$ cm-Hz$^{1/2}$-W$^{-1}$, with 2π FOV and 300K background, was observed at -30mV, with a corresponding responsivity of 1.3A/W (QE=38%). While the detectivity calculated from thermal noise and shot noise due to dark current showed a peak value of 8.9x10$^{12}$ cm-Hz$^{1/2}$-W$^{-1}$, at -10mV. We also observed that there is no significant change in responsivity with bias and hence this device can be operated at a very small bias without compromising on the QE. This also reflects that the barrier layers do not offer any resistance to the flow of photogenerated carriers and validates the use of EPM for predicting bandoffsets and bandgaps in superlattices made of the 6.1Å family. Fig. 5.13(b) shows the variation of responsivity and measured detectivity as a function of temperature. As stated above, the responsivity does not show dependence on temperature.

A measured detectivity of $3.2\text{x}10^{9}$ cm-$Hz^{1/2}$-$W^{-1}$ and $4.2\text{x}10^{8}$ cm-$Hz^{1/2}$-$W^{-1}$ was observed at 175K and 200K, respectively, at $\lambda$=4.2μm.

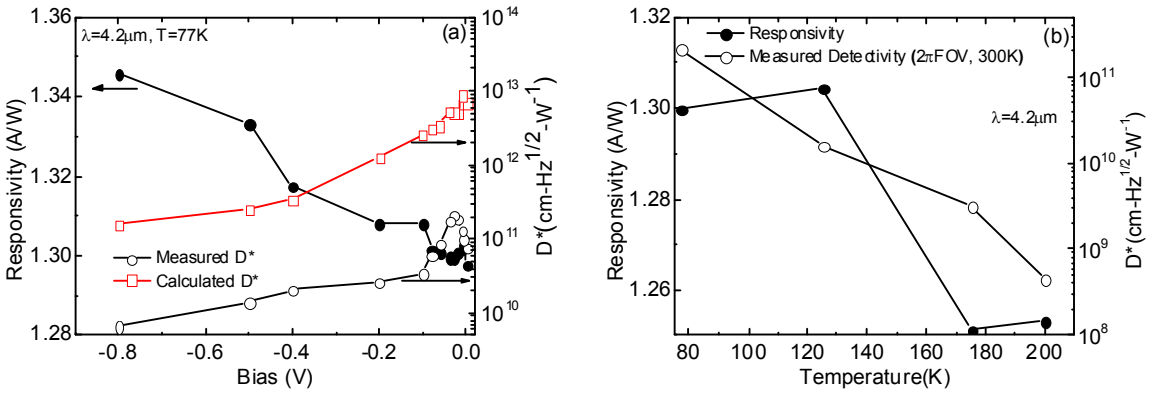


Fig. 5.13 (a) Responsivity, measured detectivity and calculated detectivity at 77K, (b) Measured responsivity and peak detectivity at 2π FOV, 300K background as a function of temperature, at λ=4.2μm.

## 5.5 Multicolor Detection using Barrier Infrared Detectors

Multicolor detection capabilities are important for the realization of fourth generation infrared detectors[111]. As a part of this thesis, two color and three color detectors based on T2SL system were realized as discussed below. The devices fabricated were as three contact structures. FPA realization of the device structure would require three bumps per pixel technology. Read out integrated circuits (ROICs) with three indium bumps per pixel (for simultaneous two color detection) have already been demonstrated[112]. In this section, we will first discuss the two color detector and then go over the three color detector.

### 5.5.1 Dual Band Detector

The dual band detector, to detect MWIR and LWIR radiation simultaneously, was developed in this work, using the unipolar barriers. The detector architecture has been

shown in Fig. 5.14 (a), depicting a three contact device, with pBiBn architecture implemented for MWIR as well as LWIR detection. Top and bottom contact layers are used for detection of MWIR and LWIR, respectively, with the middle contact layer being the common contact between the two absorber regions. This device is meant for top illumination and hence the MWIR absorber is on the top. The advantage of such a design is the simultaneous operation of the two bands along with significant reduction in dark current due to barrier layers.

The schematic of the detector structure has been depicted in Fig. 5.14 (a). The bottom N+ contact layer is made of 16ML InAs/7ML GaSb T2SL, followed by a hole barrier layer for LWIR absorber made of 15.4ML InAs/4ML AlSb T2SL. This is followed by 1.5μm thick LWIR absorber region, doped with Be to a level of $5x10^{15}$ $cm^{-3}$. The next layer is an EB region made of 6ML InAs/10ML GaSb T2SL and then the middle P+ contact layer common for both the absorbers. On top of the P+ contact layer is an EB layer for MWIR absorber, made of 100nm thick $Al_{0.2}Ga_{0.8}Sb$, then followed by a 1.5μm thick MWIR absorber region made of 8ML InAs/8ML GaSb T2SL non-intentionally-doped. The HB layer is made of 12ML InAs/5ML AlSb T2SL and on top of it is the N+ contact layer made of InAs. The band-diagram of the detector is shown in Fig. 5.14 (b), depicting the CBO and VBO between various regions. The band alignment has been obtained with EPM.

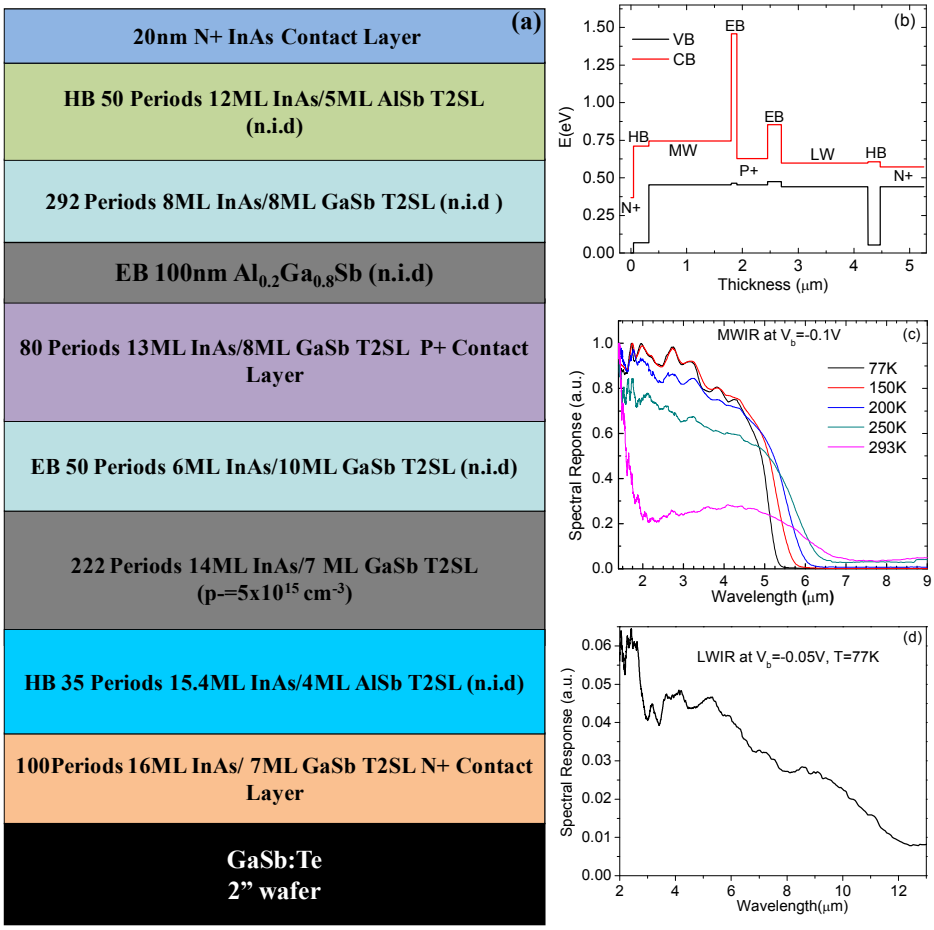


Fig. 5.14. (a) Heterojunction schematic, (b) Band diagram obtained with EPM, (c) Variable temperature spectral response of MWIR band and (c) 77K spectral response of LWIR band, of dual band T2SL detecor

The MWIR detector was characterized up to room temperature. Fig. 5.14 (c) show the spectral response measured at different temperatures. It demonstrated a 0% cutoff wavelength of 5μm and 7μm at 77K and 293K, respectively, at -100mV of applied bias. The characterization of LWIR detector was carried out at 77K, and as can be seen in Fig. 5.14 (d), it demonstrated a cutoff wavelength of 12μm at -50mV of applied bias. Radiometric characterization of both MWIR and LWIR detectors was carried out with a calibrated black body source at 900K. Measured responsivity and detectivity has been

shown in Fig. 5.15 (a) and (b), for MWIR and LWIR detectors, respectively. For MWIR detector, measured responsivity and detectivity for 2πFOV (300K background), has been shown against temperature at a wavelength of 4.9μm. The detector demonstrated responsivity of 1.18A/W and 1.44A/W at 77K and 200K, respectively, while the corresponding measured $D^*$ is $6.5\text{x}10^{10}$ cm-$\text{Hz}^{1/2}$-$\text{W}^{-1}$ and $2.5\text{x}10^{8}$ cm-$\text{Hz}^{1/2}$-$\text{W}^{-1}$. For LWIR detector, at 77K and a wavelength of 9μm, responsivity of 0.18A/W and measured $D^*$ of $8.4\times10^{8}$ cm-$\text{Hz}^{1/2}$-$\text{W}^{-1}$ was observed. It is to be noted that the dual band structures were realized before the optimal pBiBn LWIR design. The performance of dual band detector can be increased significantly if the optimized LWIR and MWIR designs are take into consideration.

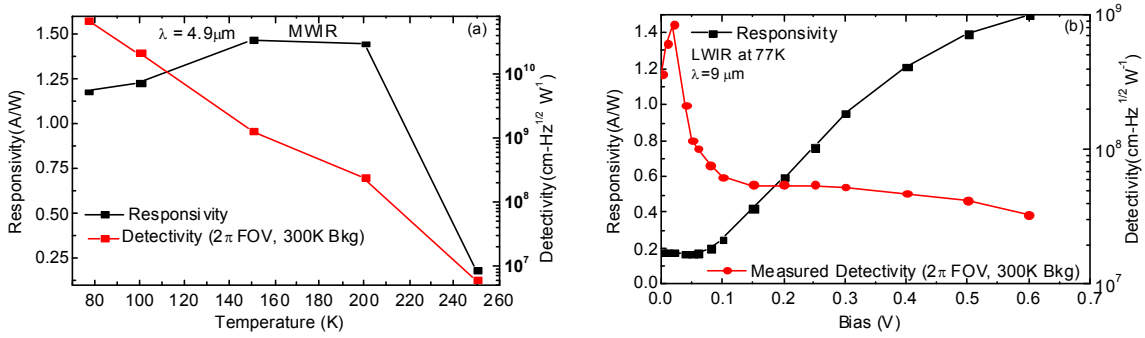


Fig. 5.15. Measured responsivity and detectivity with 2π FOV, 300K background of (a) MWIR and (b) LWIR bands of dual band T2SL detector.

### 5.5.2 Three Color Detector

The three-color detector is a three terminal device using an nBn-nBiBp heterostructure with a top N-contact, a middle N-contact and a bottom P-contact. The SWIR and MWIR absorbers are embedded in nBn[113], architecture between the top and the middle contact whereas the LWIR absorber is incorporated in nBiBp [23] section between the middle and the bottom contact. The dual color nBn device provides sequential SWIR/MWIR

detection by switching the polarity of the applied bias. The LWIR detector region's nBiBp heterojunction design has a hole blocking layer sandwiched between the absorber region and the N contact layer, where "i" refers to the absorber region. Fig. 5.16 shows the calculated band-alignment, Fermi level ($E_f$) and electric-field profile across the entire device when no external bias is applied. The EPM and Sentaurus TCAD were used for electric field calculations and equilibrium band diagram calculations. As can be seen from Fig. 5.16, the hole blocking layer (16ML InAs/4ML AlSb T2SL) in the LWIR section of the device blocks the flow of minority carrier holes from the N contact layer into the absorber region and hence reduces the noise in the system. Moreover, the electric field drops across the wider band gap barrier layer leading to reduced SRH recombination. There is also a significant field drop across the 40 period thick 6ML InAs/10ML GaSb T2SL layer sandwiched between the LWIR absorber region and the bottom P+ GaSb contact layer. The LWIR nBiBp section can be operated independent of the MWIR and SWIR nBn section by applying reverse bias between the middle contact and bottom contact.

The structure was grown on a P+ (Zn) doped GaSb substrate. The schematic of the device and high resolution X-Ray diffraction pattern are shown in Fig. 5.17 (a) and (b), respectively. The SWIR absorber is made of 190 periods of 5ML InAs/10ML GaSb T2SL ($n=5\times10^{16}$ $cm^{-3}$), the MWIR absorber consists of 190 periods of 8ML InAs/8ML GaSb T2SL ($n=1\times10^{16}$ $cm^{-3}$) and the LWIR absorber is made of 200 periods of 14ML InAs/7ML GaSb T2SL ($p=5\times10^{15}$ $cm^{-3}$). It is a top-side illumination device and hence the absorber sequence from top to bottom is SWIR, MWIR and LWIR regions. The nBn section of the device enables a bias tunable response between the SWIR and MWIR

absorber regions which are separated by a 100nm thick $Al_{0.2}Ga_{0.8}Sb$ barrier layer, similar to an earlier reported bias tunable MWIR-LWIR nBn detector[94]. The main advantage of nBn is the reduction in field drop across the smaller bandgap active region leading to a reduction in SRH recombination.

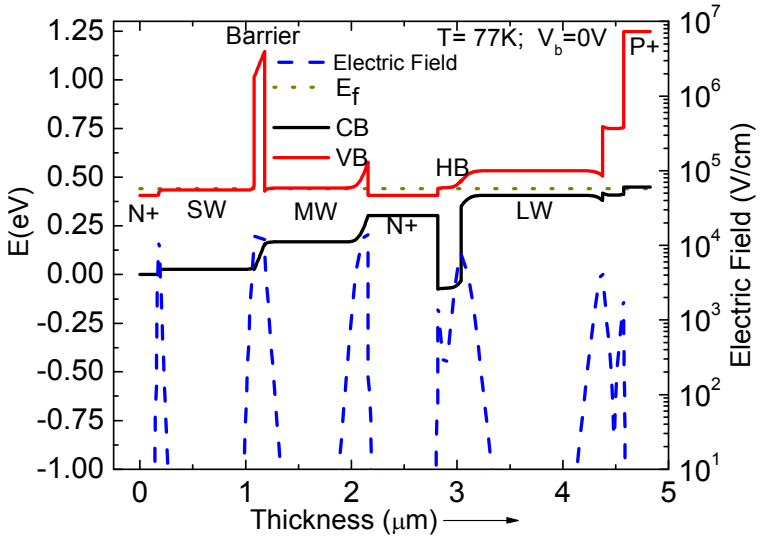


Fig. 5.16. Heterojunction equilibrium band diagram of three color detector obtained using EPM and Sentaurus TCAD. It also shows the electric field profile across the device in equilibrium.

After MBE growth, the single pixel array of detectors was fabricated. The devices were passivated with SU-8 to reduce surface leakage current.

Spectral response measurements of these devices were performed at 77K. Fig. 5.18 shows the spectral response when a bias is applied between the top and middle contact, and the bottom contact is floating. When a negative bias is applied to the top contact, the photogenerated electrons in the MWIR absorber are collected at the middle contact, while the photogenerated holes are collected at the top contact. The electrons from the SWIR

region are blocked by the $Al_{0.2}Ga_{0.8}Sb$ barrier layer from reaching the middle contact, thus leading to reduced spectral cross talk. On the other hand, when a positive bias is applied at the top contact, photogenerated electrons from SWIR region are collected at the top contact and photogenerated holes are collected at the middle contact. In this case, the electrons from the MWIR absorber are blocked by the barrier layer. The 50% cutoff wavelength ($\lambda_c$) for MWIR and SWIR response is 4.7µm ($V_b$=-0.5V) and 3µm ($V_b$=0.6V), respectively. Fig. 5.18 also shows the spectral response of the LWIR region ($\lambda_c$ =10.1µm), when a reverse bias of 10mV is applied between across middle and bottom contacts, while the top contact is floating. The inset of Fig. 5.18 shows the response from the LWIR absorber from 8µm to 12µm, the range in which LWIR detector has been characterized using a band pass filter, as described in the text below.

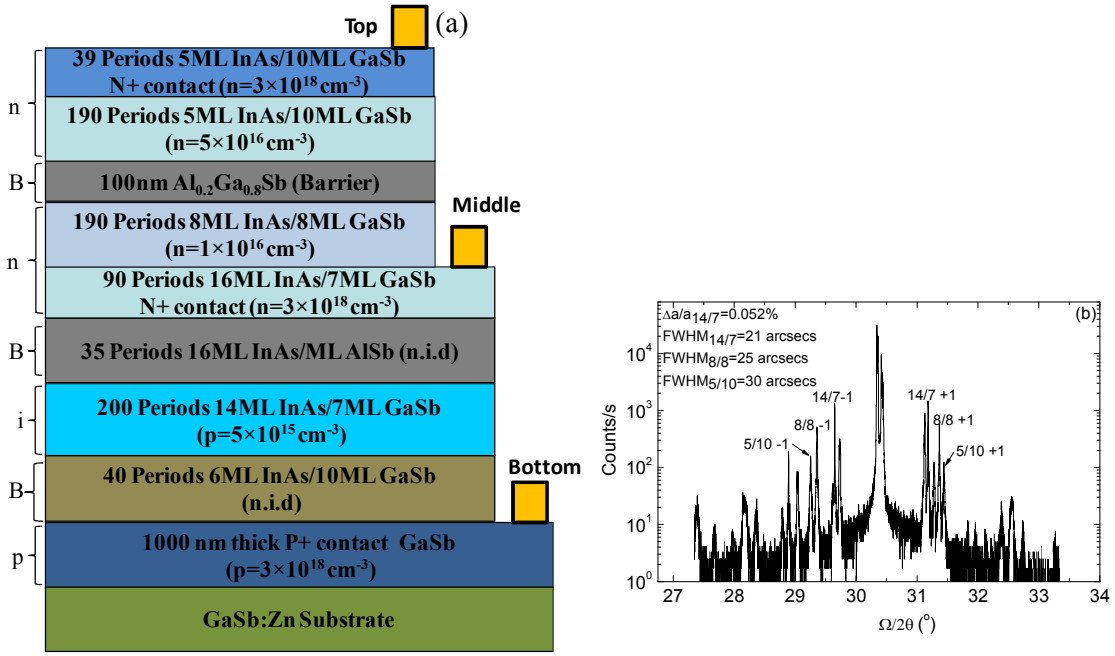


Fig. 5.17. (a) Detector schematic showing the absorber, barrier and contact layers (b) High resolution XRD spectrum of three color detector.

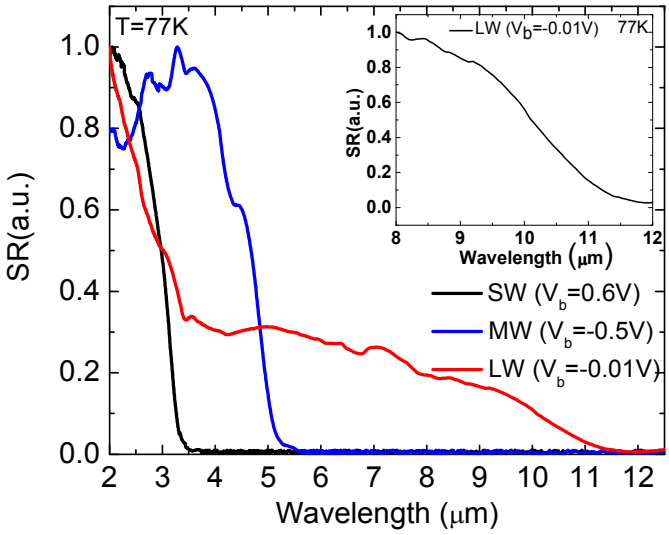


Fig. 5.18. Spectral response of three color detector at 77K, showing the SWIR, MWIR and LWIR spectra.

Fig. 5.19 shows the dark current densities plot for this device at 80K. The LWIR curve represents the current voltage curve between the middle and the bottom contact. The SWIR/MWIR curve corresponds to the response between the top and the middle contact, with the negative bias corresponding to MWIR detection and the positive bias corresponding to SWIR detection. The dark current density for MWIR region at $V_b$=-0.5V is $3.1\times10^{-5}$ A/cm$^2$ and is $2.0\times10^{-6}$ A/cm$^2$ for SWIR detection at $V_b$=-0.6V. The dark current density for LWIR signal at -10mV of applied bias is observed to be $1.8\times10^{-4}$ A/cm$^2$.

Calibrated radiometric measurements were carried out at 77K using a calibrated blackbody source at 900K. Fig. 5.20 shows the measured responsivity and detectivity for SWIR, MWIR and LWIR signals. It is to be noted that since the T2SL devices with cutoff in LWIR region give a broad response, a band-pass filter (8μm -11.5μm) was used to characterize the LWIR signal. The observed responsivity and QE for SWIR, MWIR

and LWIR signals are 0.30A/W and 14.9% ($\lambda$=2.5μm), 0.41A/W and 12.7% ($\lambda$=4μm) and 0.77 A/W and 10.7% ($\lambda$=8.94μm), respectively. The QE can be increased by increasing the thickness of the absorber layer. The measured $D^*$, at the wavelengths specified earlier, for 2π FOV and 300K background for SWIR, MWIR and LWIR absorbers are $1.4\times10^{10}$ cm-Hz$^{1/2}$W$^{-1}$ ($V_b$=0.6V), $1.8\times10^{10}$ cm-Hz$^{1/2}$W$^{-1}$ ($V_b$=-0.5V) and $1.5\times10^{9}$ cm-Hz$^{1/2}$W$^{-1}$ ($V_b$=-0.01V). SWIR, MWIR and LWIR detection regions demonstrated background limited performance at 80K under 2π FOV, 300K background. The detectivity due to Johnson noise and shot-noise was also calculated and at 77K, the calculated $D^*$ for SWIR, MWIR and LWIR is $1.8\times10^{12}$ cm-Hz$^{1/2}$W$^{-1}$ ($V_b$=0.01V), $1.4\times10^{11}$ cm-Hz$^{1/2}$W$^{-1}$ ($V_b$=-0.3V) and $9.9\times10^{10}$ cm-Hz$^{1/2}$W$^{-1}$ ($V_b$=-0.01V), respectively, as shown in Fig 5.20.

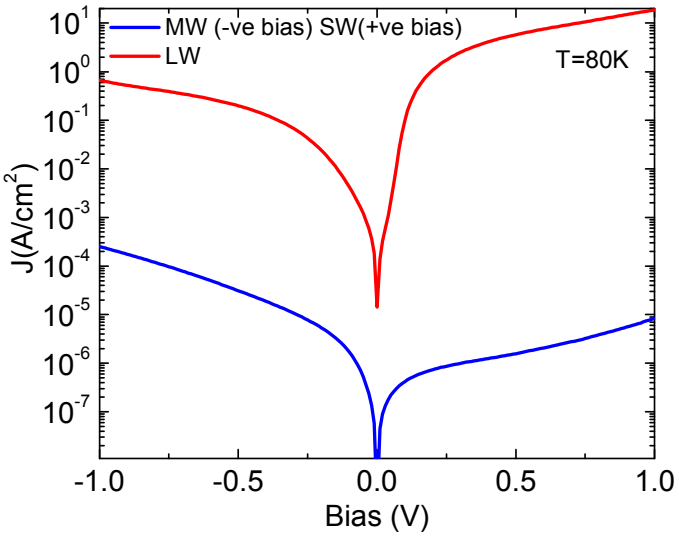


Fig. 5.19. Dark current densities from top to middle contact (SWIR/MWIR response) and bottom to middle contact (LWIR response), at 80K.

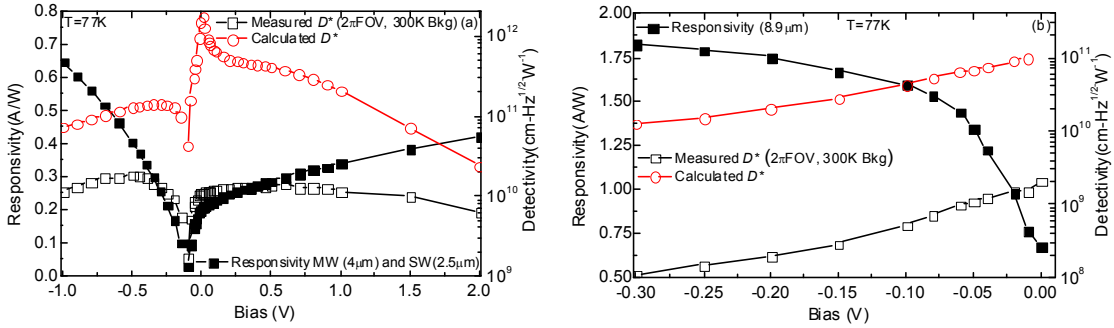


Fig. 5.20. Responsivity, measured $D^*$ and calculated $D^*$ for (a) SWIR and MWIR absorber regions, and (b) LWIR absorber region.

One of the concerns in multiband detectors is the spectral crosstalk. Superlattice detectors are broadband detectors and are susceptible to spectral crosstalk. The spectral crosstalk can be significantly reduced by increasing the thicknesses of absorber regions and using unipolar barriers to prevent photogenerated carriers from one color from reaching the opposite contact. Even with non-optimized detectors, Fig. 5.18 shows that there is no LW signal in MW spectrum and there is no MW/LW signal in SW spectrum. For a potential FPA application of this device, simple signal processing techniques can be used to observe response in a certain wavelength band.

In conclusion, the performance of T2SL detectors has been improved significantly with the realization of barrier photodiodes. The pBiBn heterojunction with an electron barrier and a hole barrier layer, which allow unimpeded flow of holes and electrons, respectively, while blocking the other carrier types. Incorporation of barrier layers in a photodiode reduced dark current without affecting the photocurrent, which demonstrated performance superior to homojunction PIN designs. Realization of barrier devices on T2SL system is possible due to the bandgap and band-offset tunability offered by the 6.1Å system. Also, this flexibility can be used to design and fabricate multi-color

detectors with unipolar barriers. In this work, dual color and three color detector designs were successfully implemented.

# 6 MWIR and LWIR Interband Cascade Detectors

In the previous chapter, the use of unipolar barriers for dark current reduction in T2SL photodetectors was discussed, and also the requirements for high operating temperature (HOT) detectors were emphasized. While no photoconductive gain measurements were carried out, it considered to be unity for photodiodes. In this chapter we focus on the use photoconductors, with an inbuilt photoconductive gain (PC Gain) less than unity, for HOT operation. The detectors have demonstrated photovoltaic operation at zero bias. PC Gain less than unity is particularly appealing for HOT FPAs, when detection is limited by read out integrated circuit (ROIC) charge well capacity.

In this work interband cascade infrared photodetectors (ICIP) were realized on the T2SL system for MWIR and LWIR detection. The devices consisted of a seven stage active region, with each stage comprised of an absorber region, relaxation region and interband tunneling region. The absorber region is composed of a MWIR type-II (broken bandgap) InAs/GaSb SLS, the relaxation region is made of a graded type-II (staggered bandgap) InAs/AlSb SLS, and the interband tunneling region is made of a GaSb well in between AlSb barriers. Electro-optic and radiometric characterization was carried out to evaluate the performance. Dark current data was analyzed to assess the dominant component of dark current.

ICIP detector based on T2SL absorber was first reported by Yang *et al.*[52, 114, 115]. The device reported by them had an absorber region made of 9ML InAs/9ML GaSb

T2SL. The device design had seven stages and each stage consisting of absorber region, transport region and tunneling region. The key features of the device were high operating temperature, low dark currents and hence the noise. The schematics of one stage of the cascade detector reported by Yang *et al.* has been shown in Fig. 6.1, which depicts the absorber region, transport or relaxation region and the tunneling region. The key highlights of their detector structure and comparison with the design reported in this work have been bulleted below.

a) The absorber region is made of 9ML InAs/9ML GaSb T2SL, same as that used in this work for MWIR detector.

b) Design by Yang *et al.* consists of InAs QWs and AlSb barriers in the relaxation or transport region, where LO phonons are used for transport from one QW into the next. We believe that the transport using phonons is not efficient especially when multiple QWs are used, and it is sensitive to temperature as phonon energy distribution changes. While our design has graded InAs/AlSb T2SL as the relaxation region, as the resonant transport through T2SL is much more efficient and less temperature sensitive.

c) Design by Yang *et al.* relies on resonant tunneling for transport in the tunneling region, while the interband tunneling region in our device is designed so that the difference in hole energies is close to the longitudinal optical (LO) phonon energy in AlSb, to facilitate phonon-assisted tunneling.

d) Design by Yang *et al.* has N+ InAs contact layer, while in our design contact is made of much wider bandgap InAs/AlSb T2SL, which helps in reducing dark current such as tunneling currents.

The interband cascade devices based on T2SL system are important technology as well interesting for device physics research. These devices can have ultra low noise needed for realizing HOT detectors, built-in gain less than unity, which is important for HOT operation. They act as a challenging platform for device physics understanding as the presence of a large number of hetero-interfaces make the carrier transport a complicated one. A cartoon representation of one stage of the cascade detector realized in this work is shown in Fig. 6.2, which shows absorber region (1), interband tunneling region (2) and the transport region (3).

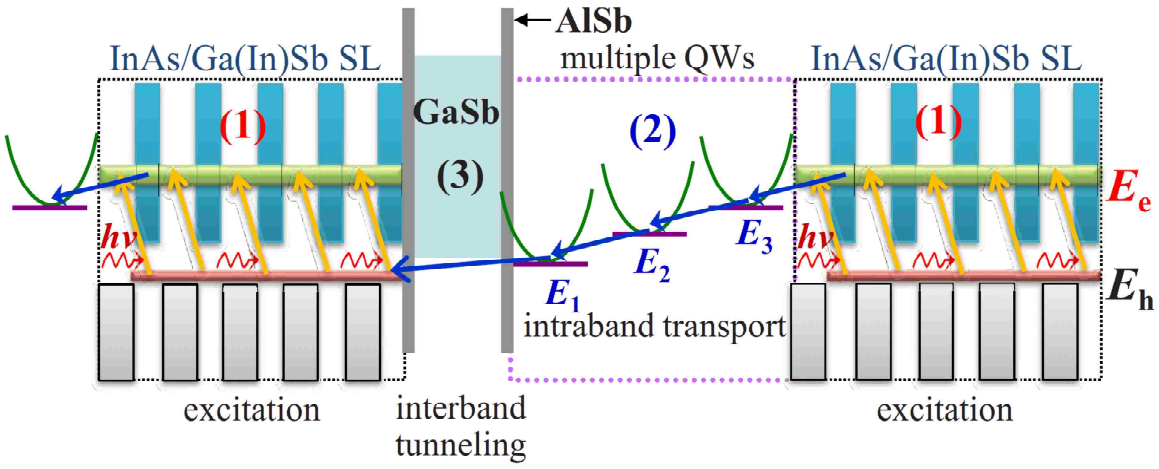


Fig. 6.1. Schematic of the ICIP detector showing, absorber, tunneling and relaxation regions, reprinted with permission from [116].

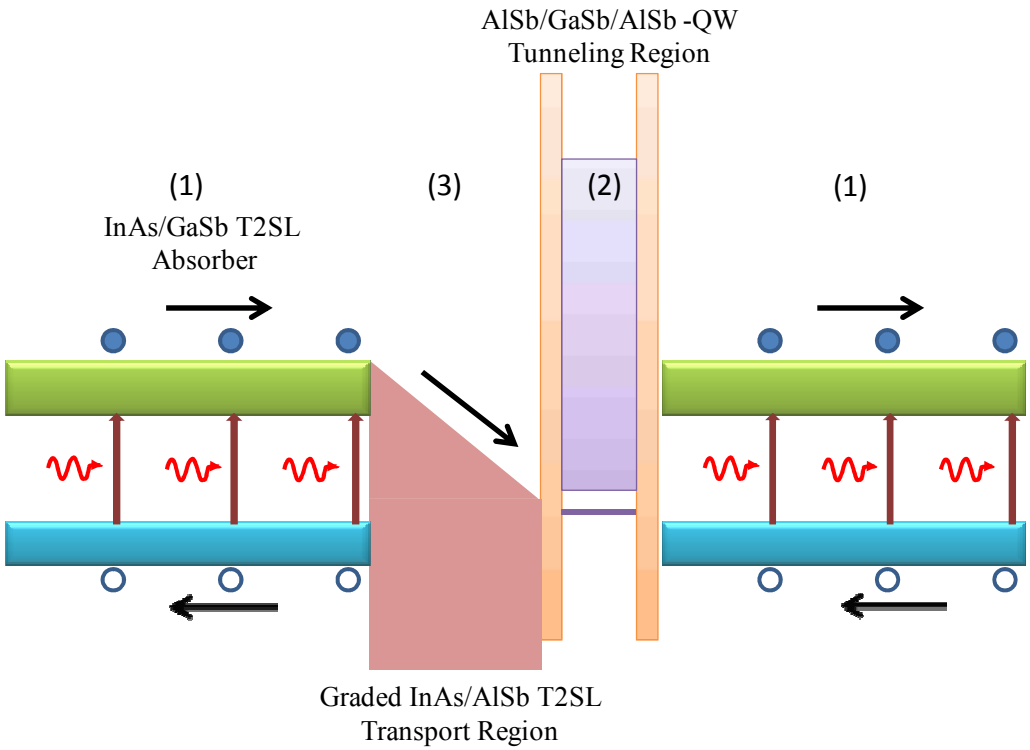


Fig. 6.2. Cartoon representation of cascade devices realized in this work showing the absorber region, interband tunneling region and transport region.

## 6.1 MWIR Cascade Detector

The heterostructure schematic of the MWIR structure is illustrated in Fig. 6.3(a). The device consists of a bottom contact layer, composed of 12.5ML InAs/5ML AlSb SLS, that is N+ doped with Gallium Telluride (GaTe) to a level of $3\times10^{18}$ $cm^{-3}$. It is followed by seven cascade stages, which precede a 2nm thick AlSb tunneling barrier, and then the top contact layer, made of GaSb (P+), doped at $3\times10^{18}$ $cm^{-3}$ with Beryllium (Be). The absorber region is made MWIR 9ML InAs/9ML GaSb SLS, with thickness of 28 periods in each stage, and is non-intentionally-doped. The residual doping in MWIR T2SL at high temperatures has been reported to be n-type[65]. All the layers except for contact layers are non-intentionally-doped as well.

The bandstructure of different T2SL layers was first simulated with the help of EPM to get the correct valence and conduction band offsets with respect to the absorber. The graded composition, relaxation region, InAs/AlSb T2SL was designed using EPM simulations. The lowest conduction band lineup of this region, which is made of 20ML InAs/4ML AlSb T2SL, is higher than the quantized hole level in the tunneling region by LO phonon energy of AlSb which is 42.2meV. To find the thickness of GaSb well and AlSb barrier layers for the design of tunneling region, Schrödinger equation was solved for the GaSb quantum well surrounded by AlSb barriers and the effect of absorber region and transport region was ignored. The thicknesses were chosen such that the energy difference between the quantized valence band level in GaSb QW and the valence band of the absorber is close to the LO phonon energy of AlSb.

Fig. 6.3(b) explains the operation of the detector in the photo-voltaic mode. Photo-generation of electron hole pairs occur in the MWIR absorber region (1), and due to the built-in field, electrons move to the right while the holes move to the left. Electrons then relax in the graded T2SL transport region (3), while holes tunnel through region (2). The separation between the quantized energy level in the GaSb quantum well of region (2) and the valance band in region (1) was designed to be equal to the LO phonon energy in AlSb, to make the tunneling of holes a phonon-assisted process. The relaxation region (3) and the interband tunneling region (2) also act as hole and electron barriers, respectively, to block the flow of dark carriers from one cascade stage into the other. This device has an inbuilt unipolar barrier action as well, which was described in details in chapter 5. The junction between regions (2) and (3) acts as recombination site for electrons and holes which leads to photoconductive gain being equal to 1/N, where N is the number of

cascade stages[115]. The evaluation of PC gain for this device has been explained later in this section. Reduction in photoconductive gain and zero bias operation are extremely desirable properties for FPAs to obtain a low noise equivalent temperature difference (NETD) at a high operating temperature as it limits the rate at which the charge capacitor is filled. In the present design, the total thickness of the absorber is 1µm as there are seven stages, and the absorption QE can be increased by increasing the number of stages. However the conversion QE is lower than that of the absorption QE by a factor of N.

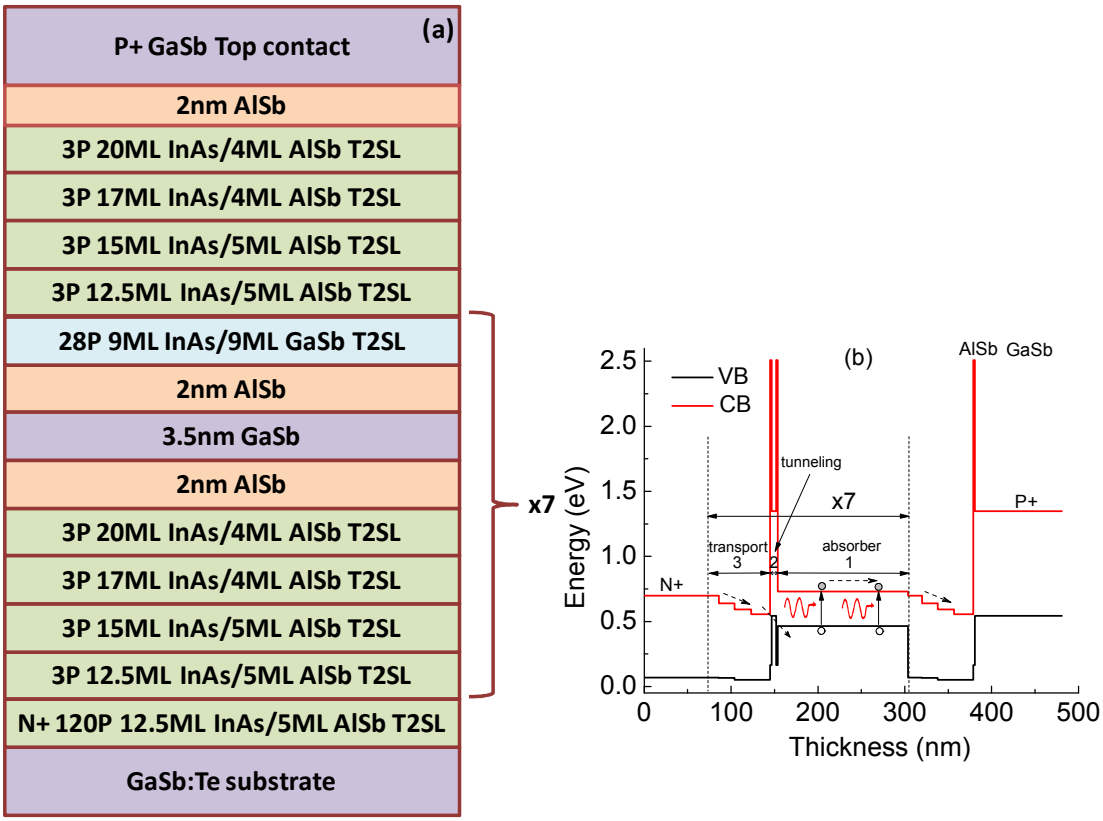


Fig. 6.3. (a) Structural schematic of the MWIR SLS cascade detector, 'P' stands for Periods. (b) Calculated energy band-diagram of cascade detector demonstrating flow of photo-generated carriers and band alignments of different segments. The band offsets of different layers have been obtained by empirical pseudopotential method.

The structure was grown in V-80H MBE system on an N+ (Te) doped GaSb substrate. Sources were calibrated using a reflection high energy electron diffraction system. Given

the complexity of the structure, growth rates were confirmed with multiple SLS growths, before the device growth, using X-ray diffraction . After MBE growth, the device fabrication was carried out using standard photolithography techniques and inductively coupled plasma etching for mesa definition. Finally, a Ti/Pt/Au ohmic contact was deposited to form the top and bottom contacts. The devices were then passivated with silicon dioxide ($SiO_2$) to reduce surface leakage current.

Material after growth was characterized using low temperature absorption measurements. The measurements were carried out at 77K, using a Thermo Nicolet Nexus 870 FourierTransform Infrared (FTIR) spectrometer. The glowbar source and liquid nitrogen-cooled HgCdTe detector of FTIR were used as the excitation source and the detector, respectively. First the transmission measurements were collected through the substrate which wass corrected with respect to the background as well. Then the background corrected transmission spectrum of the device under study was collected, which was processed further to correct for the substrate effects. The transmission spectrum was then converted into the absorption spectrum to obtain the absorption QE as well as the absorption coefficient. Further details of the absorption setup at CHTM can be found in [117]. The measured absorption QE spectrum of MWIR cascade detector is shown in Fig. 6.4(a). We obtained absorption QE of 45% at 4μm.

Spectral responses were undertaken from 77K to 420K, as shown in Fig. 6.4(b). The 100% cutoff wavelength of 5.2μm and 7μm were observed at 77K and 420K, respectively. Up to the room temperature (RT), good SNR was observed at zero bias, while at 420K the highest SNR was obtained at 0.5V, which is the highest reported operating temperature for any T2SL detector. Operation close to zero bias is important

for high temperature operation of focal plane arrays as most of the dark current components scale rapidly with the increase in applied bias[118]. The dark current density as a function of bias voltage has been shown in Fig. 6.5(a), and the Arrhenius plot with temperature in Fig. 6.5(b) at -5mV of applied bias.

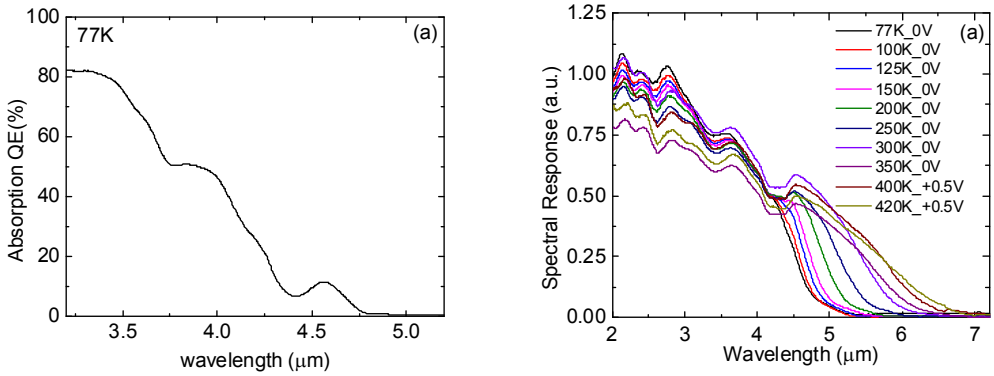


Fig. 6.4. (a)Absorption quantum efficiency at 77K, (b) spectral response from 77K-420K, with bias range specified in the legends.

Dark current density of $3.6\times10^{-7}$ A/cm$^{-2}$ and $7.3\times10^{-3}$ A/cm$^{-2}$ has been measured at 77K and 295K, respectively, at -5mV of applied bias. The dark current is dominated by tunneling, in the lower temperature range (70K-110K), indicated by small activation energy of 15 meV. While in the higher temperature range (130K-250K), the activation energy of 0.15eV (~$E_g/2$), indicating that the dominant dark current mechanism is Shockley Read Hall recombination current. This is due to a more dramatic increase in SRH currents with temperature as compared to tunneling currents. This also indicates that there is an electric field drop across the absorber region which can be minimized by carrying put a systematic study to look into the effect of doping in the absorber region on the detector performance.

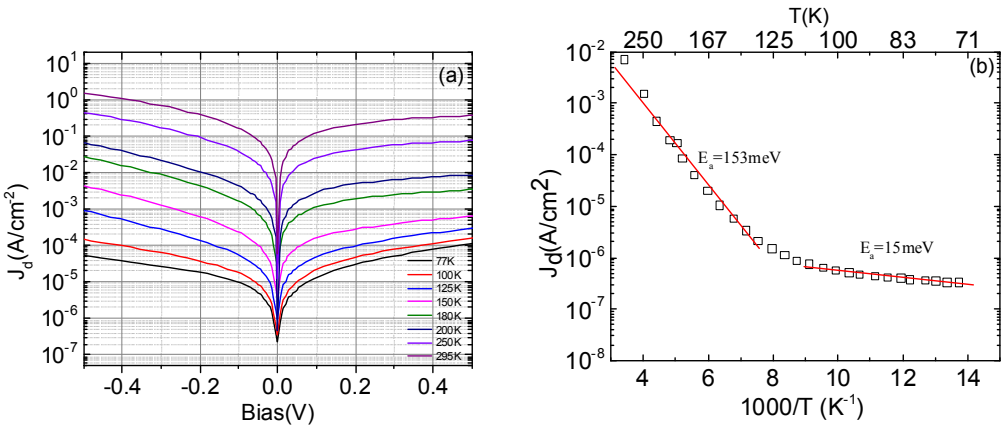


Fig. 6.5. (a) Dark current density as a function of bias for different temperatures. (b) Arrhenius plot of dark current density with temperature to calculate the activation energies in different temperature regimes.

Detailed radiometric characterization was carried out with a calibrated blackbody source at 900K, and the detector placed inside a variable temperature cryostat with 2π FOV, 300K background. The measured responsivity (4 μm, -5mV) and specific detectivity, measured with 2π FOV (300K background) and calculated Johnson noise limited regime, have been shown in Fig. 6.6 as a function of temperature. The responsivity of 0.167A/W (4μm) at 77K and $V_b$=-5mV was measured. If *G* denotes the photoconductive gain of the detector then the relationship between the responsivity and the absorption QE ($\eta_i$) is the following.

$R = \frac{\eta_i \lambda q}{hc} G$ , where $\lambda$, $q$, $h$ and $c$ are wavelength, electronic charge, Planck's constant and velocity of light in free space, respectively. From the absorption measurements, using Fig. 6.4(a), $\eta_i$ of 45% was observed at 77K and $\lambda$ = 4μm. This leads to the photoconductive gain (G) of 0.12 using responsivity equation. The device has seven stages, and one would estimate a gain of 1/7 or 0.14. The experimentally observed value

is close to the estimated value of PC gain. Conversion QE, which is defined as the product of $\eta_i$ and $G$, is 5.2%.

The Johnson noise limited detectivity has also been shown since that is a figure of merit commonly reported in the literature. It is calculated using the following relationship.

$D^* = \frac{R}{\sqrt{4kT/R_d A_d}}$, where $k$ is Boltzmann's constant, $R_d$ is the dynamic resistance, and $A_d$ is the diode area. At 77K, measured detectivity is $5.3\times10^{10}$ cm-$Hz^{1/2}W^{-1}$ and Johnson noise limited detectivity is $3.0\times10^{11}$ cm-$Hz^{1/2}W^{-1}$, while at 250K, measured detectivity and Johnson noise limited detectivities are, $4.4\times10^{8}$ cm-$Hz^{1/2}W^{-1}$ and $2.4\times10^{9}$ cm-$Hz^{1/2}W^{-1}$, respectively. At room temperature, the Johnson noise limited detectivity is $8.9\times10^{8}$ cm-$Hz^{1/2}W^{-1}$.

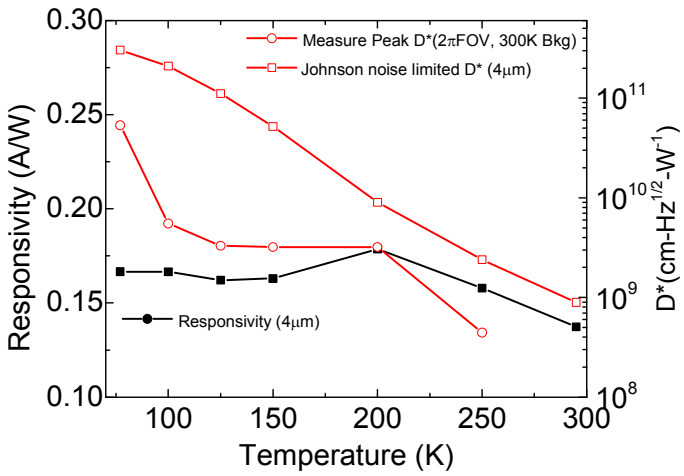


Fig. 6.6. Measured responsivity, measured specific detectivity with 2π FOV (300K background) and Johnson noise limited detectivity as a function of temperature.

## 6.2 LWIR Cascade Detector

The operating principle of LWIR T2SL cascade principle is similar to the MWIR device reported above and hence we will not indulge in the explanation of working principles of

LWIR device. The important aspect of LWIR device is the design of transport, tunneling and contact layers. In this section, we will discuss the design of LWIR cascade detector, and the experimental characterization data.

The LWIR detector was realized on 14ML InAs/7ML GaSb T2SL. The detector was grown on Te doped GaSb substrate in the V80-H MBE chamber. The schematic of the detector is shown in Fig. 6.7(a). It has seven stages, and like MWIR detector, each stage has an absorber region, relaxation region and tunneling region. The bottom contact layer is made of 16ML InAs/4ML AlSb T2SL. The relaxation region is made of graded InAs/AlSb T2SL, as shown in Fig. 6.7(a). The composition of this region has been modified as compared to the MWIR detector so that the conduction band energy of the absorber region can be close to the highest conduction band energy of the relaxation region which is determined by 16ML InAs/4ML AlSb T2SL. The absorber region is made of 24 periods thick 14ML InAs/7 ML GaSb T2SL and the interband tunneling region is made of 5.2nm GaSb well sandwiched between 2nm thick AlSb barriers. Please note that the GaSb well of tunneling region is thicker than that of the MWIR cascade structure, so as to maintain an energy difference close to LO phonon energy between the valence band of absorber and the quantized state of tunneling region well. This region is also crucial as it acts as an energy matching region between the relaxation and absorber regions. The seven cascade stages precede relaxation region, followed by 2nm thick AlSb and then the 100nm thick GaSb P+ contact layer at the very top. All the layers except for contact regions are non-intentionally-doped (n.i.d).

After epitaxial growth, the device was processed into single pixel detector arrays using standard processing method described above for MWIR detector. The sidewalls were

passivated with $SiO_2$ to reduce surface leakage currents. The spectral response of this device has been shown in Fig. 6.7(b), at 100mV of reverse bias, measured up to 220K. It shows that the 0% cutoff wavelength is 9.6μm and 10.5μm at 77K and 200K, respectively.

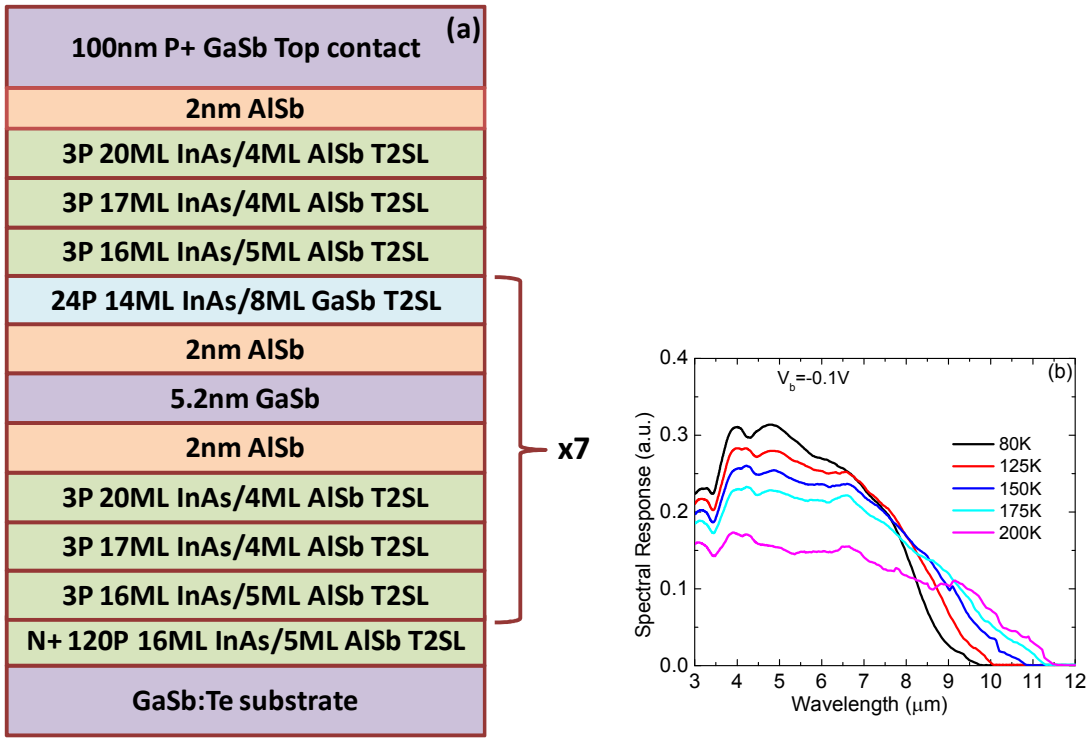


Fig. 6.7. (a) Schematic and (b) Spectral response data of LWIR interband cascade detector.

Fig. 6.8 (a) shows the dark current density plot at different temperature for LWIR cascade device. A dark current density of $3.0\times10^{-5}$A/cm$^2$ and $7.6\times10^{-3}$A/cm$^2$, at 80K and 150K at -10mV of applied bias. Fig. 6.8 (b) shows the Arrhenius plot of dark current density against inverse of the temperature. Activation energy of ~8meV in lower temperature range (50K-80K) suggests that the performance is limited by either surface leakage or tunneling phenomena. However, at higher temperature range (90-200K), activation energy of ~100meV is observed. From spectral response data, bandgap is 130meV and

118meV at 77K and 200K, respectively, suggesting that the origin of dark current is neither dominated by diffusion process nor by midgap SRH centers. This possibly indicates that the dominant dark current mechanism is the interband tunneling process, which takes place in the tunneling region. In that region, electrons from the conduction band combine with the holes in the quantized valence band state in GaSb well and the energy difference between the two states is close to 100meV.

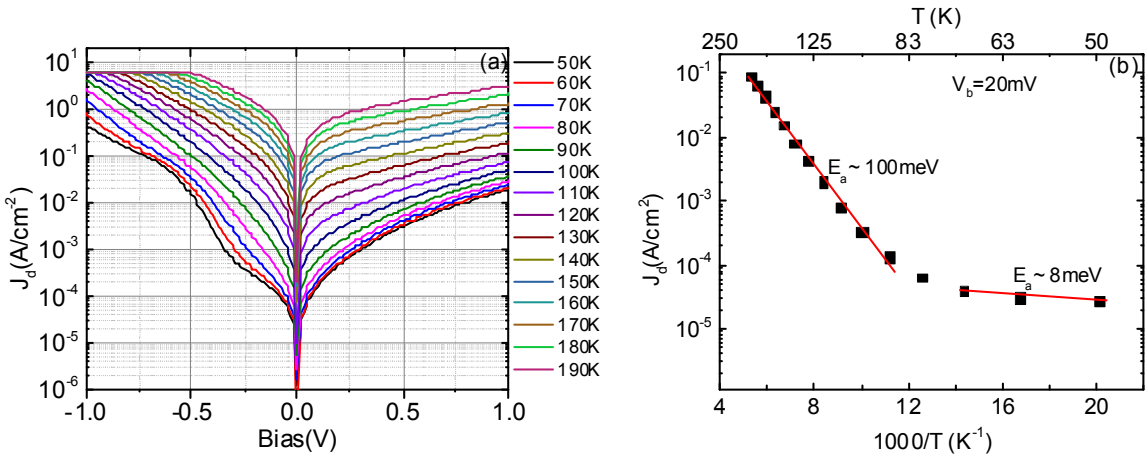


Fig. 6.8. (a) Dark current density and, (b) Arrhenius plot at 20mV of applied bias for LWIR cascade detector.

Radiometric characterization was carried out using a calibrated black body source at 900K and a long pass filter (LPF) to filter out the wavelengths shorter than 7.5μm. Measured responsivity, measured detectivity and calculated Johnson noise limited detectivity have been shown in Fig. 6.9 at 77K. We observed that the responsivity does not change much with applied bias, which indicates towards the efficient collection of photogenerated carriers. Peak responsivity of 0.35A/W was measured at 77K and -10mV of applied bias for λ=8.6μm. Using relationship between responsivity and gain-$\eta_i$ product, we obtained gain-$\eta_i$ product or conversion QE of 5.0%. Since, no absorption

measurements were carried out on this device, assuming a PC gain of 1/7, leads to a calculated absorption QE of 35%, which is a good estimate for a detector of 1μm absorber thickness. Measured peak detectivity, with 2πFOV and 300K background, of $7.1\times10^{9}$ cm-$Hz^{1/2}W^{-1}$ was observed at 77K and -10mV of applied bias.

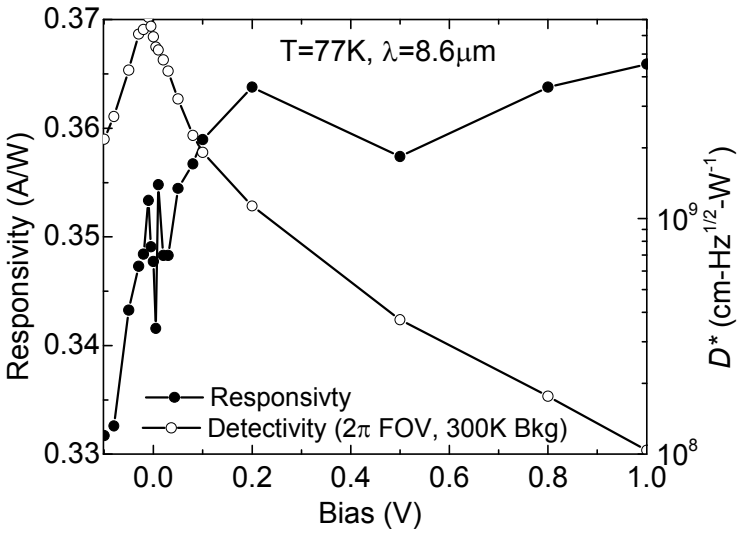


Fig. 6.9. Responsivity and detectivity measured at 2π FOV, 300K background at 77K.

In conclusion, we demonstrated high operating temperature performance of MWIR and LWIR T2SL interband cascade detectors. The flexibility of the antimonide system and the suitability of the EPM method for bandgap/bandoffset estimation of T2SLs were also demonstrated. The operating principle and dark current mechanisms of the detectors were discussed. While the MWIR detector demonstrated operation up to 420K, the LWIR detector worked up to 220K. The performance of these detectors can be further optimized by a careful study of absorber doping and optimization of tunneling and relaxation regions. A systematic study needs to be carried out for optimizing the doping and the composition of transport and tunneling regions.

# 7 Discussion and Future Directions

In this chapter, we will discuss the conclusions of this work and then highlight the important research areas in T2SL system that can further help in improving the performance of detectors and the physical understanding of the system.

## 7.1 Conclusions

The aim of this work was to realize high performance detectors based on the InAs/GaSb/AlSb T2SL system for MWIR and LWIR applications. The work was carried out at 'Material' and 'Device' level. In the 'Material' aspect of this work, bandstructure of T2SL was simulated using empirical pseudopotential method (EPM). The nature of quantum confined minibands was studied with the help of polarization dependent photocurrent spectroscopy measurements and supporting the results with theoretical simulations. The material growth of T2SL detector has been optimized to improve the performance, which involved optimization of interfaces. In the 'Device' aspect, 'Barrier Engineering' was used to design heterojunction detector architectures for performance improvement and operation at high temperature.

The bandstructure of T2SL has been modeled using EPM. Various superlattice systems such as InAs/GaSb T2SL, InAs/AlSb T2SL and GaSb/AlSb superlattice can be simulated using the codes developed as a part of this work, taking into account the strain effects. The simulation codes were also developed to evaluate optical matrix element for different inter-miniband transitions. However, exchange of atoms at the interfaces and the nature of interfacial bonds are not taken into account in this approach, as the simulations are not

atomistic. The codes can be easily extended to simulate superlattice consist of more than two components.

Material growth plays a significant role in dictating the performance of T2SL detector. Also, the performance of T2SL detectors, as explained in chapter 4, is dominated by SRH process. The origin of which can be at the interfaces. Since InAs/GaSb system has non-common cation and anion, the interfacial bonds can be either “InSb” type or “GaAs” type. For this purpose, the interfaces were optimized for T2SL detector using PL, and detector characteristic parameters such as dark current, responsivity and detectivity. A number of devices were grown, fabricated and characterized and it was concluded that supporting “InSb” type bonds at both the interfaces resulted in the best performance. This is achieved by using $Sb_2$ soak time on “GaSb on InAs” interface and growing InSb thin layer on “InAs on GaSb” interface. This also helps in strain balancing the system. This interface scheme has been subsequently used in the high performance LWIR pBiBn devices as well as the HOT MWIR cascade devices, giving lattice matched T2SL in these structures.

The nature of quantum confined miniband was studied, as described in chapter 4, using polarization dependent photocurrent spectroscopy. There had been no experimental study so far to clearly establish the ordering of valence minibands in T2SL system. The study was carried out on a MWIR as well as a LWIR sample. The experimental results were correlated with the theoretical simulations and it was concluded the order of valence minibands with increase in energy is HH1, LH1, LH2, and HH2.

High performance heterojunction detector architecture, denoted as pBiBn, has been conceptualized and realized in this work. As explained in chapter 5, it uses two unipolar barriers, with electron barrier (EB) layer sandwiched between P+ contact layer and absorber region and hole barrier (HB) layer sandwiched between the absorber and the N+ contact layer. For a given absorber region, once the bandoffsets and bandgaps of various layers are decided, the composition of InAs/GaSb/AlSb superlattice was obtained using EPM simulations. The first pBiBn LWIR design demonstrates more than two orders of magnitude improvement in the dark current over the conventional PIN detector. It also improved detectivity by a factor of four over PIN design. After optimization of barrier and doping in the absorber region, pBiBn Design 2 on LWIR detector demonstrated performance close to the state of the art in T2SL detectors with operation up to 200K. The MWIR pBiBn detector demonstrated operation at room temperature and a good signal to noise ratio till 200K, without any degradation in signal. While this thesis is being written, the fabrication of focal plane arrays (FPA) based on MWIR pBiBn and LWIR Design 2 is in progress.

The barrier engineering of antimonide system was carried out to realize multi-color detectors based on T2SL system. This work demonstrated the implementation of pBiBn architecture for a dual band LWIR/MWIR three contact device. Also, a three contact three color detector was realized where SWIR/MWIR/LWIR bands can be detected with simultaneous detection of either SWIR/LWIR or MWIR/LWIR bands. The limitation on three terminal multicolor devices is the unavailability of commercially available read out integrated circuits (ROICs). However, such ROICs are present in various laboratories for their proprietary use [93, 119].

Interband cascade detectors based on MWIR and LWIR T2SL absorbers were designed, grown, fabricated, and characterized. The interband cascade detectors are important for ultra low noise and hence HOT detection. Also the built-in gain adds to the advantage for HOT operation as described in chapter 6. The first unoptimized MWIR design demonstrated operation up to 420K. The reported cascade detector has seven stages with each stage consisting of an absorber region, relaxation or transport region and an interband tunneling region. Design aspects of the detector have been discussed in chapter 6. The photoconductive gain was calculated using absorption data and measured responsivity data. It was found to be 0.12, which close to the anticipatedvalue of 1/7. A LWIR cascade detector was also realized. The device operated up to 200K, and demonstrated an absorption quantum efficiency of 35% and dark current density $3.0\times10^{-5}$A/cm$^2$ at -10mV of applied bias and 77K.

## 7.2 Future Directions

This work has been focused on the material as well as device aspect of T2SL detectors. Though a significant progress was made in realizing high performance devices by carrying out optimization at both the fronts, there is still a scope for improvement. In this section we will go over the future work needed to be done at both “Material” and “Device” level.

### 7.2.1 Material

In this work, the interfaces of InAs/GaSb T2SL were optimized as described earlier. Another material aspect which is not very well understood is the incorporation of dopants inside the T2SL system. Because of the type-II alignment between InAs/GaSb and InAs/AlSb, it is possible that a donor atom in InAs can act as an acceptor in AlSb or GaSb. For doping InAs/GaSb T2SL, typically n-type dopant is put in InAs layer and p-

type in GaSb layer. The dependence of minority carrier lifetime on dopant density has been studied[120], but there is no conclusive statement about the incorporation of dopants in T2SL material. As has been discussed, the performance of T2SL detectors is dominated by SRH lifetime, the origin of which has not been known very well. It is a possibility that the donor or acceptor states can act as the generation-recombination centers. Hence it is important to investigate the energy of dopant level with respect to the conduction or valence band of T2SL. The optimal way of doping T2SL, by opening dopant shutter during InAs growth or GaSb growth or both, needs to be established as well. We suggest that a systematic study needs to be carried out for dopant incorporation. For each dopant type, a set of three samples should be grown as listed in Table 7.1. The characterization of dopant levels is then carried out using in-plane and vertical hall measurements, which can reveal carrier concentration dependence on the sequence of dopant shutter sequence during T2SL growth. Further, temperature dependent photoluminescence and time-resolved photoluminescence measurements should be carried out to study the impact of dopant and its type on the optical properties and carrier lifetimes of T2SL detectors. The effect of doping on detector performance needs to be studied as well. While optimizing the LWIR pBiBn detector Design 2, we grew two samples. These two samples were grown to optimize the p-type doping in the LWIR absorber region, keeping everything else identical. They were also grown back to back to avoid growth variations. The Design 2 reported in chapter 5 has the absorber region doped p- with Be such that the cell temperature of Be was adjusted to incorporate $1x10^{16}$ $cm^{-3}$ dopant concentration at the growth rates used for In and Ga. In Design 2, the Be shutter was kept open during all the layers of the absorber region. A variation of Design

2, which we call Design 3 here, was grown in which Be cell temperature was same as that used for Design 2 absorber doping but the dopant shutter was kept open only during the growth of GaSb layers of the absorber region. Apart from the changed dopant shutter sequence in the absorber region, all other layers were identical in Design 2 and 3. The characterization of both devices revealed that Design 2 had dark current density lower than that of Design 3 by more than an order of magnitude. Fig. 7.1 (a) and (b) show the Arrhenius plot of dark current of the two devices at their optimal bias of operation. It shows that the Design 2 was diffusion limited till 80K while Design 3 was diffusion limited till 110K only; here $T_0$ denoted the temperature beyond which dark current is diffusion limited. This indicates that doping in the absorber region is dictating the nature of dominant dark current mechanism. The responsivity data of the two designs has also been compared in Fig. 7.2 at $\lambda$=8.6μm. It shows that the Design 2 has better signal response and the responsivity is more than factor of two higher than that of the Design 3, which is consistent at all temperatures. This indicates that there is a very strong dependence of doping density on the device performance. The reason behind the device performance is not very well understood. One possibility is that the opening of Be shutter during all the layers resulted in higher p- doping concentration which improved the device performance. The other possibility is that the intrinsic n-type nature of InAs is compensated in Design 2 which led to the better performance. A further analysis is needed to explore the impact of doping concentration and its shutter sequence on detector performance. A combination of material study and device study for this purpose can lead to a very sound understanding of dopant incorporation and their impact on electronic as well as optical properties of T2SL.

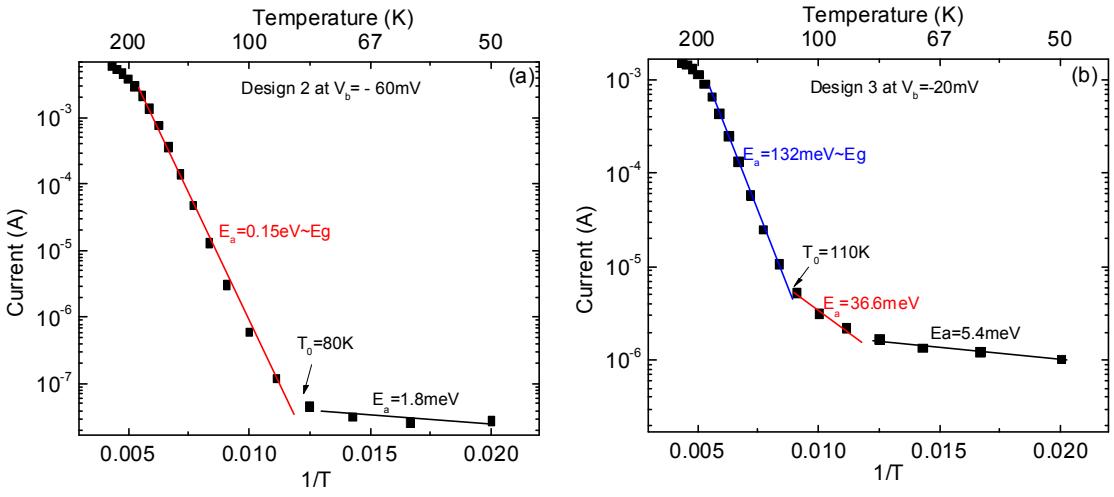


Fig. 7.1. Arrhenius plot of dark current against inverse of temperature for (a) Design 2 and (b) Design 3, at optimum bias showing the transition temperature beyond which dark current is dominated by diffusion process.

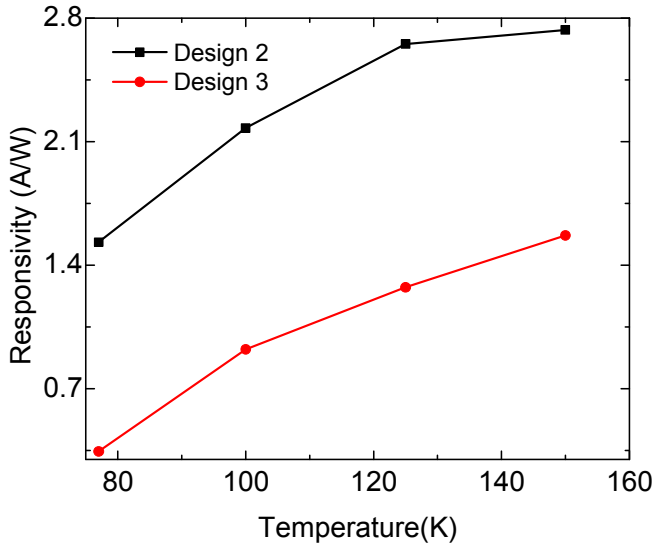


Fig. 7.2. Comparison of responsivity of Design 2 and 3 LWIR pBiBn photodiodes as a function of temperature at optimal bias of operation.

The bandstructure of T2SL was simulated in this work using EPM to obtain the E-k relationship as well as the wavefunctions for carriers in different bands. The simulations were further extended to evaluate the optical matrix element for transitions from valence

minibands to conduction minibands. Though the simulations codes work well for bandgap and bandoffset estimation for device designs, a lot of work is still needed to make them versatile. For example, density of states calculation for T2SL can be incorporated in the simulation codes and that would enable direct calculation of absorption coefficient. Comparison of calculated and measured absorption coefficient will be important in estimating some of the fundamental properties of T2SLs such as real and imaginary parts of permittivity.

### 7.2.2 Barrier Engineering

In this work we demonstrated higher performance T2SL detectors in both MWIR and LWIR range using barrier engineering. However, there is still a scope for improvement in the device designs. We will discuss the possible improvement in the pBiBn design and the cascades design in this section.

**pBiBn Design**

The performance of pBiBn detector for LWIR regime was optimized in this work with respect to the barrier. However, as motioned in the "Materials" section above, further work is needed to optimize the doping in the absorber region. This is related to the doping study that we described and it will affect the device performance as well. One important thing to keep in mind is that as the doping concentration is changed in the absorber region the EB and HB layers of pBiBn design needs to be modified in composition as well in order to allow a smooth path for holes and electrons, respectively. Else, this may results in a higher bias for operation.

We demonstrated a MWIR pBiBn detector. However, there is a scope for improving its performance by doping the absorber region and accordingly modifying the barrier layers. Given the device performance of the MWIR design reported in this work, its optimization can definitely lead to a performance comparable to the best HOT MWIR devices realized on T2SL system[121] and InAsSb system[90].

**Interband Cascade Detectors**

The interband cascade devices demonstrate HOT operation in both MWIR and LWIR regime, however the devices were the first designs and hence not optimized. A systematic study needs to be carried out to optimize the performance of cascade devices. For reference, the schematic of the cascade detector highlighting absorber, relaxation/transport and tunneling regions has been given in Fig. 7.3. Different fronts of cascade devices which need work have been bulleted below and we think that the optimization needs to be carried out in that order.

1. The superlattice composition of graded gap transport region can be changed from InAs/AlSb T2SL to InAs/AlInSb superlattice. This can provide design flexibility of transport region for different absorber compositions. There would be two degrees of freedom in changing the bandgap, one by changing thickness of individual layers of superlattice and the other by changing the composition of AlInSb layers.
2. The interband tunneling region should be optimized further. In the current design we used only one GaSb well surrounded by two barriers. A series of three samples can be designed with one, two and three wells, respectively, so that they

match the lowest conduction band energy of transport region with the valence band energy of the absorber region using LO phonons. Incorporation of more than one QW can lead to reduction in dark current but it remains to be seen if it decreases photocurrent as well. For this comparison, detectivity measurements should be carried out and then the optimal number of wells can be decided.

3. It was shown in chapter 6 that the performance of MWIR cascade detector was dominated by SRH process. That possibly indicates that the presence of depletion region in the absorber region. The reported devices in this work had a non-intentionally-doped (nid) absorber. However the MWIR cascade deice reported in[52] had absorber doped with n-type dopant. Usually, in case of photodiodes, the absorber region is doped p-type as electrons have favorable transport properties over holes. We think that a systematic study needs to be carried out by changing the type and concentration of dopant in the absorber region of cascade detector and performance of the devices should be compared.

**Dark Current Modeling**

The understanding of heterojunction device operation can be strengthened with a rigorous dark current modeling of the system. Such modeling can also help in designing high performance devices by identifying the dominant dark current mechanisms. Simulation of various dark current mechanisms and comparison of experimental data with simulated dark current can lead to an estimation of unknown parameters such as lifetime[122] or carrier mobilities or diffusion lengths, one of the physical properties if others are known from experiments. We propose that a self consistent system can be developed taking into material and device level measurements and combining them with theoretical modeling.

4. The photoconductive gain (PC Gain) can be calculated using responsivity and absorption measurements. It is a ratio of carrier lifetime and transit time.
5. Carrier lifetime can be measured experimentally [28] , which can be used with measured gain to estimate transit time.
6. A model developed for dark current simulation can be compared with experimental dark current data at different temperatures and across devices to obtain mobility, diffusion lengths and effective masses.

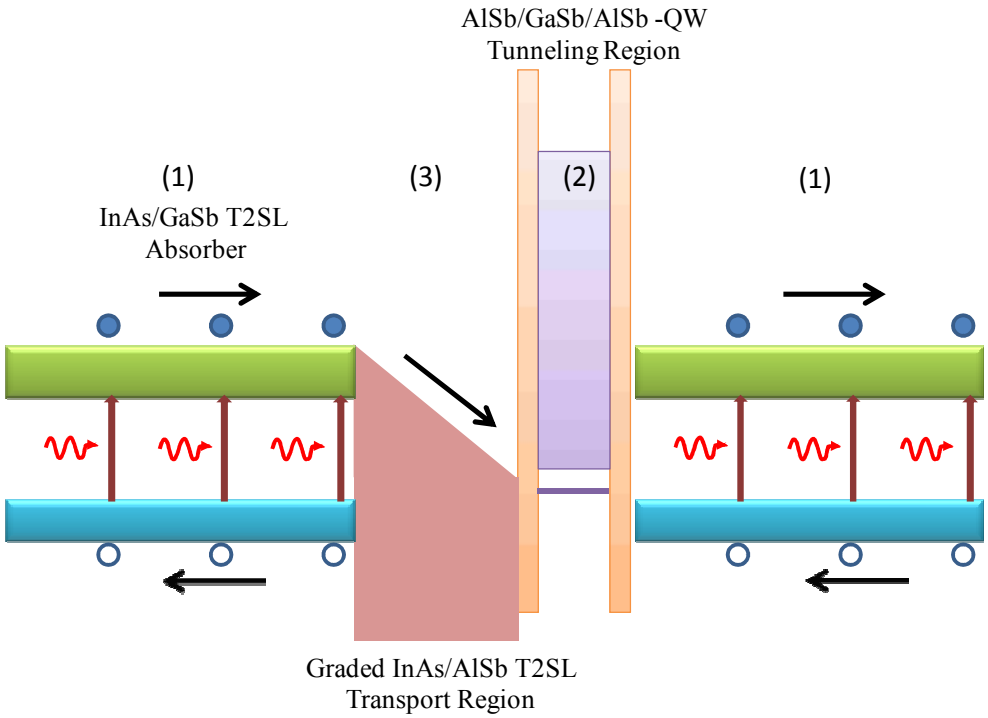


Fig. 7.3. Schematic of cascade device showing the absorber region, interband tunneling region and transport region.

**Barrier Avalanche Photodiodes**

The performance of T2SL detectors can also be improved by introducing novel heterojunction devices which increase photocurrent without affecting the dark current and

hence leading to an increased signal to noise ratio. In this work, such a concept was developed by combining unipolar barrier with avalanche multiplication region. The flat banddiagram of the proposed device is shown in Fig. 7.4 (a). It consists of MWIR 8ML InAs/8ML GaSb T2SL absorber layer. This device has only one unipolar barrier hole blocking layer made of 11ML InAs/5ML AlSb T2SL. The top contact layer is similar to the absorber region in composition while the bottom contact layer is made of wider bandgap 7ML InAs/6ML GaSb T2SL. The use of unipolar barrier for reducing dark currents has already been demonstrated in chapter 5. In the present device the HB layer not only reduces the dark current but also increases photocurrent by means of electron multiplication. Under reverse bias, we know that most of the field drops across the barrier layer from the simulations carried out on pBiBn devices. The E-k diagram of the HB layer is shown in Fig. 7.4(b), for k vector in plane of the superlattice ($k_{||}$). It shows that the energy separation between the consecutive conduction bands, C1 and C2, is comparable to the bandgap of 11ML InAs/5ML AlSb T2SL, while all the minibands in the valence band are energetically close to each other. This is called as resonance condition of conduction band[123, 124], which is absent in the valence band. As explained in [123], this can lead to a high electron initiated impact ionization coefficient, while a small probability of hole initiated ionization process. This would lead to reduced excess noise in the system, as impact ionization would be caused by only one type of carrier. Such HB layers, which predominantly support electron initiated impact ionization, and EB layer, which support hole initiated impact ionization, can be designed with by engineering the bandgap of InAs/GaSb/AlSb T2SL. Such a scheme, where a

unipolar barrier not only reduces dark current but also increases photocurrent can result high operating temperature devices.

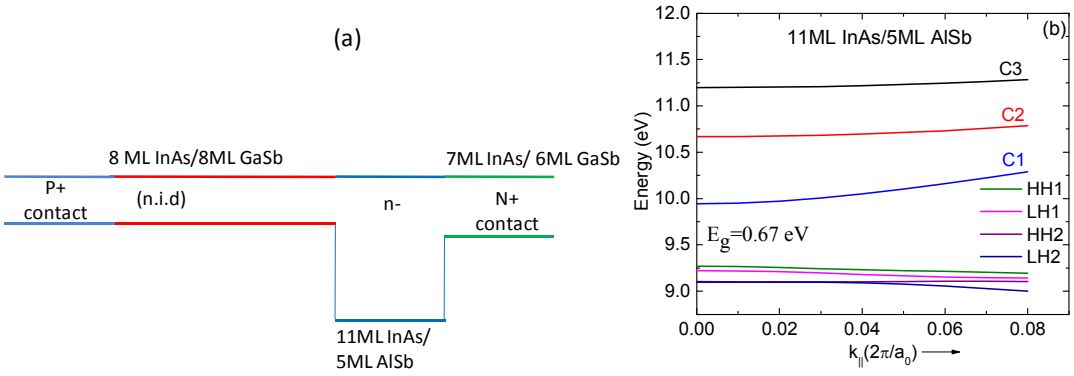


Fig. 7.4. (a) Heterojunction schematic of an avalanche unipolar barrier photodiode, (b) In plane E-k dispersion curve for 11ML InAs/5ML AlSb T2SL.

In conclusion, this work attempted realization of high performance detectors based on T2SL system by combining the physical properties with device engineering and using devices to understand the physical properties of the system. It was demonstrated that the interfaces of T2SL play an important role in dictating device performance and an optimal interface scheme was established. Quantum confined minibands and their ordering in valence band was investigated using photocurrent spectroscopy on MWIR and LWIR devices and comparing results with theoretical simulations. Barrier engineering was used extensively to design high performance LWIR devices, with performance comparable to the state of the art and HOT MWIR devices, with operation at 420K. Flexibility of tuning the bandgaps and bandoffsets of 6.1Å family was used for this purpose, where EPM was used to simulate the bandstructure. There is still a huge scope of improvement in T2SL devices by the use of doping optimization, barrier engineering and novel device designs. This work contributed towards using the physical properties of the InAs/GaSb/AlSb

T2SL system for the purpose of realizing high performance engineered devices and using the device results to improve the understanding of physical properties. Hopefully, this work is a step closer towards replacing the incumbent MCT technology with InAs/GaSb T2SL technology!

# Appendix A: Growth

The growth recipe for LWIR pBiBn Deisgn 2 heterostructure has been provided in this appendix. The sample was grown on 2" GaSb:Te substrate. Before the actual detector structure growth, a couple of calibration samples were grown to figure out the amount of InSb and $Sb_2$ soak times needed at the interfaces for strain balancing. The structure is shown below with shutter opening times during one period of the absorber T2SL. Similar shuttering scheme has been used in all the T2SLs, with appropriate InSb thickness and $Sb_2$ soak time, except in 7ML GaSb/ 3.5ML AlSb superlattice where no compensation is used, but thickness of AlSb in each period is much smaller than critical thickness on GaSb.

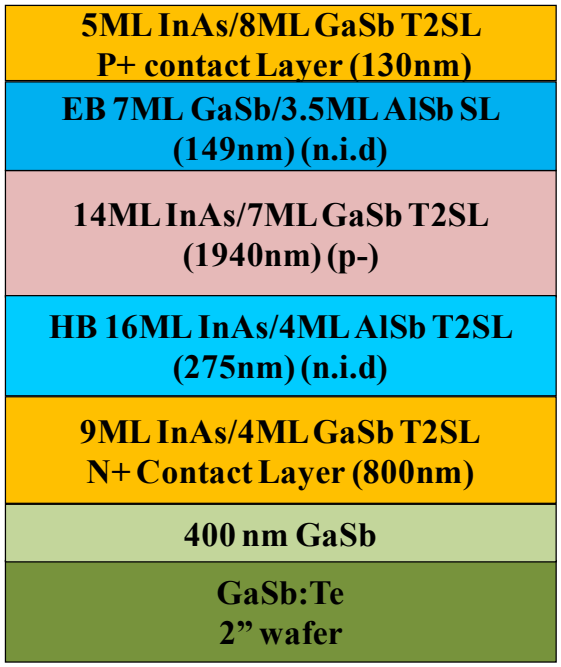


**Design 2 Schematic**

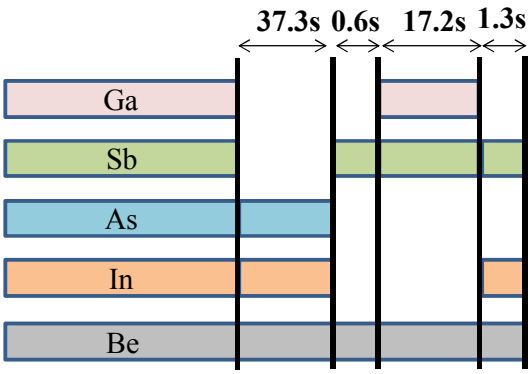


**Shutter times of sources for one period of the absorber region**

Growth rates and dopant incorporation:

For this growth, R_In=0.375 monolayers(ML)/s, R_Ga=0.407ML/s and R_Al=0.403ML/s were used, where R_In, R_Ga and R_Al are growth rates of Ga, In and Al sources. A beam equivalent pressure (BEP) ratio of 9.2 and 3.9 were used for As/In and Sb/Ga, respectively. As shown in the schematic of the detector, the N+ bottom contact layer is made of 9ML InAs/4ML GaSb T2SL and GaTe was used as n-type dopant. GaTe was only incorporated in the InAs layer of T2SL such that at the used growth rate of In, the resulting dopant incorporation is $3x10^{18}cm^{-3}$. Similarly for the top contact layer, p-type dopant, Be, was incorporated only in the GaSb layers of 5ML InAs/8ML GaSb T2SL. In this structure, the absorber is doped p- to a level of $1x10^{16}cm^{-3}$ with Be such that the Be shutter was kept open during all the layers including the strain balancing ones.

Stepwise growth sequence is given below:

1. The loaded wafer was pre-heated to a temperature of 365ºC inside the preparation chamber to get rid of water content and other impurities on substrate surface.
2. Before transferring the wafer inside the growth chamber, flux measurements were carried out to determine valve opening for As cracker source and base power to Sb cracker source which was not a valved one. Flux measurements should always be carried out in one source sequence as resulting flux also depends on the history. Also, one much wait 5-6 minutes before recording $As_2$ flux as it takes time for stabilizing.

3. Once wafer is loaded inside the chamber, it was heated till 370ºC and then temperature of the substrate was increased to 635ºC (on pyrometer) under $Sb_2$ flux because at higher temperatures Sb starts to come off the surface of GaSb and hence a continuous source of $Sb_2$ is needed.
4. Between 635-650ºC, native oxide on the wafer started to come off and this can been seen with a spotty RHEED pattern which eventually turned into streaky one as oxide was completely removed.
5. Once oxide desorption was completed, the temperature of wafer was lowered to 490 ºC to start growth of the buffer layer or smoothing layer of GaSb with a thickness of 400-500nm.
6. After buffer layer growth, the substrate temperature was further lowered under $Sb_2$ flux, and RHEED was observed to monitor the transition temperature ($T_t$) at which the GaSb RHEED pattern changes from (1x3) to (5x2). Since the pyrometer used in V80H chamber cannot read temperatures lower than 440ºC, transition temperature[80] is used to decide the growth temperature. It is to be noted that $T_t$ is also a function of $Sb_2$ flux[80]; hence it should be taken into consideration if $Sb_2$ flux changes.
7. For detector structure growth, the substrate temperature was adjusted to $T_t$-30ºC. Once the temperature was reached, a labview program which controls all the shutters was started to proceed with the detector growth.

# Appendix B: Parameters for Empirical Pseudopotential Method

This appendix provides list of all the bulk parameters used for the simulation of InAs/GaSb/AlSb superlattice bandstructure. Form factors and other parameters are used in empirical pseudopotential formalism to get bandstructure of bulk materials and these parameters are used to simulate bandstructure of T2SL. Values of form factors and parameter Γ, defined in chapter 3, have been tabulated below for InAs, GaSb and AlSb. $V_S(|\mathbf{q}|^2)$ and $V_A(|\mathbf{q}|^2)$ denote symmetric and anti-symmetric form factors and the term in parenthesis is magnitude square of $\mathbf{q}$ defined as $\mathbf{q=G'-G}$, in chapter 3. The form factors have been given in units of Rydberg constant which is equal to 13.605eV. The form factor $V_S(0)$ does not have any impact on bandstructure and is solely used to control bandoffsets between different materials.

| Parameters | InAs | GaSb | AlSb |
|---|---|---|---|
| $V_S(0)$ | 0.008 | 0.00 | 0.0362 |
| $V_S(3)$ | -0.266 | -0.249 | -0.2456 |
| $V_A(3)$ | 0.07 | 0.038 | 0.071 |
| $V_A(4)$ | 0.038 | 0.004 | 0.00 |
| $V_S(8)$ | 0.01923 | 0.05 | 0.0167 |
| $V_S(11)$ | 0.047 | 0.032 | 0.094 |
| $V_A(11)$ | 0.01 | 0.035 | 0.00 |
| Γ | 3450 | 13300 | 9700 |

List of parameters used in empirical pseudopotential calculations

# References


[1] E. L. Dereniak and G. D. Boreman, *Infrared Detectors and Systems*: John Wiley & Sons, 1996.

[2] A. Rogalski, "Infrared detectors: an overview," *Infrared Physics & Technology,* vol. 43, pp. 187-210, 2002.

[3] A. Rogalski, "Infrared detectors: status and trends," *Progress in Quantum Electronics,* vol. 27, pp. 59-210, 2003.

[4] B. F. Levine, "Quantum-well infrared photodetectors," *Journal of Applied Physics,* vol. 74, pp. R1-R81, 1993.

[5] H. C. Liu, J. Y. Duboz, R. Dudek, Z. R. Wasilewski, S. Fafard, and P. Finnie, "Quantum dot infrared photodetectors," *Physica E: Low-dimensional Systems and Nanostructures,* vol. 17, pp. 631-633, 2003.

[6] A. V. Barve, S. J. Lee, S. K. Noh, and S. Krishna, "Review of current progress in quantum dot infrared photodetectors," *Laser & Photonics Reviews,* vol. 4, pp. 738-750, 2010.

[7] A. Rogalski, "Quantum well photoconductors in infrared detector technology," *Journal of Applied Physics,* vol. 93, pp. 4355-4391, 2003.

[8] W. D. Lawson, S. Nielsen, E. H. Putley, and A. S. Young, "Preparation and properties of HgTe and mixed crystals of HgTe-CdTe," *Journal of Physics and Chemistry of Solids,* vol. 9, pp. 325-329, 1959.

[9] L. Esaki and R. Tsu, "Superlattice and Negative Differential Conductivity in Semiconductors," *IBM Journal of Research and Development,* vol. 14, pp. 61-65, 1970.

[10] G. A. Sai-Halasz, R. Tsu, and L. Esaki, "A new semiconductor superlattice," *Applied Physics Letters,* vol. 30, pp. 651-653, 1977.

[11] D. L. Smith and C. Mailhiot, "Proposal for strained type II superlattice infrared detectors," *Journal of Applied Physics,* vol. 62, pp. 2545-2548, 1987.

[12] D. Z. Y. Ting, A. Soibel, L. Höglund, J. Nguyen, C. J. Hill, A. Khoshakhlagh, and S. D. Gunapala, "Chapter 1 - Type-II Superlattice Infrared Detectors," in *Semiconductors and Semimetals*. vol. Volume 84, D. R. R. Sarath D. Gunapala and J. Chennupati, Eds., ed: Elsevier, 2011, pp. 1-57.

[13] C. H. Grein, P. M. Young, and H. Ehrenreich, "Minority carrier lifetimes in ideal InGaSb/InAs superlattices," *Applied Physics Letters,* vol. 61, pp. 2905-2907, 1992.

[14] E. R. Youngdale, J. R. Meyer, C. A. Hoffman, F. J. Bartoli, C. H. Grein, P. M. Young, H. Ehrenreich, R. H. Miles, and D. H. Chow, "Auger lifetime enhancement in InAs--Ga[sub 1 - x]In[sub x]Sb superlattices," *Applied Physics Letters,* vol. 64, pp. 3160-3162, 1994.

[15] A. Rogalski, "Recent progress in infrared detector technologies," *Infrared Physics & Technology,* vol. 54, pp. 136-154, 2011.

[16] A. Rogalski, "Third-generation infrared photon detectors," *Optical Engineering,* vol. 42, pp. 3498-3516, 2003.

[17] A. Rogalski and P. Martyniuk, "InAs/GaInSb superlattices as a promising material system for third generation infrared detectors," *Infrared Physics & Technology,* vol. 48, pp. 39-52, 2006.

[18] H. Kroemer, "The 6.1 Å family (InAs, GaSb, AlSb) and its heterostructures: a selective review," *Physica E: Low-dimensional Systems and Nanostructures,* vol. 20, pp. 196-203, 2004.

[19] M. Walther, R. Rehm, F. Fuchs, J. Schmitz, J. Fleißner, W. Cabanski, D. Eich, M. Finck, W. Rode, J. Wendler, R. Wollrab, and J. Ziegler, "256×256 focal plane array midwavelength infrared camera based on InAs/GaSb short-period superlattices," *Journal of Electronic Materials,* vol. 34, pp. 722-725, 2005.

[20] E. H. Aifer, J. G. Tischler, J. H. Warner, I. Vurgaftman, W. W. Bewley, J. R. Meyer, J. C. Kim, L. J. Whitman, C. L. Canedy, and E. M. Jackson, "W-structured type-II superlattice long-wave infrared photodiodes with high quantum efficiency," *Applied Physics Letters,* vol. 89, p. 053519, 2006.

[21] B.-M. Nguyen, D. Hoffman, P.-Y. Delaunay, and M. Razeghi, "Dark current suppression in type II InAs/GaSb superlattice long wavelength infrared photodiodes with M-structure barrier," *Applied Physics Letters,* vol. 91, p. 163511, 2007.

[22] D. Z.-Y. Ting, C. J. Hill, A. Soibel, S. A. Keo, J. M. Mumolo, J. Nguyen, and S. D. Gunapala, "A high-performance long wavelength superlattice complementary barrier infrared detector," *Applied Physics Letters,* vol. 95, p. 023508, 2009.

[23] N. Gautam, H. S. Kim, M. N. Kutty, E. Plis, L. R. Dawson, and S. Krishna, "Performance improvement of longwave infrared photodetector based on type-II InAs/GaSb superlattices using unipolar current blocking layers," *Applied Physics Letters,* vol. 96, p. 231107, 2010.

[24] P. Manurkar, S. Ramezani-Darvish, B.-M. Nguyen, M. Razeghi, and J. Hubbs, "High performance long wavelength infrared mega-pixel focal plane array based on type-II superlattices," *Applied Physics Letters,* vol. 97, p. 193505, 2010.

[25] S. D. Gunapala, D. Z. Ting, C. J. Hill, J. Nguyen, A. Soibel, S. B. Rafol, S. A. Keo, J. M. Mumolo, M. C. Lee, J. K. Liu, B. Yang, and A. Liao, "Demonstration of 1Kx1K long-wave and mid-wave superlattice infrared focal plane arrays," 2010, p. 780802.

[26] B. C. Connelly, G. D. Metcalfe, H. Shen, and M. Wraback, "Direct minority carrier lifetime measurements and recombination mechanisms in long-wave infrared type II superlattices using time-resolved photoluminescence," *Applied Physics Letters,* vol. 97, p. 251117, 2010.

[27] D. Donetsky, S. P. Svensson, L. E. Vorobjev, and G. Belenky, "Carrier lifetime measurements in short-period InAs/GaSb strained-layer superlattice structures," *Applied Physics Letters,* vol. 95, p. 212104, 2009.

[28] D. Donetsky, G. Belenky, S. Svensson, and S. Suchalkin, "Minority carrier lifetime in type-2 InAs--GaSb strained-layer superlattices and bulk HgCdTe materials," *Applied Physics Letters,* vol. 97, p. 052108, 2010.

[29] S. Chih-Tang, R. N. Noyce, and W. Shockley, "Carrier Generation and Recombination in P-N Junctions and P-N Junction Characteristics," *Proceedings of the IRE,* vol. 45, pp. 1228-1243, 1957.

[30] W. H. Lau and M. E. Flatte, "Effect of interface structure on the optical properties of InAs/GaSb laser active regions," *Applied Physics Letters,* vol. 80, pp. 1683-1685, 2002.

[31] H. J. Haugan, G. J. Brown, and L. Grazulis, "Effect of interfacial formation on the properties of very long wavelength infrared InAs/GaSb superlattices," 2011, p. 03C101.

[32] J. Steinshnider, M. Weimer, R. Kaspi, and G. W. Turner, "Visualizing Interfacial Structure at Non-Common-Atom Heterojunctions with Cross-Sectional Scanning Tunneling Microscopy," *Physical Review Letters,* vol. 85, p. 2953, 2000.

[33] M. Debbichi, S. B. Rejeb, L. Debbichi, and M. Said, "Interfaces as design tools for the InAs/GaSb/InSb short-period superlattice for mid-infrared emission," *Semiconductor Science and Technology,* vol. 26, p. 095010, 2011.

[34] J. B. Rodriguez, P. Christol, L. Cerutti, F. Chevrier, and A. Joullié, "MBE growth and characterization of type-II InAs/GaSb superlattices for mid-infrared detection," *Journal of Crystal Growth,* vol. 274, pp. 6-13, 2005.

[35] A. Khoshakhlagh, S. Myers, K. HaSul, E. Plis, N. Gautam, L. Sang Jun, S. K. Noh, L. R. Dawson, and S. Krishna, "Long-Wave InAs/GaSb Superlattice Detectors Based on nBn and Pin Designs," *Quantum Electronics, IEEE Journal of,* vol. 46, pp. 959-964, 2010.

[36] E. A. Plis, S. S. Krishna, N. Gautam, S. Myers, and S. Krishna, "Bias Switchable Dual-Band InAs/GaSb Superlattice Detector With pBp Architecture," *Photonics Journal, IEEE,* vol. 3, pp. 234-240, 2011.

[37] G. C. Dente and M. L. Tilton, "Pseudopotential methods for superlattices: Applications to mid-infrared semiconductor lasers," *Journal of Applied Physics,* vol. 86, pp. 1420-1429, 1999.

[38] G. Biasiol and L. Sorba, "Molecular beam epitaxy: principles and applications," in *Crystal Growth of Materials for Energy Production and Energy-Saving Applications*, R. Fornari and L. Sorba, Eds., ed Pisa, Italy: ETS, 2001, pp. 66 -83.

[39] M. J. Furlong, R. Martinez, S. Amirhaghi, and B. Smith, "Antimonide based infrared materials: Developments in InSb and GaSb substrate technologies," in *Indium Phosphide & Related Materials (IPRM), 2010 International Conference on*, 2010, pp. 1-5.

[40] M. A. Herman and H. Sitter, *Molecular beam epitaxy—fundamentals and current status.* : Springer-Verlag 1989.

[41] H. S. Kim, "Investigation of InAs/GaSb superlattice based nBn detectors and focal plane arrays," Doctoral, Dept. of Electrical and Computer Engineering, University of New Mexico, 2010.

[42] E. A. Plis, M. N. Kutty, and S. Krishna, "Passivation techniques for InAs/GaSb strained layer superlattice detectors," *Laser & Photonics Reviews,* pp. n/a-n/a, 2012.

[43] H. S. Kim, E. Plis, N. Gautam, S. Myers, Y. Sharma, L. R. Dawson, and S. Krishna, "Reduction of surface leakage current in InAs/GaSb strained layer long wavelength superlattice detectors using SU-8 passivation," *Applied Physics Letters,* vol. 97, p. 143512, 2010.

[44] S. Perkowitz, *Optical Characterization of Semiconductors: Infrared, Raman, and Photoluminescence Spectroscopy*: Academic Press, 1993.

[45] D. K. Bowen and B. K. Tanner, *X-Ray Metrology in Semiconductor Manufacturing*: CRC Press, 2006.
[46] K. Matney, "PeakSplit," 2.8.2 ed, 1998.
[47] A. Soibel, D. Z.-Y. Ting, C. J. Hill, M. Lee, J. Nguyen, S. A. Keo, J. M. Mumolo, and S. D. Gunapala, "Gain and noise of high-performance long wavelength superlattice infrared detectors," *Applied Physics Letters,* vol. 96, p. 111102, 2010.
[48] N. Gautam, M. Naydenkov, S. Myers, A. V. Barve, E. Plis, T. Rotter, L. R. Dawson, and S. Krishna, "Three color infrared detector using InAs/GaSb superlattices with unipolar barriers," *Applied Physics Letters,* vol. 98, p. 121106, 2011.
[49] J. B. Rodriguez, E. Plis, G. Bishop, Y. D. Sharma, H. Kim, L. R. Dawson, and S. Krishna, "nBn structure based on InAs/GaSb type-II strained layer superlattices," *Applied Physics Letters,* vol. 91, pp. 043514-2, 2007.
[50] A. M. Hoang, G. Chen, A. Haddadi, S. A. Pour, and M. Razeghi, "Demonstration of shortwavelength infrared photodiodes based on type-II InAs/GaSb/AlSb superlattices," *Applied Physics Letters,* vol. 100, p. 211101, 2012.
[51] C. L. Canedy, E. H. Aifer, J. H. Warner, I. Vurgaftman, E. M. Jackson, J. G. Tischler, S. P. Powell, K. Olver, J. R. Meyer, and W. E. Tennant, "Controlling dark current in type-II superlattice photodiodes," *Infrared Physics & Technology,* vol. 52, pp. 326-334, 2009.
[52] Z. Tian, R. T. Hinkey, R. Q. Yang, D. Lubyshev, Y. Qiu, J. M. Fastenau, W. K. Liu, and M. B. Johnson, "Interband cascade infrared photodetectors with enhanced electron barriers and p-type superlattice absorbers," *Journal of Applied Physics,* vol. 111, p. 024510, 2012.
[53] Synopsis. SENTAURUS device user guide [Online]. Available: http://www.synopsys.com/TOOLS/TCAD/Pages/default.aspx
[54] S. Birner, "InAs / In0.4Ga0.6Sb superlattice dispersion with 8x8 k.p," ed. Germany: Nextnano, 2004.
[55] C. H. Grein, W. H. Lau, T. L. Harbert, and M. E. Flatte, "Modeling of very long infrared wavelength InAs/GaInSb strained layer superlattice detectors," 2002, pp. 39-43.
[56] N. F. Johnson, H. Ehrenreich, P. M. Hui, and P. M. Young, "Electronic and optical properties of III-V and II-VI semiconductor superlattices," *Physical Review B,* vol. 41, pp. 3655-3669, 1990.
[57] R. Magri and A. Zunger, "Effects of interfacial atomic segregation on optical properties of InAs/GaSb superlattices," *Physical Review B,* vol. 64, p. 081305, 2001.
[58] S. Abdollahi Pour, B. Movaghar, and M. Razeghi, "Tight-binding theory for the thermal evolution of optical band gaps in semiconductors and superlattices," *Physical Review B,* vol. 83, p. 115331, 2011.
[59] G. C. Dente and M. L. Tilton, "Comparing pseudopotential predictions for InAs/GaSb superlattices," *Physical Review B,* vol. 66, p. 165307, 2002.
[60] P. Y. Yu and M. Cardona, *Fundamentals of Semiconductors*, 4th ed.: Springer-Verlag, 2010.

[61] P. Harrison, *Quantum Wells, Wires and Dots: Theoretical and Computational Physics of Semiconductor Nanostructures*, 2nd ed.: JOHN WILEY & SONS, 2005

[62] P. Y. Yu and M. Cordona, *Fundamentals of Semiconductors*

*Physics and Materials Properties*, 4th ed.: Springer, 2010.

[63] Q. Yang, C. Pfahler, J. Schmitz, W. Pletschen, and F. Fuchs, "Trap centers and minority carrier lifetimes in InAs/(GaIn)Sb superlattice long wavelength photodetectors," 2003, pp. 448-456.

[64] C. Cervera, J. B. Rodriguez, J. P. Perez, H. Ait-Kaci, R. Chaghi, L. Konczewicz, S. Contreras, and P. Christol, "Unambiguous determination of carrier concentration and mobility for InAs/GaSb superlattice photodiode optimization," *Journal of Applied Physics,* vol. 106, p. 033709, 2009.

[65] P. Christol, C. Cervera, R. Chaghi, H. Ait-Kaci, J. B. Rodriguez, L. Konczewicz, S. Contreras, K. Jaworowicz, and I. Ribet-Mohamed, "Electronic properties of InAs/GaSb superlattice detectors to evaluate high-temperature operation," 2010, p. 76081U.

[66] A. Khoshakhlagh, F. Jaeckel, C. Hains, J. B. Rodriguez, L. R. Dawson, K. Malloy, and S. Krishna, "Background carrier concentration in midwave and longwave InAs/GaSb type II superlattices on GaAs substrate," *Applied Physics Letters,* vol. 97, p. 051109, 2010.

[67] H. Ehrenreich, M. E. Flatte, and C. H. Grein, "Superlattice IR detectors: a theoretical view," San Jose, CA, USA, 1996, pp. 48-61.

[68] K. Kim, P. R. C. Kent, A. Zunger, and C. B. Geller, "Atomistic description of the electronic structure of In_{x}Ga_{1-x}As alloys and InAs/GaAs superlattices," *Physical Review B,* vol. 66, p. 045208, 2002.

[69] R. Magri and A. Zunger, "Predicting interband transition energies for InAs/GaSb superlattices using the empirical pseudopotential method," *Physical Review B,* vol. 68, p. 155329, 2003.

[70] P. Voisin, G. Bastard, and M. Voos, "Optical selection rules in superlattices in the envelope-function approximation," *Physical Review B,* vol. 29, p. 935, 1984.

[71] auml, K. A. der, and A. Zunger, "Empirical atomic pseudopotentials for AlAs/GaAs superlattices, alloys, and nanostructures," *Physical Review B,* vol. 50, p. 17393, 1994.

[72] L. L. Li, W. Xu, and F. M. Peeters, "Intrinsic optical anisotropy of [001]-grown short-period InAs/GaSb superlattices," *Physical Review B,* vol. 82, p. 235422, 2010.

[73] P.-F. Qiao, S. Mou, and S. L. Chuang, "Electronic band structures and optical properties of type-II superlattice photodetectors with interfacial effect," *Opt. Express,* vol. 20, pp. 2319-2334, 2012.

[74] M. E. Flatte, J. T. Olesberg, S. A. Anson, T. F. Boggess, T. C. Hasenberg, R. H. Miles, and C. H. Grein, "Theoretical performance of mid-infrared broken-gap multilayer superlattice lasers," *Applied Physics Letters,* vol. 70, pp. 3212-3214, 1997.

[75] C. H. Grein, H. Cruz, M. E. Flatte, and H. Ehrenreich, "Theoretical performance of very long wavelength InAs/In[sub x]Ga[sub 1 - x]Sb superlattice based infrared detectors," *Applied Physics Letters,* vol. 65, pp. 2530-2532, 1994.

[76] C. H. Grein, M. E. Flatte, J. T. Olesberg, S. A. Anson, L. Zhang, and T. F. Boggess, "Auger recombination in narrow-gap semiconductor superlattices incorporating antimony," *Journal of Applied Physics,* vol. 92, pp. 7311-7316, 2002.

[77] M. R. Kitchin and et al., "Models of GaSb/InAs type-II infrared detectors at very long wavelengths: band offsets and interface bonds," *Semiconductor Science and Technology,* vol. 18, p. 225, 2003.

[78] F. Szmulowicz, S. Elhamri, H. J. Haugan, G. J. Brown, and W. C. Mitchel, "Demonstration of interface-scattering-limited electron mobilities in InAs/GaSb superlattices," *Journal of Applied Physics,* vol. 101, p. 043706, 2007.

[79] H. J. Haugan, G. J. Brown, and L. Grazulis, "Effect of interfacial formation on the properties of very long wavelength infrared InAs/GaSb superlattices," 2011, p. 03C101.

[80] A. S. Bracker, M. J. Yang, B. R. Bennett, J. C. Culbertson, and W. J. Moore, "Surface reconstruction phase diagrams for InAs, AlSb, and GaSb," *Journal of Crystal Growth,* vol. 220, pp. 384-392, 2000.

[81] R. K. Ahrenkiel, "Chapter 2 Minority-Carrier Lifetime in III–V Semiconductors," in *Semiconductors and Semimetals*. vol. Volume 39, K. A. Richard and S. L. Mark, Eds., ed: Elsevier, 1993, pp. 39-150.

[82] E. A. Plis, "Mid-IR type-II InAs/GaSb nanoscale supperlattice sensors," Ph. D., Department of Electrical and Computer Engineering, University of New Mexico, Albuquerque, 2007.

[83] J. Hernando, J. L. Sanchez-Rojas, A. Guzman, E. Munoz, J. M. G. Tijero, D. Gonzalez, G. Aragon, and R. Garcia, "Effect of indium content on the normal-incident photoresponse of InGaAs/GaAs quantum-well infrared photodetectors," *Applied Physics Letters,* vol. 78, pp. 2390-2392, 2001.

[84] J. Singh, *Electronic and Optoelectronic Properties of Semiconductor Structures*: Cambridge University Press.

[85] S. L. Chuang, *Physics of Photonic Devices*. Hoboken, New Jersey: Wiley Publishing, 2009.

[86] G. Bastard, *Wave Mechanics Applied to Semiconductor Heterostructures* Les Ulis, France.

[87] E. H. Aifer, S. I. Maximenko, M. K. Yakes, C. Yi, C. L. Canedy, I. Vurgaftman, E. M. Jackson, J. A. Nolde, C. A. Affouda, M. Gonzalez, J. R. Meyer, K. P. Clark, and P. R. Pinsukanjana, "Recent developments in type-II superlattice-based infrared detectors," 2010, p. 76601Q.

[88] S. D. Gunapala, D. Z. Ting, C. J. Hill, J. Nguyen, A. Soibel, S. B. Rafol, S. A. Keo, J. M. Mumolo, M. C. Lee, J. K. Liu, B. Yang, and A. Liao, "Demonstration of 1Kx1K long-wave and mid-wave superlattice infrared focal plane arrays," 2010, p. 780802.

[89] M. Razeghi, S. Abdollahi Pour, E. Huang, G. Chen, A. Haddadi, and B. Nguyen, "Type-II InAs/GaSb photodiodes and focal plane arrays aimed at high operating temperatures," *Opto-Electronics Review,* vol. 19, pp. 261-269, 2011.

[90] P. Klipstein, O. Klin, S. Grossman, N. Snapi, I. Lukomsky, M. Yassen, D. Aronov, E. Berkowitz, A. Glozman, O. Magen, I. Shtrichman, R. Frenkel, and E.

Weiss, "High operating temperature XBn-InAsSb bariode detectors," 2012, p. 82680U.

[91] W. Cabanski, R. Breiter, R. Koch, W. Gross, K. H. Mauk, W. Rode, J. Ziegler, H. Schneider, M. Walther, and R. Oelmaier, "Third gen focal plane array IR detection modules at AIM," *Infrared Physics & Technology,* vol. 43, pp. 257-263, 2002.

[92] H. Schneider, T. Maier, J. Fleissner, M. Walther, P. Koidl, G. Weimann, W. Cabanski, M. Finck, P. Menger, W. Rode, and J. Ziegler, "Dual-band QWIP focal plane array for the second and third atmospheric windows," *Infrared Physics & Technology,* vol. 47, pp. 53-58, 2005.

[93] R. Rehm, M. Walther, J. Fleissner, J. Schmitz, J. Ziegler, W. Cabanski, and R. Breiter, "Bispectral thermal imaging with quantum-well infrared photodetectors and InAs/GaSb type-II superlattices," Orlando (Kissimmee), FL, USA, 2006, pp. 62060Y-11.

[94] A. Khoshakhlagh, J. B. Rodriguez, E. Plis, G. D. Bishop, Y. D. Sharma, H. S. Kim, L. R. Dawson, and S. Krishna, "Bias dependent dual band response from InAs/Ga(In)Sb type II strain layer superlattice detectors," *Applied Physics Letters,* vol. 91, p. 263504, 2007.

[95] P.-Y. Delaunay, B.-M. Nguyen, D. Hoffman, A. Hood, E. K.-W. Huang, M. Razeghi, and M. Z. Tidrow, "High quantum efficiency two color type-II InAs/GaSb n-i-p-p-i-n photodiodes," *Applied Physics Letters,* vol. 92, p. 111112, 2008.

[96] E. K.-w. Huang and M. Razeghi, "World's first demonstration of type-II superlattice dual band 640x512 LWIR focal plane array," 2012, p. 82680Z.

[97] Q. K. Yang, F. Fuchs, J. Schmitz, and W. Pletschen, "Investigation of trap-assisted tunneling current in InAs/(GaIn)Sb superlattice long-wavelength photodiodes," *Applied Physics Letters,* vol. 81, pp. 4757-4759, 2002.

[98] J. L. Johnson, L. A. Samoska, A. C. Gossard, J. L. Merz, M. D. Jack, G. R. Chapman, B. A. Baumgratz, K. Kosai, and S. M. Johnson, "Electrical and optical properties of infrared photodiodes using the InAs/Ga[sub 1 - x]In[sub x]Sb superlattice in heterojunctions with GaSb," *Journal of Applied Physics,* vol. 80, pp. 1116-1127, 1996.

[99] I. Vurgaftman, E. H. Aifer, C. L. Canedy, J. G. Tischler, J. R. Meyer, J. H. Warner, E. M. Jackson, G. Hildebrandt, and G. J. Sullivan, "Graded band gap for dark-current suppression in long-wave infrared W-structured type-II superlattice photodiodes," *Applied Physics Letters,* vol. 89, p. 121114, 2006.

[100] P.-Y. Delaunay, A. Hood, B. M. Nguyen, D. Hoffman, Y. Wei, and M. Razeghi, "Passivation of type-II InAs/GaSb double heterostructure," *Applied Physics Letters,* vol. 91, p. 091112, 2007.

[101] B.-M. Nguyen, S. Bogdanov, S. A. Pour, and M. Razeghi, "Minority electron unipolar photodetectors based on type II InAs/GaSb/AlSb superlattices for very long wavelength infrared detection," *Applied Physics Letters,* vol. 95, p. 183502, 2009.

[102] C. L. Canedy, E. H. Aifer, J. H. Warner, I. Vurgaftman, E. M. Jackson, J. G. Tischler, S. P. Powell, K. Olver, J. R. Meyer, and W. E. Tennant, "Controlling

dark current in type-II superlattice photodiodes," *Infrared Physics & Technology,* vol. 52, pp. 326-334, 2009.

[103] A. Hood, A. Evans, A. Ikhlassi, D. Lee, and W. Tennant, "LWIR Strained-Layer Superlattice Materials and Devices at Teledyne Imaging Sensors," *Journal of Electronic Materials,* vol. 39, pp. 1001-1006, 2010.

[104] J. P. Prineas, M. Maiorov, C. Cao, J. T. Olesberg, M. E. Flatte, M. Reddy, C. Coretsopoulos, and M. Itzler, "Processes limiting the performance of InAs/GaSb superlattice mid-infrared PIN mesa photodiodes," 2006, p. 611904.

[105] V. Gopal, E. Plis, J.-B. Rodriguez, C. E. Jones, L. Faraone, and S. Krishna, "Modeling of electrical characteristics of midwave type II InAs/GaSb strain layer superlattice diodes," *Journal of Applied Physics,* vol. 104, p. 124506, 2008.

[106] J. Nguyen, D. Z. Ting, C. J. Hill, A. Soibel, S. A. Keo, and S. D. Gunapala, "Dark current analysis of InAs/GaSb superlattices at low temperatures," *Infrared Physics & Technology,* vol. 52, pp. 317-321, 2009.

[107] C. Cervera, K. Jaworowicz, H. Aït-Kaci, R. Chaghi, J. B. Rodriguez, I. Ribet-Mohamed, and P. Christol, "Temperature dependence performances of InAs/GaSb superlattice photodiode," *Infrared Physics & Technology,* vol. 54, pp. 258-262, 2011.

[108] D. R. Rhiger, R. E. Kvaas, S. F. Harris, and C. J. Hill, "Characterization of LWIR diodes on InAs/GaSb Type-II superlattice material," *Infrared Physics & Technology,* vol. 52, pp. 304-309, 2009.

[109] D. Z. Ting, C. J. Hill, A. Soibel, J. Nguyen, S. A. Keo, J. M. Mumolo, M. C. Lee, B. Yang, and S. D. Gunapala, "Antimonide superlattice barrier infrared detectors," 2009, p. 74190B.

[110] A. Soibel, J. Nguyen, S. B. Rafol, A. Liao, L. Hoeglund, A. Khoshakhlagh, S. A. Keo, J. M. Mumolo, J. Liu, D. Z. Ting, and S. D. Gunapala, "High-performance LWIR superlattice detectors and FPA based on CBIRD design," 2012, p. 82680Y.

[111] S. Krishna, "The infrared retina: Moving towards the fourth generation infrared detectors with quantum dots and superlattices," in *IEEE Photonics Society, 2010 23rd Annual Meeting of the*, 2010, pp. 527-527.

[112] R. Rehm, M. Walther, J. Fleissner, J. Schmitz, J. Ziegler, W. Cabanski, and R. Breiter, "Bispectral thermal imaging with quantum-well infrared photodetectors and InAs/GaSb type-II superlattices," 2006, p. 62060Y.

[113] S. Maimon and G. W. Wicks, "nBn detector, an infrared detector with reduced dark current and higher operating temperature," *Applied Physics Letters,* vol. 89, p. 151109, 2006.

[114] R. Q. Yang, Z. Tian, J. F. Klem, T. D. Mishima, M. B. Santos, and M. B. Johnson, "Interband cascade photovoltaic devices," *Applied Physics Letters,* vol. 96, p. 063504, 2010.

[115] R. Q. Yang, Z. Tian, Z. Cai, J. F. Klem, M. B. Johnson, and H. C. Liu, "Interband-cascade infrared photodetectors with superlattice absorbers," *Journal of Applied Physics,* vol. 107, pp. 054514-6, 2010.

[116] R. Q. Yang, Z. Tian, Z. Cai, J. F. Klem, M. B. Johnson, and H. C. Liu, "Interband-cascade infrared photodetectors with superlattice absorbers," *Journal of Applied Physics,* vol. 107, p. 054514, 2010.

[117] B. Klein, N. Gautam, S. Myers, and S. Krishna, "Temperature-dependent absorption derivative on InAs/GaSb Type II superlattices," 2012, p. 83530X.
[118] Q. Yang, C. Pfahler, J. Schmitz, W. Pletschen, and F. Fuchs, "Trap centers and minority carrier lifetimes in InAs/(GaIn)Sb superlattice long wavelength photodetectors," *Proc. of SPIE,* vol. 4999, pp. 448-456, 2003.
[119] S. D. Gunapala, S. V. Bandara, J. K. Liu, J. M. Mumolo, D. Z. Ting, C. J. Hill, and J. Nguyen, "First demonstration of megapixel dual-band QWIP focal plane array," in *Sensors, 2009 IEEE*, 2009, pp. 1609-1612.
[120] S. Bandara, P. Maloney, N. Baril, J. Pellegrino, and M. Tidrow, "Doping dependence of minority carrier lifetime in long-wave Sb-based type II superlattice infrared detector materials," *Optical Engineering,* vol. 50, p. 061015, 2011.
[121] M. Razeghi, S. A. Pour, E. Huang, G. Chen, A. Haddadi, and B.-M. Nguyen, "High-operating temperature MWIR photon detectors based on Type II InAs/GaSb superlattice," 2011, p. 80122Q.
[122] J. Pellegrino and R. DeWames, "Minority carrier lifetime characteristics in type II InAs/GaSb LWIR superlattice n[sup + ] pi p[sup + ] photodiodes," 2009, p. 72981U.
[123] C. H. Grein, K. A. El-Rub, and M. E. Flatté, "Enhancement of electron-initiated impact ionization in superlattice-based mid- and long-wavelength infrared avalanche photodiodes," in *State-of-the-Art Program on Compound Semiconductors XXXVII (SOTAPOCS XXXVII) / Narrow Bandgap Optoelectronic Materials and Devices*, 2002, pp. 80-87.
[124] K. A. El-Rub, C. H. Grein, M. E. Flatte, and H. Ehrenreich, "Band structure engineering of superlattice-based short-, mid-, and long-wavelength infrared avalanche photodiodes for improved impact ionization rates," *Journal of Applied Physics,* vol. 92, pp. 3771-3777, 2002.